Cell

Article

Human fetal brain self-organizes into long-term expanding organoids

Graphical abstract

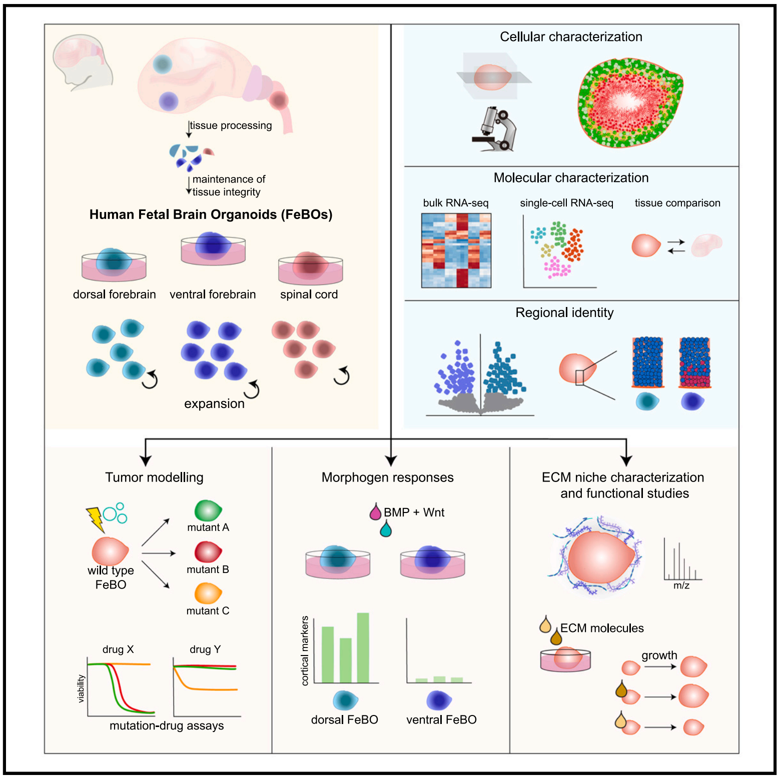

Highlights

- Human fetal brain organoids (FeBOs) display cellular heterogeneity and can be expanded
- FeBOs produce a tissue-like ECM niche and enable ECM perturbation studies
- Derivation of regional FeBOs allows the study of regional morphogen effects
- CRISPR-engineered FeBOs are a scalable bottom-up tumor modeling platform

Authors

Delilah Hendriks, Anna Pagliaro, Francesco Andreatta, ..., Wei Wu, Hans Clevers, Benedetta Artegiani

Correspondence

d.hendriks@hubrecht.eu (D.H.), h.clevers@hubrecht.eu (H.C.), b.a.artegiani@prinsesmaximacentrum.nl (B.A.)

In brief

Tissue-derived human fetal brain organoids (FeBOs) are established from different anatomical regions that can be expanded in culture. FeBOs may help understand developmental and disease-related biology.

Hendriks et al., 2024, Cell *187*, 712–732
February 1, 2024 © 2023 The Author(s). Published by Elsevier Inc.
https://doi.org/10.1016/j.cell.2023.12.012

CellPress

CellPress
OPEN ACCESS

Cell

Article

Human fetal brain self-organizes into long-term expanding organoids

Delilah Hendriks,[1,2,3,14,*] Anna Pagliaro,[1,12] Francesco Andreatta,[1,12] Ziliang Ma,[4,5,6] Joey van Giessen,[1] Simone Massalini,[1] Carmen López-Iglesias,[7] Gijs J.F. van Son,[1,3] Jeff DeMartino,[1] J. Mirjam A. Damen,[4] Iris Zoutendijk,[1] Nadzeya Staliarova,[4] Annelien L. Bredenoord,[8] Frank C.P. Holstege,[1,9] Peter J. Peters,[7] Thanasis Margaritis,[1] Susana Chuva de Sousa Lopes,[10] Wei Wu,[4,5,6] Hans Clevers,[1,2,3,11,13,14,*] and Benedetta Artegiani[1,13,14,15,*]

[1]Princess Máxima Center for Pediatric Oncology, Utrecht, the Netherlands
[2]Hubrecht Institute, Royal Netherlands Academy of Arts and Sciences (KNAW), Utrecht, the Netherlands
[3]Oncode Institute, Utrecht, the Netherlands
[4]Biomolecular Mass Spectrometry and Proteomics, Bijvoet Center for Biomolecular Research and Utrecht Institute of Pharmaceutical Sciences, Utrecht University, Utrecht, the Netherlands
[5]Singapore Immunology Network (SIgN), Agency for Science, Technology and Research (A*STAR), Immunos, Singapore 138648, Singapore
[6]Department of Pharmacy, National University of Singapore, Singapore 117543, Singapore
[7]The Maastricht Multimodal Molecular Imaging Institute, Maastricht University, Maastricht, the Netherlands
[8]Erasmus School of Philosophy, Erasmus University Rotterdam, Rotterdam, the Netherlands
[9]Center for Molecular Medicine, University Medical Center Utrecht and Utrecht University, Utrecht, the Netherlands
[10]Department of Anatomy and Embryology, Leiden University Medical Center, Leiden, the Netherlands
[11]Present address: Roche Pharmaceutical Research and Early Development, Basel, Switzerland
[12]These authors contributed equally
[13]These authors contributed equally
[14]Senior author
[15]Lead contact
*Correspondence: d.hendriks@hubrecht.eu (D.H.), h.clevers@hubrecht.eu (H.C.), b.a.artegiani@prinsesmaximacentrum.nl (B.A.)

https://doi.org/10.1016/j.cell.2023.12.012

SUMMARY

Human brain development involves an orchestrated, massive neural progenitor expansion while a multicellular tissue architecture is established. Continuously expanding organoids can be grown directly from multiple somatic tissues, yet to date, brain organoids can solely be established from pluripotent stem cells. Here, we show that healthy human fetal brain *in vitro* self-organizes into organoids (FeBOs), phenocopying aspects of *in vivo* cellular heterogeneity and complex organization. FeBOs can be expanded over long time periods. FeBO growth requires maintenance of tissue integrity, which ensures production of a tissue-like extracellular matrix (ECM) niche, ultimately endowing FeBO expansion. FeBO lines derived from different areas of the central nervous system (CNS), including dorsal and ventral forebrain, preserve their regional identity and allow to probe aspects of positional identity. Using CRISPR-Cas9, we showcase the generation of syngeneic mutant FeBO lines for the study of brain cancer. Taken together, FeBOs constitute a complementary CNS organoid platform.

INTRODUCTION

Human organoids are stem cell-derived three-dimensional (3D) structures that mimic features of the pertinent tissue, including molecular specification, cellular composition and architecture, and functionality.[1,2] As such, organoids allow *in vitro* study of physiological and pathological aspects of human tissue biology. Two sources of stem cells can be used to derive organoids: pluripotent stem cells (PSCs) and tissue stem cells (TSCs). The common approach to the derivation of any PSC-derived organoid model is the sequential exposure to a series of signaling cues. These are meant to direct developmental patterning and the differentiation trajectory, starting from early embryonic development, to germ layer specification, and ultimately to approximate organogenesis of the organ of interest.[3] Based on a different rationale, TSC-organoids can be derived from adult tissues by exploiting the capacity of most organs to expand or replace lost cells, either in homeostasis (e.g., the intestine[4]) or as repair mechanism (e.g., the liver[5,6]). Understanding the specific niche and tissue requirements is imperative to recreate an *in vitro* environment that allows continuous somatic (stem) cell expansion while retaining the capacity to generate differentiated progeny. TSC-organoids can also be derived from certain fetal tissues.[7–9] These expanding fetal tissue-derived organoid lines provide a fixed reflection of the developmental state of the tissue of origin and, unlike

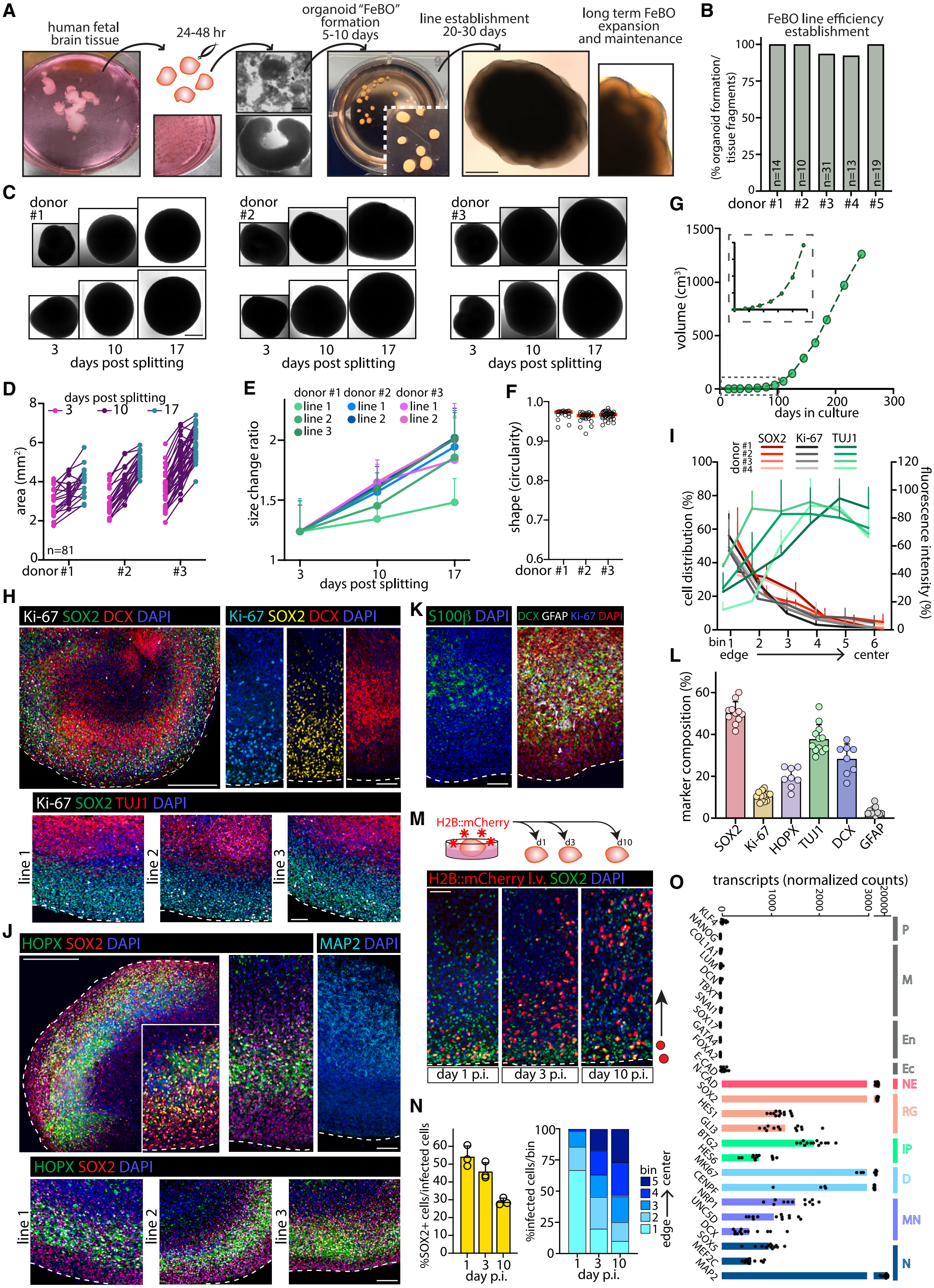

(legend on next page)

PSC-organoids, do not spontaneously progress until specifically switched to media promoting maturation.

PSC- and TSC-derived organoids represent complementary systems. Yet, establishment of both models has not been achieved for all organs. Organoids generated from PSCs can inform on developmental trajectories and associated disorders. TSC-organoids offer the possibility to study cell behavior and characteristics in health and disease directly in a native, specified human tissue and can as such inform on cell-intrinsic properties and physiology as well as on the external (niche) influences. TSC-organoids can be established as robust, long-term expanding lines, while PSC-organoids typically progress toward a certain endpoint of the developmental trajectory.[10]

The study of mammalian brain development and biology has greatly benefited from *in vivo* models, primarily rodents. Despite many principles of development being conserved, as compared with the rodent brain (e.g., mouse and rat), the human brain and its development present distinct characteristics.[11–14] These include surface folding, an enlarged forebrain, a more complex layered organization, temporally extended developmental processes (e.g., the progenitor expansion phase), and increased cellular diversity. This is highlighted for instance by the human-specific enrichment of a specific type of radial glia, the outer radial glia. Moreover, phylogenetic studies revealed human-specific gene regulatory mechanisms and pathways governing brain development.[11–14]

The advent of *in vitro* human cell-based brain models has facilitated studies on its development, evolution, and infective and neurodevelopmental diseases. Early pioneering studies led to cell cultures from rodent and human brain[15] and have since been further developed in the form of two-dimensional (2D) cultures,[16,17] 3D aggregates (neurospheres),[18] as well as short-lived organotypic slice cultures.[19] PSC-derived brain organoids/spheroids[20–22] present the advantage of a 3D architecture while being long-living, relatively scalable experimental models that enable to follow development in a dish and represent a growing field.

The human developing brain displays an evolutionarily unique expansion capacity[23] while simultaneously establishing cellular differentiation and diversity as well as a complex tissue architecture.[24] Yet, translation of these remarkable endogenous brain features into long-term expanding, 3D *in vitro* cultures has not been accomplished. Establishment of such models would allow the study of native tissue-intrinsic properties as well as of endogenous characteristics of cellular specification. Here, we attempt to generate long-term expanding CNS organoids from human fetal tissue.

RESULTS

Organoids derived from healthy human fetal brain tissue

We set out to determine whether the developing human brain can be captured into an expanding and self-organizing state *in vitro*. We focused on the early-mid neurogenesis period[25] and thus used healthy human fetal brain tissues from gestational week (GW) 12 to 15 (Figure S1A). Dissociated human neural stem cells (NSCs) can grow in culture as a monolayer[26] or as relatively small and unorganized 3D cell aggregates, neurospheres[18,27] (Figure S1B). We asked whether a different culture strategy could generate long-term expanding organoid cultures with tissue-like cellular and architectural complexity. To this end, we cut the tissue into small pieces (ca. 1–2-mm diameter) spanning the germinal and neuronal layers to preserve the original tissue architecture and cell-cell contacts (Figure 1A). These tissue fragments indeed contained various (proliferative) progenitors as well as neuronal cells (Figure S1C). We placed these pieces in

Figure 1. Generation of human fetal brain organoids through tissue self-organization

(A) Timeline and main steps for the establishment of tissue-derived human fetal brain organoid (FeBO) lines. Scale bars, 1 mm.

(B) Quantification of FeBO line establishment efficiency rates. The indicated n refers to the number of tissue fragments tested.

(C) Representative brightfield images showing single FeBOs growing after passaging. Scale bars, 1 mm.

(D) Organoid area expansion of FeBOs (dots) within a passage.

(E) Quantification of the FeBO size change ratio within a passage (mean ± SD).

(F) Quantification of the organoid shape (circularity) of FeBOs (dots).

(G) Estimated total biomass produced by the expansion of a FeBO line during 266 days.

(H) Representative immunofluorescence images for the indicated markers depicting cellular composition and organization in 3-month-expanded FeBOs (top) and reproducibility across different lines (bottom). Scale bars, 500 μm (left), 50 μm (right), and 100 μm (bottom).

(I) Quantification of the cell type distribution within FeBOs. The organoids were subdivided in multiple bins (from edge to center), and the number of cells ($SOX2^+$ and Ki-67^+) or fluorescence intensity (TUJ1) in each bin was quantified (mean ± SD of multiple FeBO lines per donor).

(J) Representative immunofluorescence images for the indicated markers depicting cellular composition and organization in 3-month-expanded FeBOs (top) and reproducibility across different lines (bottom). Scale bars, 500 μm (left), 100 μm (right), and 150 μm (bottom).

(K) Representative immunofluorescence images for the indicated markers depicting the presence of some astrocytes in expanding FeBOs. Scale bars, 100 μm.

(L) Quantification of the marker composition of expanding FeBO lines, highlighting neural stem cells (SOX2), outer radial glia (HOPX), proliferating cells (Ki-67), neuronal cells (DCX and TUJ1), and astrocytes (GFAP) across 3 different donors (mean ± SD, each dot represents a FeBO).

(M) Schematic of viral labeling experiment (top). Representative immunofluorescence images for SOX2 in H2B::mCherry lentivirus-infected FeBOs at different days post infection (p.i.) (bottom). Scale bars, 50 μm.

(N) Quantification of the percentage of $SOX2^+$/$mCherry^+$ (infected) cells across n = 3 FeBOs at different days p.i. (left) and the distribution of the percentage of infected cells in the organoid at different days p.i. (right). Organoids were subdivided in multiple bins (from edge to center), and $mCherry^+$ cells were counted in each bin.

(O) Mean expression of specific marker genes in FeBOs derived from bulk RNA sequencing. Pluripotency (P), mesenchyme (M), endoderm (En), ectoderm (Ec), neuroectoderm (NE), radial glia (RG), intermediate progenitors (IPs), dividing cells (D), migrating neurons (MNs), and neurons (N). Each dot represents a FeBO, n = 13 from different donors and varied culture ages.

See also Figures S1–S3.

a serum-free and extracellular matrix-free medium (including EGF, FGF-2, and FGF-10) and placed the cultures on an orbital shaker. Over the first 4 to 8 days, we noticed the formation of multiple 3D structures, which developed defined borders (Figure 1A). These sometimes exhibited some surface folding, presumably due to the stem cell expansion and space constraints. These structures grew over time while maintaining a tissue-like appearance (Figure 1A). We termed these fetal brain organoids (FeBOs). Individual fetal brain tissue fragments were cultured separately, each generating an individual FeBO line. Take rates of individual fragments were high (>95% success rate) (Figures 1B and S1D).

FeBOs could be reliably passaged by cutting of a whole organoid, and each of these single FeBO pieces consistently reformed entire organoids, yielding stably expanding FeBO lines within 20–30 days of culture (Figures 1C and S1E). We next assessed their expansion kinetics. On average, organoids doubled their size after each split (every 2 weeks) (Figures 1C–1E). The optimal size to passage FeBOs was empirically determined (~2.5–3.0 mm in diameter). Across multiple organoids (n > 80) derived from different lines and different donors, the growth kinetics were reproducible, as were FeBO morphology and their size, which depended on the initial piece size (Figures 1C–1F, S1E, and S1F). From all 7 donors, FeBOs could be expanded long-term (Figures 1G, S1G, and S1H). The estimated biomass that could be produced after 8 months from only ~0.1 cm^3 of initially established organoids was ~1,500 cm^3, representing an increase in tissue volume of 15,000-fold (Figure 1G). After this long culture period, FeBOs typically slow down their growth but can be viably maintained (Figure S1G).

We assessed the cellular composition of FeBOs using a panel of common neurodevelopmental markers[25] (Figures 1H–1L, S2, S3A, and S3B). Abundant neural stem/progenitor cells ($SOX2^+$), often Ki-67^+, were located at the periphery of the FeBOs, delimited by intact adherent junctions (ZO-1^+) (Figures 1H–1J, S2, and S3B). Neuronal cells ($TUJ1^+$, DCX^+, and $NeuN^+$ cells) were located toward the FeBO center (Figures 1H–1J and S2). This organization was consistent across FeBO lines from different donors (Figures 1I and S2) and over time before-after splitting (Figure S3A). Some $GFAP^+$ and $S100\beta^+$ astrocytes were observed, interspersed between DCX^+ cells (Figure 1K). Importantly, we noted a thick layer of $HOPX^+$ cells. Those cells were positive for SOX2, PAX6, and often also for Ki-67, and were located above the positive $SOX2^+/PAX6^+$ ($HOPX^-$) dense layer (Figures 1H, 1J, S2A, and S3B), all hallmarks of the outer radial glial cells (oRGs),[28–30] a cell type enriched in primates. Quantification of cellular composition revealed reproducible abundance of the different cell populations (Figure 1L), highlighting robust cellular heterogeneity within FeBOs. Intriguingly, preserving tissue integrity was previously linked to maintenance of cellular heterogeneity in tumor-derived brain organoids.[31] Typical cell biological and morphological features of neural tissue within FeBOs were also detected by transmission electron microscopy, including neurites and axons with microtubules (Figure S3C). We then used lentiviral infection of intact FeBOs to assess cell lineage dynamics. Over half of the infected cells were $SOX2^+$ and mostly located near the surface of the organoid 1 day post infection. Over time, labeled cells increased in abundance and were located also in the inner neuron-rich ($SOX2^-$) part of the organoid and colocalized with TUJ1 (Figures 1M, 1N, and S3D), supporting ongoing neurogenesis.

Finally, transcriptomic characterization of whole FeBOs revealed the absence of marker expression for pluripotency (*KLF4* and *NANOG*), mesoderm (*LUM* and *Brachyury*), endoderm (*GATA4* and *SOX17*), and ectoderm (*E-CAD*) (Figure 1O). Instead, markers for developing brain cell populations were robustly expressed. These included markers for RG cells (*SOX2*, *HES1*, and *GLI3*), intermediate neurogenic progenitors (*BTG2* and *HES6*), newborn migrating neurons (*NRP1*, *UNC5D*, and *DCX*), and neurons (*SOX5*, *MEF2C*, and *MAP2*). Proliferation markers (*MKI67* and *CENPF*) were also highly expressed. Together, this highlighted their exclusive neuroectodermal identity (N-CAD^+) (Figure 1O). The transcriptomic analyses furthermore underscored organoid-to-organoid similarity (Figure S3E). Altogether, FeBO lines possess an active stem/progenitor cell pool, accounting for their long-term expansion upon repeated splitting while at the same time capturing broad cellular heterogeneity and organization by the generation of neuronal cells, providing a "snapshot" of the tissue of origin.

FeBOs capture regional brain identities of the tissue of origin

We questioned whether we could culture region-specific FeBOs and whether regional identity is an intrinsic tissue property that can be captured *in vitro*. We separately processed individual fragments derived from anatomically different human brain regions (Figure 2A) and used a qPCR marker panel on the original tissue fragments to assign identities (Figure S4A). Most fragments were of telencephalic origin (*FOXG1*$^+$), in concordance with the abundance of this region at the gestational ages of the donor tissues. These fragments enriched for either dorsal (*EMX1*$^+$ and *PAX6*$^+$)[32] or ventral (*DLX2*$^+$, *GSX2*$^+$, and *NKX2-1*$^+$)[33] forebrain markers (Figure S4B). The assigned identity was further confirmed on whole transcriptome level, followed by VoxHunt analysis (Figures S4C and S4D). From these fragments, we could establish separate FeBO lines, termed dorsal and ventral FeBOs, with comparable efficiency, and presenting expression of dorsal and ventral forebrain markers, respectively (Figures 2B–2E).

We characterized the region-specific identities of these regional FeBOs by immunofluorescence (Figures 2E–2G and S2B). Dorsal-specific $PAX6^+/SOX2^+$ stem cells were located in the Ki-67-rich outer layer, while $MAP2^+$ neurons were located mostly in the inner part of dorsal FeBOs (Figures 2E, 2F, S2B, and S5A). $EMX2^+$ dorsal progenitors were likewise located on the periphery, forming a distinct layer below the DCX^+ neurons (Figures 2F and S2B). Some $TBR2^+$ intermediate progenitors were also identified in younger cultures (Figures 2F and S2B). Similar distribution and abundance of the different classes of cell types was observed across dorsal FeBOs from multiple donors (Figures 2F, 2H, and S2B). Ventral FeBOs were characterized by a $PAX6^-$ outer layer of $SOX2^+$ and NKX2-1^+ ventral forebrain progenitor cells (Figures 2E, 2G, and S2B). In addition, $OLIG2^+$ progenitor cells[34] were intermingled with $DLX2^+$ cells (representing early interneurons[35,36]) (Figures 2G, S2B, and S5A). GABAergic interneuron markers GAD65 and GAD67[36]

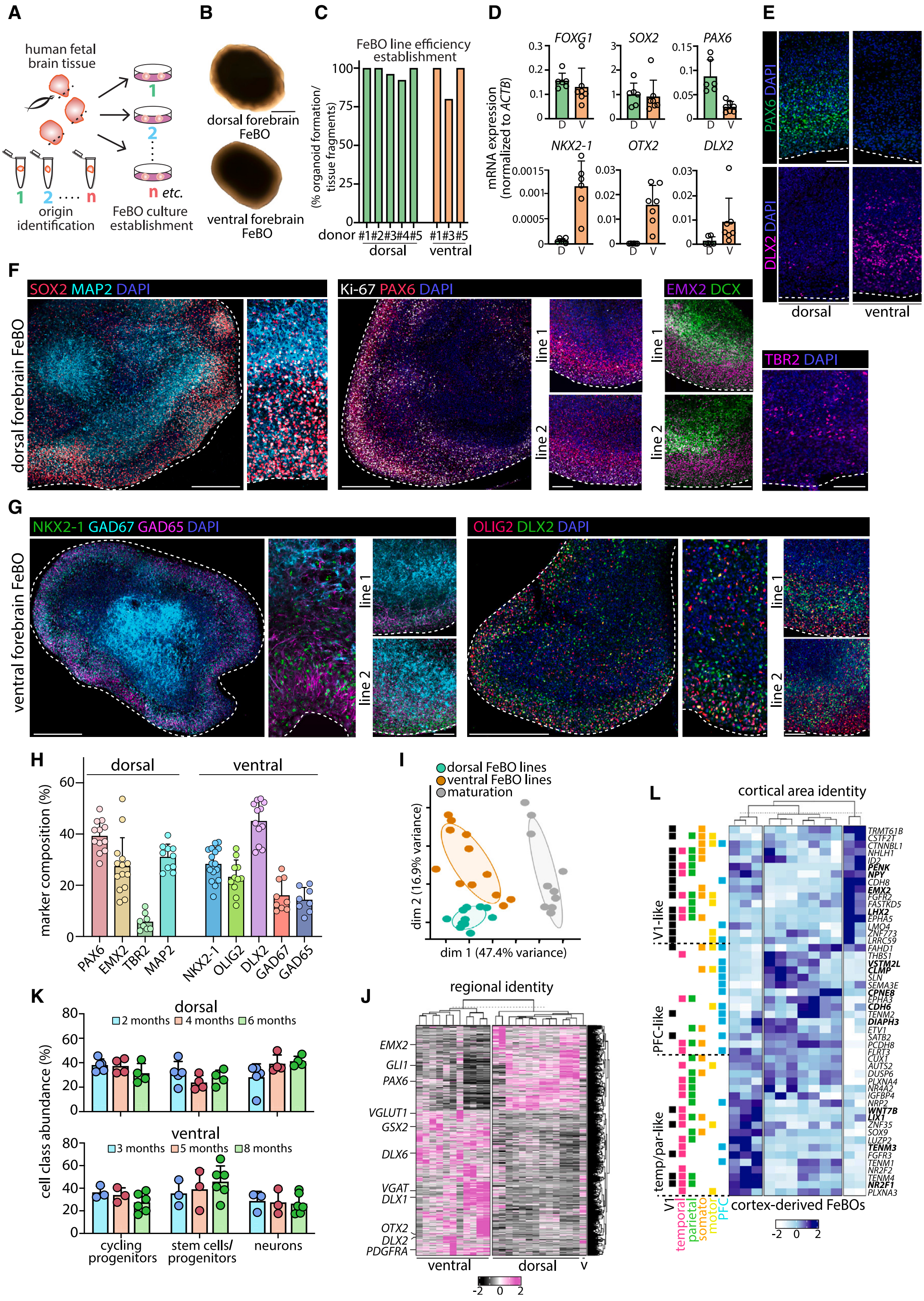

(legend on next page)

were also present (Figures 2G, S2B, and S5B). Quantifications of cell type percentages showed reproducible cellular composition across multiple ventral FeBO lines (Figures 2H and S5A–S5C). We next performed bulk RNA sequencing analysis of regional forebrain FeBOs (Figures 2I and 2J). The expression profiles of both FeBO types indicated a clear developing brain profile (Figure S4E). Dorsal vs. ventral forebrain FeBOs clustered separately based on their regional origin (Figures 2I and 2J; Table S1). We noted enrichment of well-known markers and patterning genes such as *PAX6*, *EMX2*, *EMX1*, and *VGLUT1* in dorsal FeBOs, and vice versa *GSX2*, *CALB1*, *VGAT*, *SCGN*, and *DLX* genes in ventral FeBOs (Figures 2J and S4F).

We next probed the stability of expanding FeBOs during long-term culture. Different cell populations (SOX2$^+$, PAX6$^+$, TUJ1$^+$, Ki-67$^+$, DLX2$^+$, NKX2-1$^+$, and GAD67$^+$) remained largely stable over time over repeated splitting events (>6 months expansion) in regional FeBO lines (Figures S5A–S5C). This was further corroborated by inferring the relative proportion of the main cell classes within multiple FeBOs by whole transcriptome deconvolution (Figure 2K) and by correlation of whole transcriptomes across "early-mid-late passage" FeBOs (Figure S5D). RNA expression of some neuronal markers increased in long-term expanding FeBOs (Figures S4G–S4J). These included genes connected with neuronal functions and brain development, e.g., the presynaptic and postsynaptic proteins (*SYN1*, *PSD-93*, and *PSD-95*), neurexins and neuroligins, the NMDA receptors (*GRIN2A* and *GRIA1*), as well as astrocytic (*S100β*) and oligodendrocytic (*PDGFRA*) genes, suggesting that some degree of gradual maturation spontaneously occurred. GFAP$^+$ astrocytes, intermingled with neurons, also appeared morphologically more complex in 8-month-expanded dorsal FeBOs (Figure S5E).

To further probe the derivation of FeBOs from an anatomically distant brain region, we generated organoids from human fetal spinal cord tissue (GW8), which displayed regionalized expression of specific progenitor and motor neuron markers (Figures S6A–S6D).

Along the rostro-caudal axis, the human cortex is subdivided into distinct specialized areas, with the prefrontal cortex (PFC) and primary visual (V1) cortex spanning the two poles. We retrospectively evaluated the expression signatures of markers associated with cortical area patterning[37,38] in different cortex-derived FeBO lines (each derived from a unique cortex fragment). Certain lines showed enrichment of V1 markers (*PENK*, *NPY*, and *LHX2*), while other lines enriched for either PFC (*CLMP*, *VSTM2L*, and *CPNE8*), or temporal/parietal markers (*WNT7B*, *LIX1*, and *NR2F1*) (Figure 2L; Table S2). Altogether, aspects of endogenous *in vivo* tissue "imprinting" are reflected *in vitro* in regional FeBO cultures.

Modulation of expansion vs. maturation by culture conditions

We wondered whether we could further enhance maturation of the FeBOs, inspired by other TSC-derived organoid models.[39] We thus altered the FeBO environment, mainly by withdrawal of growth factors and addition of 0.5% basement membrane extract (Figure 3A). In this maturation medium, FeBOs slowed down their expansion. Transcriptomic comparison of FeBOs maintained for 10 days in maturation medium revealed broad changes in gene expression (Figures 2I and 3B), likely also reflecting changes in cell class ratios (Figure 3C). Various progenitor and proliferation markers were reduced, while most markers for early and late neuronal specification were generally upregulated across both FeBO types (Figure 3B; Table S1). Notably, multiple genes associated with mature neuronal functions, e.g., synaptic components and neurotransmitter receptors and secretion, increased during maturation (Figure S7A). Characterization by immunofluorescence confirmed a decrease in the number of SOX2$^+$ stem cells (Figures 3D and S7B). Matured dorsal FeBOs displayed increased expression of the pan-neuronal marker TUJ1 as well as DCX (Figures 3D and S7B). The layer-specific markers CTIP2, SATB2, BRN2, TBR1, CUX1, RORβ, and SOX5 were detected and appeared organized (Figures 3D, 3E, and S7C). Matured dorsal FeBOs further displayed abundant MAP2$^+$ neuronal processes (Figure 3F). We observed increased numbers of DLX2$^+$ and GAD65$^+$ interneurons in matured ventral FeBOs, while expression of NKX2-1 and OLIG2 was reduced (Figures 3G, S7B, and S7D). In some organoids, the interneurons

Figure 2. Derivation of regional FeBOs from different brain regions
(A) Strategy to derive regional FeBOs.
(B) Representative brightfield images of regional forebrain FeBOs. Scale bars, 1 mm.
(C) Quantification of FeBO line establishment efficiency rates from dorsal and ventral forebrain.
(D) Differences in mRNA expression of specific regional markers across dorsal (D) and ventral (V) forebrain-derived FeBOs (dots) from varied culture ages.
(E) Representative immunofluorescence images for PAX6 (dorsal forebrain marker) and DLX2 (ventral forebrain marker) in regional FeBOs. Scale bars, 100 μm.
(F) Representative immunofluorescence images of dorsal forebrain FeBOs for the indicated markers and reproducibility across different lines (2–3 months expanded). Scale bars, 500 μm (whole organoids), 200 μm (lines), and 100 μm (TBR2).
(G) Representative immunofluorescence images of ventral forebrain FeBOs for the indicated markers and reproducibility across different lines (2–3 months expanded). Scale bars, 500 μm (whole organoids) and 200 μm (lines).
(H) Quantification of the marker composition of expanding dorsal and ventral forebrain FeBO lines across 3 different donors (mean ± SD, each dot represents a FeBO).
(I) PCA on whole transcriptomes of expanding FeBOs derived from dorsal (green) or ventral (orange) forebrain as well as matured FeBOs (gray).
(J) Heatmap showing the expression of differentially expressed genes ($|\log_2 FC| > 0.5$, $p < 0.05$) between dorsal and ventral forebrain FeBOs. Columns represent FeBO lines from different donors and varied culture ages (2–8 months).
(K) Estimated cell class abundance in regional FeBOs of varied culture ages through deconvolution of bulk RNA sequencing transcriptomes. Each dot represents a FeBO.
(L) Heatmap showing the expression of gene markers of the different subareas of the human cortex in different cortex-derived FeBOs (columns). Boxes indicate enriched expression of each marker across the different cortical areas as reported in human fetal brain tissue.
See also Figures S2 and S4–S6.

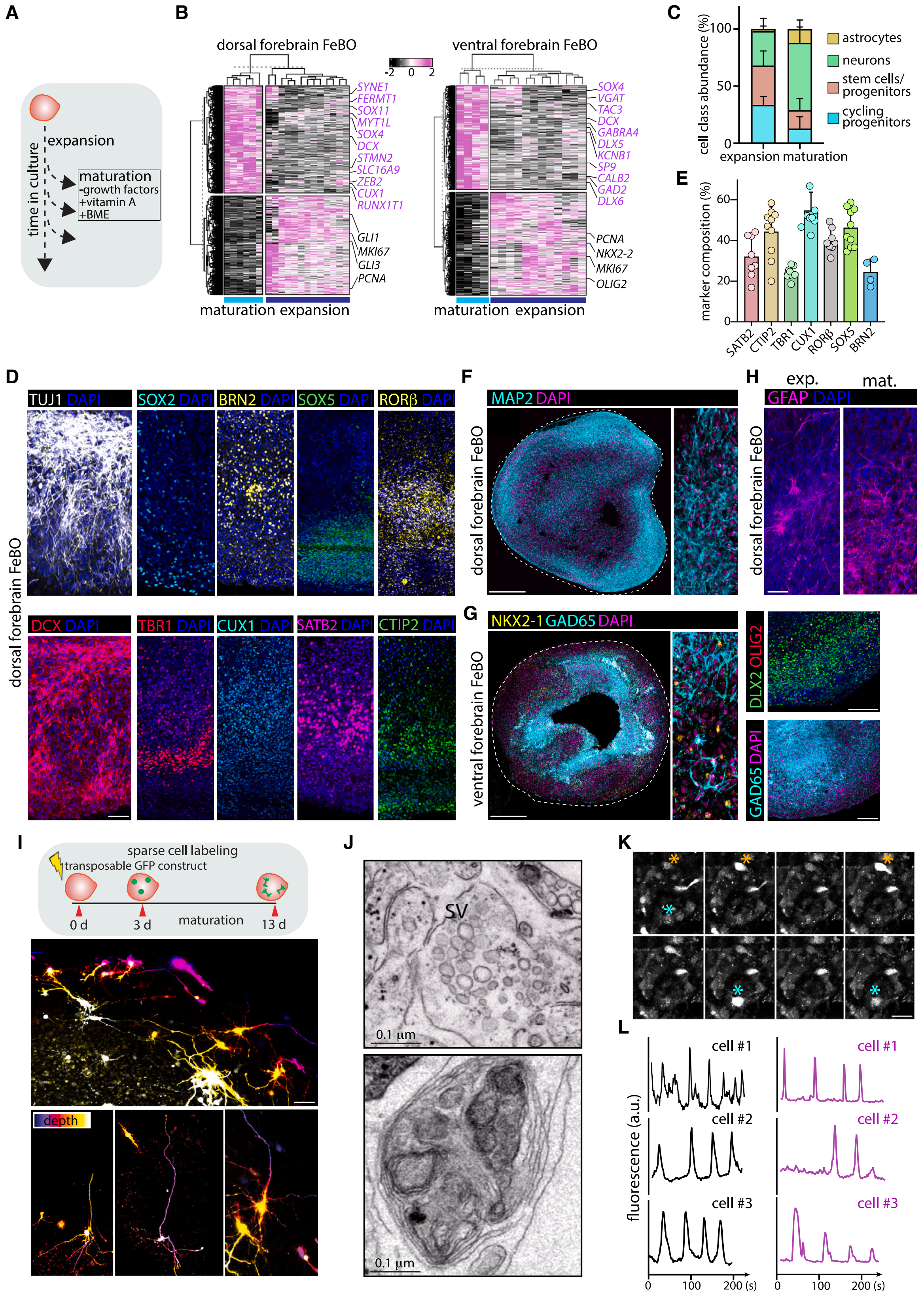

(legend on next page)

had more variable locations and were organized in bundles, reminiscent of the migratory interneuron streams observed *in vivo*[40] (Figures S7D and S7E). GFAP$^+$ astrocytes also increased upon maturation (Figures 3C and 3H).

We investigated whether acquisition of mature traits was also apparent regarding morphological and cell structural features. We established conditions to sparsely label individual cells by whole-organoid electroporation of a transposable GFP construct. This revealed many cells with typical neuronal morphology, displaying arborization (Figure 3I). Transmission electron microscopy analysis confirmed the presence of multiple neuronal processes with aligned neurotubules, neurofilaments, and interspersed elongated mitochondria (Figures S8A and S8B). We observed neuronal terminals containing neurotransmitter synaptic vesicles, suggestive of synapse formation (Figures 3J and S8C). We also detected structures that could possibly be interpreted as initial stages of myelination around axons (Figures 3J, S8D, and S8E). Of note, we also observed increased mRNA expression of mature oligodendrocyte markers (*MBP*, *PLP1*, *SOX10*, and *PCDH15*). Lastly, we live-imaged FeBOs matured for 7 days in the presence of a fluorescent calcium probe. Many cells exhibited spontaneous and regular calcium spikes, both in matured FeBOs derived from early and late passage lines (Figures 3K, 3L, and S7F; Video S1).

FeBO profiles resemble human fetal brain tissue at single-cell level

To address the cellular heterogeneity of the FeBOs in more detail, we performed single-cell sequencing of cells derived from FeBOs in expansion medium and after a short pulse of maturation from both dorsal and ventral forebrain origin (6 months in culture). Clustering analysis of ventral FeBOs identified 13 clusters, all of neural identity (V0–V12), corresponding to 8 main populations (Figures 4A, 4B, and S9A–S9D). Cell type assignment was based on previously reported markers and signatures for developing human forebrain subpopulations (Table S2; Figure S9E). We noticed substantial radial glia diversity. Subpallial RG cells expressed typical NSC markers (*SOX2*, *ID4*, *HES1*, and *VIM*) and specific markers of ganglionic eminence (GE) precursors (*NTRK2*, *TTYH1*, and *SOX6*).[41,42] Some expressed higher levels of RG/astrocytic genes (*AQP4*, *AGT*, and *GFAP*), likely representing states of radial glia primed for (V6) or transitioning to (V2) astrocyte differentiation. V10 cells expressed *NR2F1* and *NR2F2*, important for radial glia to acquire gliogenic competence.[43] We also detected glycolytic radial glia (*BNIP3* and *PGK1*), also observed in PSC-brain organoid models[44,45] and linked to signatures found in fetal tissue,[45,46] as well as cells expressing truncated RG (tRG) markers (*CRYAB*) (V1 and V5). Higher expression of neurogenic ventricular RG markers (*NESTIN*, *HES5*, and *FABP7*) and oRG markers (*HOPX*, *PTPRZ1*, and *TNC*) were detected in V0 and V3. Accordingly, some neuronal markers (*GAP43*) were expressed. Markers of ventral neuronal precursors/intermediate progenitors (*PTTG1*, *ASCL1*, and *KPNA2*) and proliferation (*MKI67*, *PCNA*, and *TOP2A*) were expressed in V4 and V9. V7 contained newborn neurons, characterized by ventral forebrain-restricted progenitor markers (*GSX2*), markers of neuronal commitment (*SOX4*, *SOX11*, and *PROX1*), and specification of interneurons (*DLX5* and *ASCL1*).[42] GABAergic interneuron markers (*VGAT*, *DLX6*, *CALB2*, and *GAD2*) were expressed in mature neuronal clusters V8 and V12. In general, we noted for both FeBO types that cells retrieved from single-cell sequencing underestimated neuronal cell population proportions as compared with immunofluorescence observations, presumably owing to the difficulty in viably retrieving single neurons as well as their inside localization within FeBOs. Oligodendrocyte precursors (OPC) markers (*OLIG1* and *OLIG2*) and the more mature marker *SOX10* were expressed in V11 (Figures 4A, 4B, and S9A–S9D). Endothelial cells, microglia, or other immune cells were not detected.

We defined at higher resolution the heterogeneity of the neurogenic and neuronal populations by subclustering analysis (Figures 4C, S10A, and S10B). We identified different classes of *ASCL1*$^+$ interneuron precursors that were *POU3F2*^{high}, *MEIS2*^{high}, or *ZEB2*^{high} (Figures 4C, S10A, and S10B), reflecting the precursor cellular diversity of human fetal GE tissue.[42] These cells also enriched for *NRP1* and *CXCR4*, expressed in migratory streaks of progenitor cells.[47] We noted a transition in expression of *SLC12A2* (NKCC1) and *SLC12A5/6* (KCC2/3) from the

Figure 3. Cellular and molecular maturation of FeBOs

(A) Strategy to further mature FeBOs at any given time in culture, with the main changes indicated.

(B) Heatmaps showing the differentially expressed genes between FeBOs in maturation and expansion medium ($p < 0.05$). Columns represent FeBO lines from varied culture ages.

(C) Estimated cell class abundance in expanding and matured FeBOs through deconvolution of bulk RNA sequencing transcriptomes (mean ± SD).

(D) Representative immunofluorescence images for the indicated markers in 10-day-matured dorsal forebrain FeBOs (matured after 2–3 months expansion). Scale bars, 100 μm.

(E) Quantification of the neuronal marker composition in matured dorsal forebrain FeBOs (mean ± SD, each dot represents a FeBO).

(F) Representative immunofluorescence images for MAP2 in 10-day-matured dorsal forebrain FeBOs. Scale bars, 500 μm.

(G) Representative immunofluorescence images for the indicated markers in 10-day-matured ventral forebrain FeBOs (matured after 2–3 months expansion). Scale bars: 500 μm (left) and 200 μm (right).

(H) Representative immunofluorescence images for GFAP in expanding and matured dorsal forebrain FeBOs. Scale bars, 50 μm.

(I) Schematic of sparse single-cell labeling in FeBOs (top). Representative images of GFP$^+$ labeled neuronal cells color-coded by depth (bottom). Scale bars, 20 μm.

(J) TEM images showing matured features in FeBOs including synaptic vesicles (SVs) (top) and putative indications of early stages of myelination (bottom).

(K) Live imaging of spontaneous electric activity in matured FeBO slices. Asterisks point at cells displaying spontaneous calcium spikes. Scale bars, 20 μm.

(L) Examples of calcium recording in different cells visualized as changes in fluorescence intensity over time in matured FeBO slices of early (2 months) passage (black) and late (6 months) passage (purple).

See also Figures S7 and S8.

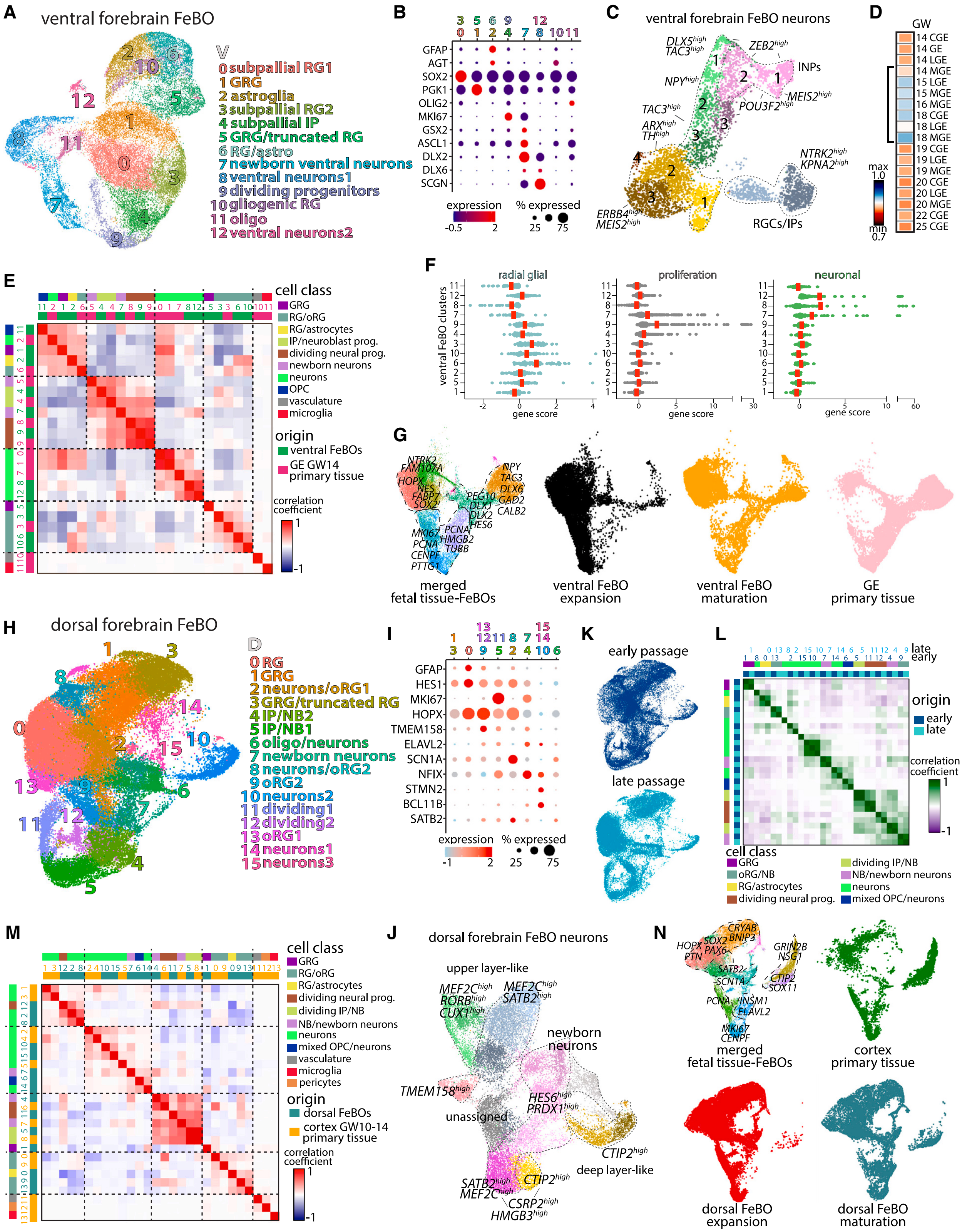

(legend on next page)

neurogenic precursors to the more mature neurons.[48] The *CALB2*$^{+}$ neurons showed a degree of diversity, with some enriched for *MEIS2* and *ERBB4*, and others *TAC3*$^{+}$, *NPY*$^{+}$, *ST18*$^{+}$, or *TH*$^{+}$ (Figures 4C and S10B).

We next assessed FeBO-to-tissue similarity. Tissue age resemblance of ventral forebrain FeBOs using pseudobulk comparisons to GW14-25 fetal GE tissues[37] revealed good correlation with GW14-18 tissues (Figure 4D). We then performed organoid-tissue cluster correlation comparisons with the GW14 tissue dataset. We noted distinct groups of specific cell classes, composed of intermingled organoid and tissue clusters, correlating with each other (Figures 4E, S9F, and S9G). Specific FeBO clusters were enriched for corresponding cell type gene signatures found in tissue[37] (Figure 4F). Finally, integration and UMAP visualization of the tissue and the expanding and matured FeBO datasets showed that similar cell types were present in the different datasets (Figure 4G). This was further confirmed by comparisons to an additional human fetal GE tissue dataset[42] (Figure S9H).

We next evaluated the single-cell sequencing profiles of the dorsal FeBOs (Figures 4H, 4I, and S11A–S11E). Also in these organoids, we captured radial glia diversity, as described in tissue.[49] D0 cells expressed typical RG markers (*SOX2*, *HES1*, and *SOX9*), including ventricular RG (*FBXO32*) and dorsal telencephalic neurogenic progenitor markers (*PAX6* and *HES5*). RGs enriched for markers of tRG (e.g., *CRYAB*) were detected in D3. D1 represented glycolytic radial glia (*BNIP3* and *PGK1*). D13 and D9 encompassed the oRG population (*HOPX*, *PTPRZ1*, *FAM107A*, and *PTN*). Neurogenic intermediate progenitors were identified (*INSM1*, *TMEM158*, and *HES5/6*). Some of these (D11 and D12) expressed cycling genes (*MKI67* and *PCNA*), while D4 and D5 started expressing markers of differentiation/commitment and migration of cortical neurons (*RND2*, *POU3F2*, *NFIA*, and *SOX4*). The remaining clusters expressed newborn and mature neuron markers (*CTIP2*, *NFIX*, *STMN2*, *SOX11*, and *BACH2*), which we further subclustered (Figures 4J, S10C, and S10D). Most cells expressed some newborn cortical excitatory neuron markers (*PRDX1*, *ENC1*, and *CSRP2*) but lacked expression of *NEUROD* genes. Deep-layer neuron-like subclusters expressed layers 5–6 markers, including *CTIP2*, *SOX5*, *NFIA*, *NFIB*, and *CELF1*. Upper-layer neuron-like cells displayed higher expression among others of *SATB2*, *RORB*, *MEF2C*, *POU3F2*, *CUX1*, *CUX2*, and *RAC3*, markers of cells isolated mostly from layers 2–4[45,49–51] (Figures 4J, S10C, and S10D; Table S2).

To assess cellular diversity over time in culture, we compared early passage FeBOs (2 months) to 6-month-old (late passage) FeBOs. Cells integrated well in the same UMAP space, and correlation analysis showed good correlation of most corresponding cell clusters (Figures 4K and 4L). We then assessed tissue similarity of the dorsal FeBO datasets. Cortical tissue (GW10–14)[37] clusters and dorsal FeBO clusters with the same assigned cell identity were intermingled in correlation analysis (Figures 4M, S11F, and S11G). UMAP integration of the FeBO datasets with two independent tissue datasets[37,52] revealed representation of cells coming from both tissue and organoid origins across clusters, corroborating cellular diversity in both expanding and matured dorsal FeBOs (Figures 4N and S11H). Altogether, these characterizations highlighted that FeBO cells present cellular heterogeneity and compare well with primary cell types.

A tissue-like ECM niche in expanding FeBOs

Growing evidence suggests a crucial role of extracellular matrix (ECM) and ECM-cell interactions in regulating the human-specific expansion of the developing brain.[53–55] Supplying exogenous decellularized human brain ECM instead of non-neural matrices (Matrigel) enhanced cell expansion in PSC-brain organoids.[56] Furthermore, mutations in ECM genes have been linked to developmental defects.[57] We hypothesized that FeBOs constitute a self-sustained expanding structure through maintenance of a favorable ECM tissue-like microenvironment.

Comparative whole transcriptome analysis of classes of ECM genes and cell-to-ECM-interaction genes revealed a high resemblance between the profiles of expanding FeBOs and developing human brain tissue (Figures 5A and S12A). ECM components were expressed by different FeBO cell types, with a predominance of RG and oRG, similar to fetal brain tissue (Figures S12B and S12C). Further comparison with published

Figure 4. Cellular similarity between FeBOs and human fetal brain tissue

(A) Single-cell profiling of cells derived from expanding and 5-day-matured ventral forebrain FeBOs (6 months expanded).

(B) Dot plot showing the expression of selected cell type markers in the different clusters in ventral forebrain FeBOs.

(C) Subclustering analysis on neurogenic and neuronal populations identified in ventral forebrain FeBOs.

(D) Primary tissue age resemblance of ventral forebrain FeBOs based on pseudobulk comparisons with primary GE tissues from different gestational ages (Bhaduri et al.[37]). Medial ganglionic eminence (MGE), lateral ganglionic eminence (LGE), and caudal ganglionic eminence (CGE).

(E) Correlation plot comparing organoid-tissue clusters with assigned cell classes between ventral forebrain FeBOs and primary GE tissue (Bhaduri et al.[37]).

(F) Gene score analysis in ventral forebrain FeBO clusters of primary GE tissue signatures of radial glial cells, cycling cells, and neuronal cells. Each dot represents a gene score for a specific marker.

(G) UMAP plots depicting the integration of the expanding and matured ventral forebrain FeBO datasets with primary GE tissue.

(H) Single-cell profiling of cells derived from expanding and 5-day-matured dorsal forebrain FeBOs (early and late passage integrated).

(I) Dot plot showing the expression of selected cell type marker genes in the different clusters in dorsal forebrain FeBOs.

(J) Subclustering analysis on neurogenic and neuronal populations identified in dorsal forebrain FeBOs.

(K) UMAP plots depicting the similarity of expanding and matured dorsal forebrain FeBOs at early passage (2 months) and late passage (6 months).

(L) Correlation plot comparing early passage-late passage clusters (as per H) with assigned cell identities of dorsal forebrain FeBOs.

(M) Correlation plot comparing organoid-tissue clusters with assigned cell identities between dorsal forebrain FeBOs and primary cortex tissue (Bhaduri et al.[37]).

(N) UMAP plots depicting the integration of the expanding and matured dorsal forebrain FeBO datasets with primary cortex tissue.

See also Figures S9–S11.

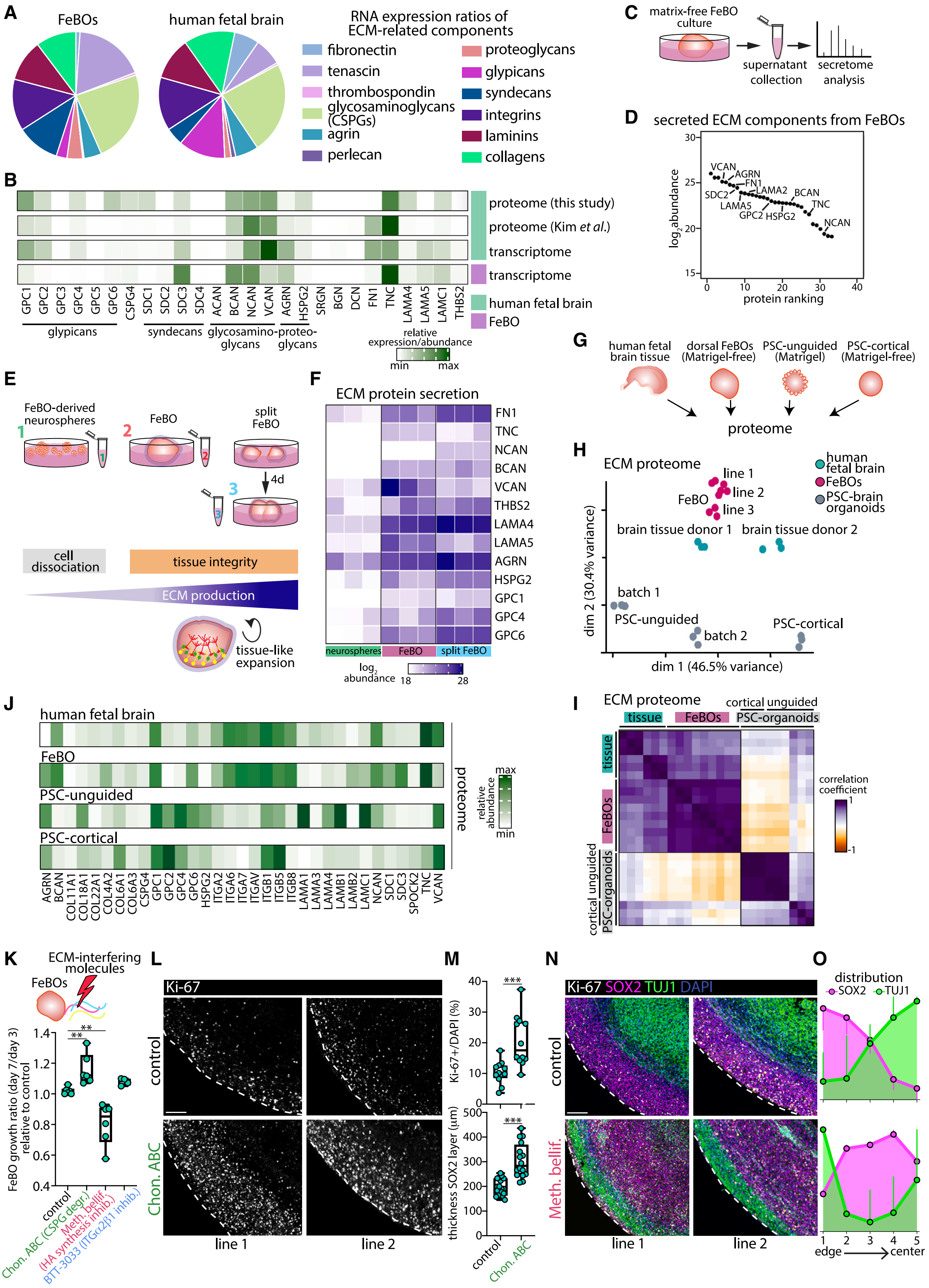

(legend on next page)

proteomic data[58] as well as our proteomic data of human fetal brain, revealed good transcriptomic-proteomic expression similarity of key ECM brain components (e.g., proteoglycans, glypicans, and syndecans) (Figure 5B). We addressed functional ECM secretion through secretome mass spectrometry analysis of FeBO supernatants (Figures 5C and S12D). Various secreted ECM components were detected (Figures 5D and S12E), including components specifically enriched in human fetal brain[58] (Figure S12F).

To understand whether the intrinsic capacity of the FeBOs to secrete a tissue-like "matrisome" is linked to the maintenance of cell-to-cell organization and integrity, we compared the secretome of intact FeBOs (established organoids as well as those reforming shortly after splitting) with the secretome of neurospheres, derived from FeBOs after a single-cell dissociation step (Figure 5E). FeBOs and FeBO-derived neurospheres displayed distinct ECM secretomes as assessed by principal-component analysis (PCA) clustering (Figure S12G), and brain-relevant ECM components were more abundant in FeBO secretomes (Figures 5F and S12H; Table S3). These observations suggested that the continued maintenance of tissue integrity promotes generation of an ECM niche, which in turn may promote sustained expansion of FeBOs in a tissue-like structure (Figure 5E). Of note, matrisome secretion increased in FeBOs shortly after splitting, suggesting the importance of ECM during FeBO regrowth/formation (Figures 5F and S12H).

To further investigate if the FeBOs resembled a proper tissue-like ECM niche, we performed side-by-side comparative proteomic analyses with human fetal brain tissue. Moreover, to understand how the developing human brain tissue ECM niche compared not only with FeBOs but also with PSC-derived 3D brain models, we also included proteomic analysis of unguided PSC-cerebral organoids (supplemented with Matrigel)[59] and PSC-cortical spheroids (generated without the addition of exogenous matrices)[60] (Figures 5G, S13A, and S13B).

PCA and correlation analyses showed that the ECM-related proteome of different FeBO lines and human fetal brain tissues displayed similarity and clustered together. PSC-cortical spheroids and particularly unguided PSC-cerebral organoids were more distinct from the FeBO-tissue cluster (Figures 5H and 5I). Also at whole proteome level, FeBOs clustered closely together with fetal brain tissue (Figure S12I). Finally, we inspected the proteomic expression of relevant matrisome components. Expression patterns were similar across FeBOs and tissue, whereas the PSC-brain models considered here demonstrated a more diverse ECM composition (Figure 5J; Table S3). These differences may find their origin in the observation that the ECM niche of the developing brain is tightly linked to human progenitor expansion.[55]

We probed whether FeBOs could be used to study the effect of experimental ECM perturbations. We performed a proof-of-concept screen using small molecules or enzymes interfering at various levels with ECM-related signaling (Figure 5K). We noted rapid growth effects upon ECM perturbations. FeBOs exposed to chondroitinase ABC (degrading CSPGs) displayed increased growth (Figure 5K). Histological analysis confirmed an increase in Ki-67$^+$ cells in the proliferative layer and an increased SOX2$^+$ layer thickness (Figures 5L, 5M, and S12J). Interestingly, treatment with chondroitinase ABC in rats upon spinal cord injury promotes CNS plasticity and regeneration.[61] FeBOs exposed to 4-methylumbelliferone (inhibiting hyaluronan synthesis) markedly reduced their growth (Figure 5K). Strikingly, these FeBOs displayed inverted polarity and layered organization with TUJ1$^+$ neurons presenting on the outside, suggesting a role of hyaluronan in controlling neuronal migration and establishment of tissue polarity (Figures 5N and 5O). Taken together,

Figure 5. Tissue integrity promotes the generation of a tissue-like ECM niche in FeBOs

(A) Pie charts depicting the relative mRNA expression of ECM-related components in expanding FeBOs (average across n = 25 FeBOs from different donors and different culture ages) and human fetal brain tissue, based on bulk RNA sequencing.

(B) Heatmaps showing the relative mRNA expression of ECM components within FeBOs and within human fetal brain and comparison with relative protein abundance in human fetal brain based on proteomic analysis from this study and from Kim et al.[58]

(C) Experimental set-up to analyze secreted ECM components by FeBOs.

(D) Ranked normalized abundance of detected matrisome proteins in the FeBO secretome (secreted products).

(E) Experimental conditions to evaluate how tissue integrity influences ECM production (top). Suggested model how tissue integrity ensures FeBO expansion (bottom).

(F) Heatmap comparing the normalized abundance of secreted ECM components between FeBOs (steady-state and upon splitting) and dissociated FeBO single-cell-derived neurospheres. n = 3 replicates per condition.

(G) Experimental conditions analyzing the proteomes of human fetal brain tissue, FeBOs, and PSC-derived 3D brain models, including a matrix-free (PSC-cortical spheroids) and matrix-containing (unguided PSC-cerebral organoids) protocol.

(H) PCA on ECM proteomes of human fetal brain tissue, FeBOs, PSC-cortical spheroids, and unguided PSC-cerebral organoids. n = 3 replicates per condition.

(I) Correlation plot comparing ECM proteomes across the different samples.

(J) Heatmaps depicting the relative protein abundance of ECM components in each experimental condition.

(K) Quantification of the FeBO growth ratio based on organoid area measurements upon challenge with different ECM perturbation molecules relative to control. Each dot represents a FeBO. $^{**}p < 0.01$; Student's t test.

(L) Representative immunofluorescence images for Ki-67 showing increased proliferation in chondroitinase ABC-exposed FeBOs. Scale bars, 150 μm.

(M) Quantification of the percentage of Ki-67$^+$ cells over DAPI$^+$ (top) and the thickness of the SOX2 layer (bottom) in control and chondroitinase ABC-exposed FeBOs. $^{***}p < 0.001$; Student's t test.

(N) Representative immunofluorescence images for SOX2 and TUJ1 showing changed cell distribution in 4-methylumbelliferone-exposed FeBOs. Scale bars, 150 μm.

(O) Quantification of cell type distribution within control and 4-methylumbelliferone-exposed FeBOs. Organoids were subdivided in multiple bins (from edge to center), and the number of cells (SOX2) or fluorescence intensity (TUJ1) in each bin was quantified.

See also Figures S12 and S13.

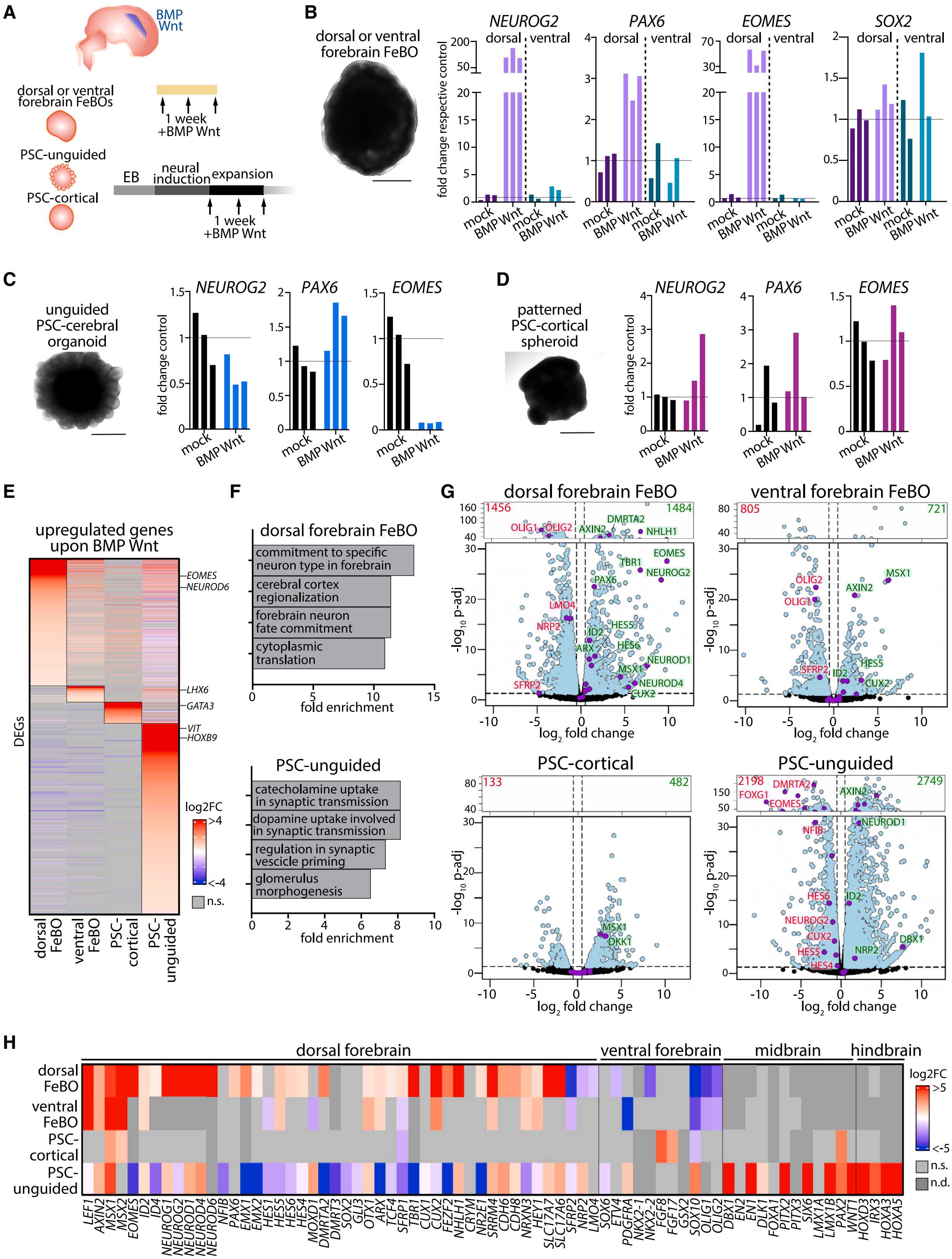

(legend on next page)

FeBOs maintain a developing tissue-like ECM niche, enabling functional ECM studies in human brain development.

Morphogen responses of endogenously specified human fetal brain identities assessed in FeBOs

During brain development, complex morphogen gradients are known to establish cellular and regional identity.[62,63] Whether the same morphogens affect the maintenance of positional identity is less established. Similarly, it remains unclear if established positional identities are hardwired or plastic, especially in human development. We probed if FeBOs could be useful to study the consequences of morphogen exposure on their endogenously specified identity. We utilized a combination of BMP and Wnt stimulation, dorsalizing signaling molecules in the neural tube and later on produced by the cortical hem to induce dorsomedial fate,[62,64,65] and assessed responses of both dorsal and ventral forebrain FeBOs (Figure 6A). We also studied the effect of the same molecules on unguided and cortex-patterned PSC-derived brain organoids, which are instead exogenously specified starting from the PSC state (Figures 6A, S13A, and S13B).

After 7 days of BMP+Wnt exposure, expanding dorsal FeBO lines robustly induced dorsal forebrain-specific genes (*PAX6*, *EOMES,* and *NEUROG2*) as compared with control FeBOs, while expression of the pan-NSC marker *SOX2* remained unchanged (Figure 6B). Remarkably, BMP+Wnt-exposed ventral FeBO lines did not show expression changes in any of these markers (Figure 6B). Neither the unguided PSC-cerebral organoids nor the PSC-cortical spheroids induced these dorsal markers upon BMP+Wnt stimulation (Figures 6C and 6D). We next analyzed the models' broad transcriptomic responses by bulk RNA sequencing. Visualization of the expression trends of the differentially expressed genes across all models highlighted their largely unique responses (Figures 6E, S13C, and S13D; Table S1). Ventral forebrain FeBOs and PSC-cortical spheroids responded with smaller (but unique) gene sets, while dorsal forebrain FeBOs and unguided PSC-cerebral organoids each displayed large, upregulated gene sets, mostly not overlapping (Figure 6E). GO-term enrichment analysis on upregulated gene sets revealed enrichment for cerebral cortex regionalization and forebrain neuron fate commitment in dorsal forebrain FeBOs, possibly in alignment with the reported physiological role of BMP and Wnt in the telencephalon[62–65] (Figures 6F and S13E). All models responded to Wnt and BMP signaling activation by upregulating bona fide Wnt and BMP target genes (e.g., *AXIN2*, *DKK1*, *LEF1* and *ID2*, *MSX1*, respectively). Upon inspection of expression of regional and cell type-specific genes, we observed upregulation of typical cortical genes in the dorsal forebrain FeBOs, including markers for dorsal intermediate progenitors (*EOMES*, *NHLH1*, and *NEUROG2*), neurogenic genes in NSCs (*ID4*, *HES5*), markers for early- and late-born glutamatergic cortical neurons (*SLC17A6*, *TBR1*, and *NEUROD6*), and different cortical neuronal subtypes/layer-specific genes, such as deep-layer (*FEZF2*, *CTIP2*, *SOX5*, *NFIA*, *NFIB*, *CELF1*, and *TLE4*) and upper-layer markers (*POU3F2*, *CDH6*, *CUX1/2*, *BHLHE22*, and *PLXNA4*)[45,50,66,67] (Figures 6G and 6H; Tables S1 and S2). Expression of dorsomedial markers (*LEF1*, *EMX1/2*, *GLI3*, *PAX6*, and *DMRTA2*) increased, while some markers of the lateral cortex (anti-hem) and ventral forebrain—the most distant regions from the BMP-Wnt gradient *in vivo*—appeared downregulated (*SFRP2*, *NRP2*, *LMO4*, *SOX10*, and *OLIG2*) (Figures 6G and 6H). These data suggested a strengthening of cortical fate and cellular diversity in dorsal forebrain FeBOs, including the induction of lowly expressed dorsal markers, implying that BMP+Wnt signaling might be needed for the maintenance of full cortical identity as optimized culture condition. Interestingly, ventral forebrain FeBOs did not respond in a similar manner, suggesting that these signals per se are not able to determine a ventral-to-dorsal forebrain fate change (Figures 6G, 6H, and S13F), highlighting aspects of plasticity of established ventral forebrain identity.

BMP+Wnt exposure did not induce changes in most of the regional genes in PSC-cortical spheroids in the experimental layout considered (Figures 6G and 6H). Unguided PSC-cerebral organoids presented a different response in regional fate, with upregulation of some mid- and hindbrain markers (e.g., *EN1*, *PITX2*, and *HOXA* genes), possibly reflecting the caudalization effect of BMP and Wnt during early stages of neural development.[68–70] Concomitantly, we noted a more varied expression trend of dorsal forebrain markers (Figures 6G and 6H).

Figure 6. FeBOs display physiologically relevant morphogen sensitivity

(A) Experimental setup to evaluate morphogen responses of dorsal and ventral forebrain FeBOs, unguided PSC-cerebral organoids, and PSC-cortical spheroids upon exposure to BMP+Wnt (BMP4 + CHIR-99021).

(B) Representative brightfield image of a FeBO (left) and mRNA expression analysis (qPCR) of *NEUROG2*, *PAX6*, *EOMES*, and general stem cell marker *SOX2* upon BMP+Wnt exposure relative to mock (control) in 3-month-expanded dorsal and ventral forebrain FeBOs. Each bar represents an individual FeBO. Scale bars, 1 mm.

(C) Representative brightfield image of an unguided PSC-cerebral organoid (left) and mRNA expression analysis (qPCR) of *NEUROG2*, *PAX6*, and *EOMES* upon BMP+Wnt exposure relative to mock (control). Each bar represents an individual organoid. Scale bars, 500 μm.

(D) Representative brightfield image of a PSC-cortical spheroid (left) and mRNA expression analysis (qPCR) of *NEUROG2*, *PAX6*, and *EOMES* upon BMP+Wnt exposure relative to mock (control). Each bar represents an individual spheroid. Scale bars, 500 μm.

(E) Heatmap displaying expression trends across all models upon BMP+Wnt exposure of all upregulated genes ($|\log_2 FC| > 0.5$, p-adj. < 0.05) identified in each experimental model vs. its respective control. n.s., not significant.

(F) GO-term enrichment analysis on the upregulated genes identified in dorsal forebrain FeBOs (top) and in unguided PSC-cerebral organoids (bottom) upon BMP+Wnt exposure.

(G) Volcano plots of the differentially expressed genes identified in each experimental model upon BMP+Wnt exposure. Blue dots indicate statistically significant genes. The number of upregulated (green) and downregulated (red) genes are indicated.

(H) Heatmap displaying the log2FC trends of selected markers of different brain regions across all experimental models upon BMP+Wnt exposure. n.s., not significant; n.d., not detected.

See also Figure S13.

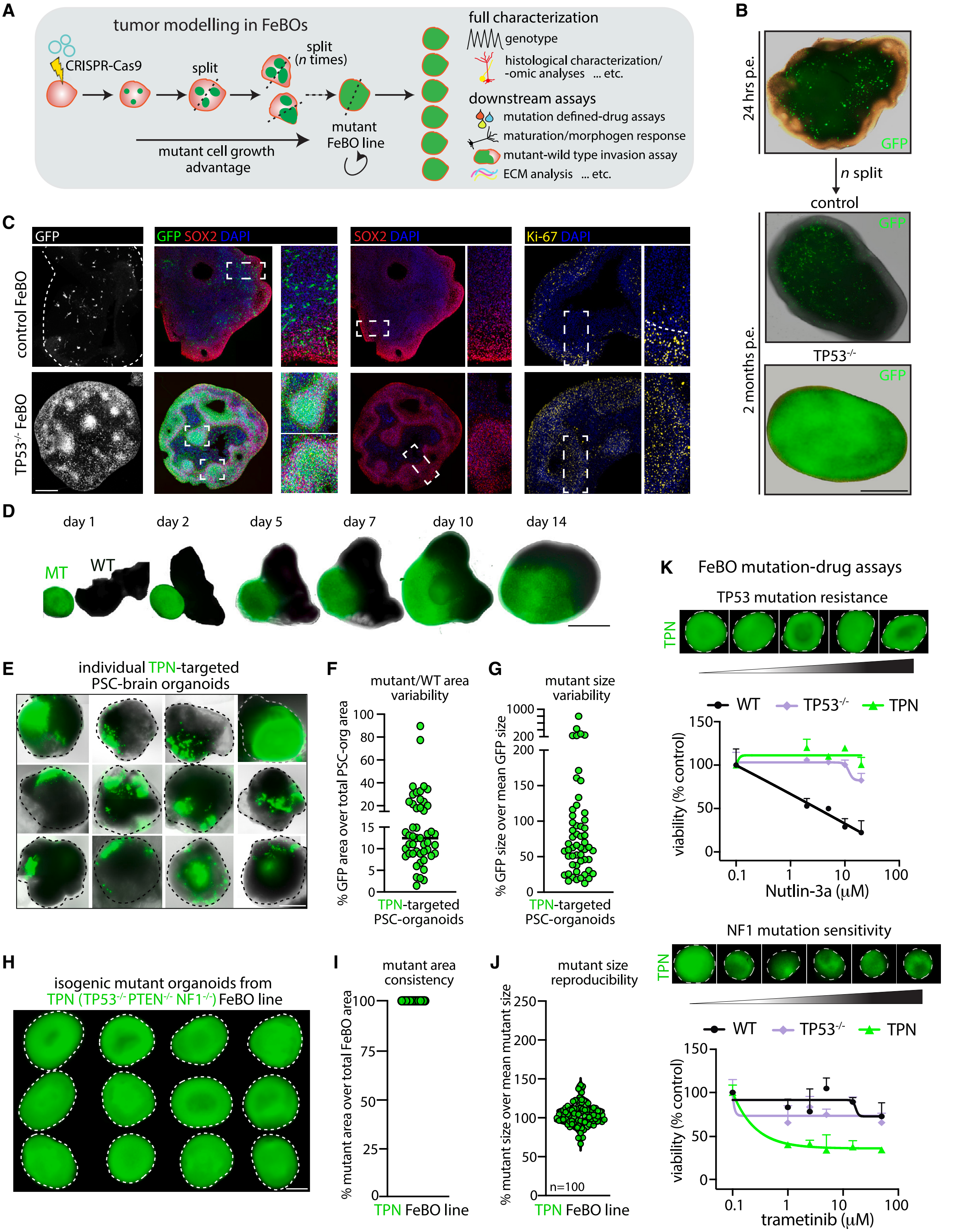

(legend on next page)

Our data uncover divergent morphogen responses between PSC-brain models and tissue-derived FeBOs. These differences may find their origin in the native vs. exogenously guided brain region identity, and a different level of cellular plasticity. Effect of morphogens during brain development are different depending on the developmental window.[63,71] In this context, the FeBOs represent a complementary *in vitro* model to study the effect of signaling molecules on maintenance and plasticity of native, *in vivo* established regional identities.

Scalable CRISPR-engineered mutant FeBO lines for brain tumor modeling

We investigated whether FeBOs allow disease modeling by CRISPR editing,[72] first focusing on a developmental gene. *RAB3GAP2* mutations are associated with Warburg Micro or Martsolf syndromes, characterized by microcephaly,[73,74] and its expression decreases along the developmental trajectory (Figures S14A and S14B). By CRISPR-engineering FeBOs through whole-organoid electroporation (Figure S14C), we introduced *RAB3GAP2* mutations in cells co-transfected with a transposable GFP. Transfected cells were mainly located in the stem/progenitor outside region (Figures S14D and S14E). This allowed following their fate and that of their daughter cells upon gene manipulation.[75] A conspicuous decrease of SOX2$^+$ and PAX6$^+$ stem cells and a concomitant proportional increase of the neuronal TUJ1$^+$ and MAP2$^+$ populations were observed within the targeted GFP$^+$ population (Figures S14F–S14I). These observations suggested that loss of RAB3GAP2 leads to an unbalanced fate of progenitor maintenance vs. neuronal differentiation (Figure S14J).

We reasoned that FeBOs would allow to visualize the effect of mutating cancer genes in sporadic cells within an otherwise healthy developing brain (Figure 7A). We first introduced knockout mutations in *TP53*. A small number of cells were initially targeted (GFP$^+$) (Figure 7B). During subsequent expansion and repeated splitting (ca. 2–3 months), a sharp increase of GFP$^+$ cells in TP53-targeted organoids was seen, which was not observed in control conditions (Figure 7B), revealing a clear growth advantage of *TP53*-mutant cells. These mutant organoids contained increased proliferative GFP$^+$/SOX2$^+$ cells, which appeared to grow in a nodule-like fashion (Figure 7C). GFP$^+$ (*TP53*$^{-/-}$) cells repressed expression of the downstream target TP21 (Figure S15A) and remained proliferative also upon maturation (Figures S15B and S15C), suggesting impaired differentiation (Figure S15D). Over time, mutant FeBOs became fully GFP$^+$, and clonal *TP53* frameshift mutations were confirmed (Figures S15E and S15F). To further probe their tumorigenic behavior, we established co-cultures between mutant FeBOs (GFP$^+$) and wild-type FeBOs (GFP$^-$) derived from the same donor. Hybrid organoids were quickly formed, and GFP$^+$ cells markedly invaded the wild-type FeBO (Figure 7D), illustrating their potential to study mutant brain cell invasiveness.

Tumor modeling has been reported in PSC-brain organoids,[76] but their application for extensive drug screening is complex due to organoid-to-organoid variation in terms of the extent and size of the grown GFP$^+$ area and the lack of passaging capacity (Figures 7E–7G and S15G–S15I). Single CRISPR-mutated FeBOs can each generate multiple, identical mutant organoids (i.e., clonal lines) amenable for multiple downstream analyses in a scalable and reproducible manner (Figures 7A and S15G). We generated a triple knockout of *TP53*, *PTEN*, and *NF1* (TPN), a classical combination for glioblastoma modeling.[77] After ca. 3 months, TPN (GFP$^+$) FeBO lines were derived, and isogenic, clonal TPN FeBOs could be split into a large number of organoids of similar size, which were solely composed of mutant cells (Figures 7H–7J). To show the applicability of such mutant FeBO lines, we performed mutation-drug sensitivity assays, based on methods compatible with higher throughput (i.e., ATP-based viability assays). Dose-response curves for afatinib and everolimus were reliably generated with minimal inter-organoid variation (Figure S15J). We then exposed both TPN FeBOs, single *TP53*$^{-/-}$ FeBOs, and wild-type FeBOs to Nutlin-3a. TP53-mutant cells should be resistant to Nutlin-3a.[78] Indeed, TPN FeBOs as well as single *TP53*$^{-/-}$ FeBOs were resistant to Nutlin-3a, while wild-type organoids displayed reduced viability already at the lowest dose tested (Figures 7K and S15J). We also evaluated responses to the MEK inhibitor trametinib,[79] to which *NF1*-mutant cells should be sensitive. While wild-type FeBOs and single *TP53*$^{-/-}$ FeBOs displayed near-complete resistance, TPN FeBOs displayed marked sensitivity

Figure 7. FeBOs enable robust tumor modeling

(A) Principle of tumor modeling in FeBOs using genetic engineering and examples of downstream analyses.

(B) Representative brightfield and GFP fluorescence overlay image of sparsely transfected (GFP$^+$) cells 24 h post electroporation (p.e.) in whole FeBOs. Upon TP53 knockout, *TP53*$^{-/-}$; GFP$^+$ cells rapidly and exclusively enrich over time. Scale bars, 1 mm.

(C) Representative immunofluorescence images for the indicated markers in control FeBOs and FeBOs in which *TP53*$^{-/-}$; GFP$^+$ cells have rapidly enriched at two months p.e. (*TP53*$^{-/-}$ FeBO). Scale bars, 500 μm.

(D) Representative brightfield and GFP fluorescence overlay images of an invasion assay of a *TP53*$^{-/-}$ mutant (MT, GFP$^+$) FeBO on a wild-type (WT) FeBO. Scale bars, 1 mm.

(E) Representative brightfield and GFP fluorescence overlay images of individual TPN-targeted PSC-brain organoids. Scale bars, 500 μm.

(F) Quantification of the percentage of mutant area over whole organoid area of individual TPN-targeted PSC-brain organoids (dots).

(H) Quantification of the mutant area size variability across individual TPN-targeted PSC-brain organoids (dots).

(H) Representative GFP fluorescence images of individual isogenic organoids from a TPN FeBO line. Scale bars, 500 μm.

(I) Quantification of the percentage of mutant area over whole organoid area of TPN FeBOs (dots).

(J) Quantification of the organoid-to-organoid size variability of TPN FeBOs (dots).

(K) FeBO mutation-drug assays. Representative GFP fluorescence images of TPN FeBOs in response to increasing doses of Nutlin-3a (top) or trametinib (bottom). Underneath, ATP-based viability curves of wild-type (WT), single mutant *TP53*$^{-/-}$, and triple mutant TPN FeBOs after 7 days Nutlin-3a (top) or trametinib (bottom) exposure (mean ± SD).

See also Figures S14 and S15.

(Figures 7K and S15J). Altogether, FeBOs constitute a versatile platform for brain cancer modeling.

DISCUSSION

Experimental platforms of human brain have flourished in recent years, most notably due to the emerging PSC-brain organoid models.[80] The continued advancement of different protocols and exhaustive characterizations through various single-cell technologies have emphasized their promise and reliability.[45,81–84] Among others, PSC-brain organoids have unraveled intricate details of human brain development, including evolutionary[44,85–87] and disease-related aspects[88–90].

Approximation of the complexity of *in vivo* biology inherently benefits from the continued establishment of novel models. Here, we demonstrate that small fragments of human fetal brain tissue can be expanded over long periods of time under defined culture conditions as organoids (FeBOs), with reliable molecular profiles and cellular heterogeneity. We thus find that the human developing brain is capable of robustly self-organizing *in vitro* over multiple passages into a 3D, layered structure. In these FeBOs, progenitor cells localize to the organoid periphery, while neurogenesis occurs toward the center, creating a self-sustaining organoid system. Importantly, FeBOs are of exclusive neuroectoderm composition. Notably, a key finding of our study is that the preservation of tissue integrity and thus of native cell-cell interactions appear instrumental to produce a proper tissue-like ECM niche, which we hypothesize might be important to maintain long-term expansion. This argues that intact germinal zones of the human brain are self-proficient in the creation of the proper local environment, which in turn regulates tissue growth. In line, functional perturbation of the ECM niche directly influenced FeBO growth and cellular organization.

Through histological and transcriptomic characterizations as well as direct comparisons with primary tissue, we show that FeBOs recapitulate aspects of human fetal brain across multiple lines and donors, including cellular diversity (including abundant oRGs) and transcriptional identities. Differently than PSC-derived brain models, FeBOs do not naturally progress to later stages in development and appear to represent expanding ‘‘avatars’’ of the tissue from which they derive. This enables the generation of expanding FeBO lines (i.e., one FeBO generates multiple FeBOs upon passaging, all derived from the same donor and same initial fragment), facilitating reproducibility for downstream applications. When placed in maturation medium, FeBOs slow down their growth, while features occurring later in development, such as gliogenesis, become more prominent.

FeBOs can be derived from distinct parts of the CNS while broadly capturing the original regional identity over prolonged periods of time. The distinct behavior of FeBOs derived from dorsal vs. ventral forebrain upon exposure to dorsalizing signaling agents suggests that they may also capture distinct regional responses. This hints at the application of FeBOs as an experimental platform to address cell-autonomous and morphogen-dependent mechanisms of cell and positional identity specification in a naturally specified human *in vitro* system.

We further demonstrate the use of the FeBO culture system to address disease-related questions. In particular, expandable CRISPR-mutated FeBO lines with defined genetic make-ups can be generated as bottom-up cancer models. Such mutant FeBO lines represent scalable and reproducible systems amenable to a plethora of functional screenings, including mutation-drug sensitivity assays.

The advances on *in vitro* experimental human brain models require proactive assessment of the ethical and societal challenges, ranging from consent to the emerging questions of the possible consciousness and pain-sensing of such models. We established FeBOs from abortion material from anonymous individuals that donated voluntarily and without any compensation. FeBOs were generated from tissue ages up to GW15, spanning the beginning of the second trimester. It is highly unlikely that FeBOs would possess consciousness or alike perceptive properties, given the lack of sensory inputs, outbound connections, and complex brain region interactions.[91] Similar to active discussions on other human brain models,[92] the use of dedicated research ethics frameworks and active discussions with donors and the scientific community should be ensured to continue ethical forms of further experimentation using FeBOs, including organoid xenotransplantation, similar to PSC-brain organoid grafts in rodent brains.[93–95]

Limitations of the study

The FeBO platform opens up an independent avenue to study the human fetal brain in health and disease but is inherently dependent on fetal tissue access. There are various aspects that will require future optimizations, and follow-up directions can be envisioned. Among others, these may regard aspects of characterization and improvement of neuronal specification and electrophysiological properties, the development of more gradual and prolonged maturation protocols specific per regional FeBO, and the appearance of a more tightly organized layer cytoarchitecture. Intriguingly, we noted a strong and specific regional response of dorsal forebrain FeBOs to supplementation of dorsalizing agents (BMP and Wnt). This is an aspect that should be further explored, also with regard to other regional FeBOs. In fact, it would be of interest to further investigate if FeBOs can be derived from brain regions other than the forebrain and if there are diverse requirements for specific signaling molecules to maintain/strengthen regional identities *in vitro*. Although this would necessitate testing of different culture conditions, it would provide novel insights into the plasticity of positional identity and simultaneously constitute optimized culture conditions. In parallel, it would be of interest to investigate whether FeBOs can be derived from a broader developmental window than tested here (GW12–15), whether these show differences in expansion capacity and cell types, and whether they can reflect temporal patterning of neurogenesis, e.g., through lineage tracing analysis. Lastly, derivation of FeBOs from diseased tissues would be of particular interest for brain defects that are associated with perinatal lethality.

STAR★METHODS

Detailed methods are provided in the online version of this paper and include the following:

- KEY RESOURCES TABLE

- RESOURCE AVAILABILITY
  - ○ Lead contact
  - ○ Materials availability
  - ○ Data and code availability
- EXPERIMENTAL MODEL AND STUDY PARTICIPANT DETAILS
  - ○ Human tissue
  - ○ Human embryonic stem cells
- METHOD DETAILS
  - ○ Tissue isolation, dissection, and processing for organoid culture
  - ○ FeBO establishment and long-term culturing
  - ○ FeBOs growth assessment
  - ○ Organoid and brain tissue processing for immunofluorescence
  - ○ Lentiviral infection of FeBOs
  - ○ ECM perturbations in FeBOs
  - ○ Morphogen treatment on FeBOs and PSC-derived 3D brain models
  - ○ Sparse cell labeling of FeBOs
  - ○ Measurement of calcium flux by live imaging
  - ○ CRISPR-editing, brain tumor modelling, and drug screening in FeBOs
  - ○ Generation of PSC-derived 3D brain models
  - ○ Brain tumor modelling and drug screening in PSC-derived brain organoids
  - ○ Confocal imaging, analysis, and quantification
  - ○ Transmission electron microscopy
  - ○ RNA extraction and qPCR analysis
  - ○ Bulk RNA sequencing, analysis, and deconvolution
  - ○ Single-cell RNA sequencing and bioinformatic analysis
  - ○ Single-cell RNA sequencing comparison with primary human fetal brain tissue
  - ○ Secretome and proteome analysis by LC-MS/MS
- QUANTIFICATION AND STATISTICAL ANALYSIS

SUPPLEMENTAL INFORMATION

Supplemental information can be found online at https://doi.org/10.1016/j.cell.2023.12.012.

ACKNOWLEDGMENTS

We thank Willine van de Wetering and Eduard Bodewes for technical support, Dr. Wim de Lau and Joost Wijnakker for discussions, and Drs. Marcel Kool and Jens Bunt for resources. We thank Drs. Steve Lisgo and Nita Solanky and their teams at HDBR for their invaluable support. D.H. is supported by an NWO VENI grant (VI.Veni.212.134). Part of this work is supported by an NWO Open Competition Science-M grant (B.A.).

AUTHOR CONTRIBUTIONS

Conceptualization, supervision, and writing: D.H., H.C., and B.A.; methodology, visualization, and data curation: D.H. and B.A.; formal analysis: D.H., W.W., and B.A.; investigation: D.H., A.P., F.A., Z.M., J.v.G., S.M., C.L.-I., J.D.M., J.M.A.D., I.Z., N.S., S.C.d.S.L., W.W., and B.A.; resources: D.H., G.J.F.v.S., A.L.B., F.C.P.H., P.J.P., T.M., S.C.d.S.L., H.C., and B.A.; project administration: D.H., S.C.d.S.L., W.W., H.C., and B.A.; funding acquisition: H.C. and B.A.

DECLARATION OF INTERESTS

D.H., B.A., and H.C. are inventors on a patent related to this work. The full disclosure of H.C. is given at https://www.uu.nl/staff/JCClevers/.

Received: December 13, 2022
Revised: September 27, 2023
Accepted: December 5, 2023
Published: January 8, 2024

REFERENCES

1. Fujii, M., and Sato, T. (2021). Somatic cell-derived organoids as prototypes of human epithelial tissues and diseases. Nat. Mater. *20*, 156–169.
2. Kim, J., Koo, B.K., and Knoblich, J.A. (2020). Human organoids: model systems for human biology and medicine. Nat. Rev. Mol. Cell Biol. *21*, 571–584.
3. McCauley, H.A., and Wells, J.M. (2017). Pluripotent stem cell-derived organoids: using principles of developmental biology to grow human tissues in a dish. Development *144*, 958–962.
4. Sato, T., Stange, D.E., Ferrante, M., Vries, R.G.J., van Es, J.H., van den Brink, S., van Houdt, W.J., Pronk, A., van Gorp, J., Siersema, P.D., et al. (2011). Long-term expansion of epithelial organoids from human colon, adenoma, adenocarcinoma, and Barrett's epithelium. Gastroenterology *141*, 1762–1772.
5. Huch, M., Gehart, H., van Boxtel, R., Hamer, K., Blokzijl, F., Verstegen, M.M.A., Ellis, E., van Wenum, M., Fuchs, S.A., de Ligt, J., et al. (2015). Long-term culture of genome-stable bipotent stem cells from adult human liver. Cell *160*, 299–312.
6. Hu, H., Gehart, H., Artegiani, B., Löpez-Iglesias, C., Dekkers, F., Basak, O., van Es, J., Chuva de Sousa Lopes, S.M., Begthel, H., Korving, J., et al. (2018). Long-term expansion of functional mouse and human hepatocytes as 3D organoids. Cell *175*, 1591–1606.e19.
7. Hendriks, D., Artegiani, B., Hu, H., Chuva de Sousa Lopes, S., and Clevers, H. (2021). Establishment of human fetal hepatocyte organoids and CRISPR–Cas9-based gene knockin and knockout in organoid cultures from human liver. Nat. Protoc. *16*, 182–217.
8. Fordham, R.P., Yui, S., Hannan, N.R.F., Soendergaard, C., Madgwick, A., Schweiger, P.J., Nielsen, O.H., Vallier, L., Pedersen, R.A., Nakamura, T., et al. (2013). Transplantation of expanded fetal intestinal progenitors contributes to colon regeneration after injury. Cell Stem Cell *13*, 734–744.
9. Lim, K., Donovan, A.P.A., Tang, W., Sun, D., He, P., Pett, J.P., Teichmann, S.A., Marioni, J.C., Meyer, K.B., Brand, A.H., et al. (2023). Organoid modeling of human fetal lung alveolar development reveals mechanisms of cell fate patterning and neonatal respiratory disease. Cell Stem Cell *30*, 20–37.e9.
10. Hofer, M., and Lutolf, M.P. (2021). Engineering organoids. Nat. Rev. Mater. *6*, 402–420.
11. Molnár, Z., Métin, C., Stoykova, A., Tarabykin, V., Price, D.J., Francis, F., Meyer, G., Dehay, C., and Kennedy, H. (2006). Comparative aspects of cerebral cortical development. Eur. J. Neurosci. *23*, 921–934.
12. Molnár, Z., Clowry, G.J., Šestan, N., Alzu'bi, A., Bakken, T., Hevner, R.F., Hüppi, P.S., Kostović, I., Rakic, P., Anton, E.S., et al. (2019). New insights into the development of the human cerebral cortex. J. Anat. *235*, 432–451.
13. Pinson, A., and Huttner, W.B. (2021). Neocortex expansion in development and evolution-from genes to progenitor cell biology. Curr. Opin. Cell Biol. *73*, 9–18.
14. Zhou, Y., Song, H., and Ming, G.L. (2024). Genetics of human brain development. Nat. Rev. Genet. *25*, 26–45.
15. Hogue, M.J. (1947). Human fetal brain cells in tissue cultures; their identification and motility. J. Exp. Zool. *106*, 85–107.

16. Schwartz, P.H., Bryant, P.J., Fuja, T.J., Su, H., O'Dowd, D.K., and Klassen, H. (2003). Isolation and characterization of neural progenitor cells from post-mortem human cortex. J. Neurosci. Res. *74*, 838–851.

17. Ray, B., Chopra, N., Long, J.M., and Lahiri, D.K. (2014). Human primary mixed brain cultures: preparation, differentiation, characterization and application to neuroscience research. Mol. Brain *7*, 63.

18. Carpenter, M.K., Cui, X., Hu, Z.Y., Jackson, J., Sherman, S., Seiger, A., and Wahlberg, L.U. (1999). In vitro expansion of a multipotent population of human neural progenitor cells. Exp. Neurol. *158*, 265–278.

19. Humpel, C. (2015). Organotypic brain slice cultures: a review. Neuroscience *305*, 86–98.

20. Qian, X., Song, H., and Ming, G.L. (2019). Brain organoids: advances, applications and challenges. Development *146*.

21. Chiaradia, I., and Lancaster, M.A. (2020). Brain organoids for the study of human neurobiology at the interface of in vitro and in vivo. Nat. Neurosci. *23*, 1496–1508.

22. Eichmüller, O.L., and Knoblich, J.A. (2022). Human cerebral organoids - a new tool for clinical neurology research. Nat. Rev. Neurol. *18*, 661–680.

23. Fernández, V., Llinares-Benadero, C., and Borrell, V. (2016). Cerebral cortex expansion and folding: what have we learned? EMBO J. *35*, 1021–1044.

24. Miller, D.J., Bhaduri, A., Sestan, N., and Kriegstein, A. (2019). Shared and derived features of cellular diversity in the human cerebral cortex. Curr. Opin. Neurobiol. *56*, 117–124.

25. Silbereis, J.C., Pochareddy, S., Zhu, Y., Li, M., and Sestan, N. (2016). The cellular and molecular landscapes of the developing human central nervous system. Neuron *89*, 248–268.

26. Sun, Y., Pollard, S., Conti, L., Toselli, M., Biella, G., Parkin, G., Willatt, L., Falk, A., Cattaneo, E., and Smith, A. (2008). Long-term tripotent differentiation capacity of human neural stem (NS) cells in adherent culture. Mol. Cell. Neurosci. *38*, 245–258.

27. Jensen, J.B., and Parmar, M. (2006). Strengths and limitations of the neurosphere culture system. Mol. Neurobiol. *34*, 153–161.

28. Pollen, A.A., Nowakowski, T.J., Chen, J., Retallack, H., Sandoval-Espinosa, C., Nicholas, C.R., Shuga, J., Liu, S.J., Oldham, M.C., Diaz, A., et al. (2015). Molecular identity of human outer radial glia during cortical development. Cell *163*, 55–67.

29. Fietz, S.A., Kelava, I., Vogt, J., Wilsch-Bräuninger, M., Stenzel, D., Fish, J.L., Corbeil, D., Riehn, A., Distler, W., Nitsch, R., et al. (2010). OSVZ progenitors of human and ferret neocortex are epithelial-like and expand by integrin signaling. Nat. Neurosci. *13*, 690–699.

30. Hansen, D.V., Lui, J.H., Parker, P.R.L., and Kriegstein, A.R. (2010). Neurogenic radial glia in the outer subventricular zone of human neocortex. Nature *464*, 554–561.

31. Jacob, F., Salinas, R.D., Zhang, D.Y., Nguyen, P.T.T., Schnoll, J.G., Wong, S.Z.H., Thokala, R., Sheikh, S., Saxena, D., Prokop, S., et al. (2020). A patient-derived glioblastoma organoid model and biobank recapitulates inter- and intra-tumoral heterogeneity. Cell *180*, 188–204.e22.

32. Shibata, M., Gulden, F.O., and Sestan, N. (2015). From trans to cis: transcriptional regulatory networks in neocortical development. Trends Genet. *31*, 77–87.

33. Wonders, C.P., and Anderson, S.A. (2006). The origin and specification of cortical interneurons. Nat. Rev. Neurosci. *7*, 687–696.

34. Jakovcevski, I., and Zecevic, N. (2005). Olig transcription factors are expressed in oligodendrocyte and neuronal cells in human fetal CNS. J. Neurosci. *25*, 10064–10073.

35. Petryniak, M.A., Potter, G.B., Rowitch, D.H., and Rubenstein, J.L.R. (2007). Dlx1 and Dlx2 control neuronal versus oligodendroglial cell fate acquisition in the developing forebrain. Neuron *55*, 417–433.

36. Le, T.N., Zhou, Q.P., Cobos, I., Zhang, S., Zagozewski, J., Japoni, S., Vriend, J., Parkinson, T., Du, G., Rubenstein, J.L., et al. (2017). GABAergic interneuron differentiation in the basal forebrain is mediated through direct regulation of glutamic acid decarboxylase isoforms by *Dlx* homeobox transcription factors. J. Neurosci. *37*, 8816–8829.

37. Bhaduri, A., Sandoval-Espinosa, C., Otero-Garcia, M., Oh, I., Yin, R., Eze, U.C., Nowakowski, T.J., and Kriegstein, A.R. (2021). An atlas of cortical arealization identifies dynamic molecular signatures. Nature *598*, 200–204.

38. Nowakowski, T.J., Bhaduri, A., Pollen, A.A., Alvarado, B., Mostajo-Radji, M.A., di Lullo, E., Haeussler, M., Sandoval-Espinosa, C., Liu, S.J., Velmeshev, D., et al. (2017). Spatiotemporal gene expression trajectories reveal developmental hierarchies of the human cortex. Science *358*, 1318–1323.

39. Clevers, H. (2016). Modeling development and disease with organoids. Cell *165*, 1586–1597.

40. Lysko, D.E., Putt, M., and Golden, J.A. (2011). SDF1 regulates leading process branching and speed of migrating interneurons. J. Neurosci. *31*, 1739–1745.

41. Shi, Y., Wang, M., Mi, D., Lu, T., Wang, B., Dong, H., Zhong, S., Chen, Y., Sun, L., Zhou, X., et al. (2021). Mouse and human share conserved transcriptional programs for interneuron development. Science *374*, eabj6641.

42. Yu, Y., Zeng, Z., Xie, D., Chen, R., Sha, Y., Huang, S., Cai, W., Chen, W., Li, W., Ke, R., et al. (2021). Interneuron origin and molecular diversity in the human fetal brain. Nat. Neurosci. *24*, 1745–1756.

43. Naka, H., Nakamura, S., Shimazaki, T., and Okano, H. (2008). Requirement for COUP-TFI and II in the temporal specification of neural stem cells in CNS development. Nat. Neurosci. *11*, 1014–1023.

44. Pollen, A.A., Bhaduri, A., Andrews, M.G., Nowakowski, T.J., Meyerson, O.S., Mostajo-Radji, M.A., di Lullo, E., Alvarado, B., Bedolli, M., Dougherty, M.L., et al. (2019). Establishing cerebral organoids as models of human-specific brain evolution. Cell *176*, 743–756.e17.

45. Uzquiano, A., Kedaigle, A.J., Pigoni, M., Paulsen, B., Adiconis, X., Kim, K., Faits, T., Nagaraja, S., Antón-Bolaños, N., Gerhardinger, C., et al. (2022). Proper acquisition of cell class identity in organoids allows definition of fate specification programs of the human cerebral cortex. Cell *185*, 3770–3788.e27.

46. Namba, T., Nardelli, J., Gressens, P., and Huttner, W.B. (2021). Metabolic regulation of neocortical expansion in development and evolution. Neuron *109*, 408–419.

47. Xiang, Y., Tanaka, Y., Patterson, B., Kang, Y.J., Govindaiah, G., Roselaar, N., Cakir, B., Kim, K.Y., Lombroso, A.P., Hwang, S.M., et al. (2017). Fusion of regionally specified hPSC-derived organoids models human brain development and interneuron migration. Cell Stem Cell *21*, 383–398.e7.

48. Blaesse, P., Airaksinen, M.S., Rivera, C., and Kaila, K. (2009). Cation-chloride cotransporters and neuronal function. Neuron *61*, 820–838.

49. Trevino, A.E., Müller, F., Andersen, J., Sundaram, L., Kathiria, A., Shcherbina, A., Farh, K., Chang, H.Y., Paşca, A.M., Kundaje, A., et al. (2021). Chromatin and gene-regulatory dynamics of the developing human cerebral cortex at single-cell resolution. Cell *184*, 5053–5069.e23.

50. Polioudakis, D., de la Torre-Ubieta, L., Langerman, J., Elkins, A.G., Shi, X., Stein, J.L., Vuong, C.K., Nichterwitz, S., Gevorgian, M., Opland, C.K., et al. (2019). A single-cell transcriptomic atlas of human neocortical development during mid-gestation. Neuron *103*, 785–801.e8.

51. Heavner, W.E., Ji, S., Notwell, J.H., Dyer, E.S., Tseng, A.M., Birgmeier, J., Yoo, B., Bejerano, G., and McConnell, S.K. (2020). Transcription factor expression defines subclasses of developing projection neurons highly similar to single-cell RNA-seq subtypes. Proc. Natl. Acad. Sci. USA *117*, 25074–25084.

52. Fan, X., Fu, Y., Zhou, X., Sun, L., Yang, M., Wang, M., Chen, R., Wu, Q., Yong, J., Dong, J., et al. (2020). Single-cell transcriptome analysis reveals cell lineage specification in temporal-spatial patterns in human cortical development. Sci. Adv. *6*, eaaz2978.

53. Amin, S., and Borrell, V. (2020). The extracellular matrix in the evolution of cortical development and folding. Front. Cell Dev. Biol. *8*, 604448.

54. Long, K.R., and Huttner, W.B. (2019). How the extracellular matrix shapes neural development. Open Biol. *9*, 180216.

55. Fietz, S.A., Lachmann, R., Brandl, H., Kircher, M., Samusik, N., Schröder, R., Lakshmanaperumal, N., Henry, I., Vogt, J., Riehn, A., et al. (2012). Transcriptomes of germinal zones of human and mouse fetal neocortex suggest a role of extracellular matrix in progenitor self-renewal. Proc. Natl. Acad. Sci. USA *109*, 11836–11841.

56. Cho, A.N., Jin, Y., An, Y., Kim, J., Choi, Y.S., Lee, J.S., Kim, J., Choi, W.Y., Koo, D.J., Yu, W., et al. (2021). Microfluidic device with brain extracellular matrix promotes structural and functional maturation of human brain organoids. Nat. Commun. *12*, 4730.

57. Esk, C., Lindenhofer, D., Haendeler, S., Wester, R.A., Pflug, F., Schroeder, B., Bagley, J.A., Elling, U., Zuber, J., von Haeseler, A., et al. (2020). A human tissue screen identifies a regulator of ER secretion as a brain-size determinant. Science *370*, 935–941.

58. Kim, M.S., Pinto, S.M., Getnet, D., Nirujogi, R.S., Manda, S.S., Chaerkady, R., Madugundu, A.K., Kelkar, D.S., Isserlin, R., Jain, S., et al. (2014). A draft map of the human proteome. Nature *509*, 575–581.

59. Lancaster, M.A., Renner, M., Martin, C.A., Wenzel, D., Bicknell, L.S., Hurles, M.E., Homfray, T., Penninger, J.M., Jackson, A.P., and Knoblich, J.A. (2013). Cerebral organoids model human brain development and microcephaly. Nature *501*, 373–379.

60. Paşca, A.M., Sloan, S.A., Clarke, L.E., Tian, Y., Makinson, C.D., Huber, N., Kim, C.H., Park, J.Y., O'Rourke, N.A., Nguyen, K.D., et al. (2015). Functional cortical neurons and astrocytes from human pluripotent stem cells in 3D culture. Nat. Methods *12*, 671–678.

61. Bradbury, E.J., Moon, L.D.F., Popat, R.J., King, V.R., Bennett, G.S., Patel, P.N., Fawcett, J.W., and McMahon, S.B. (2002). Chondroitinase ABC promotes functional recovery after spinal cord injury. Nature *416*, 636–640.

62. Sur, M., and Rubenstein, J.L.R. (2005). Patterning and plasticity of the cerebral cortex. Science *310*, 805–810.

63. Backman, M., Machon, O., Mygland, L., van den Bout, C.J., Zhong, W., Taketo, M.M., and Krauss, S. (2005). Effects of canonical Wnt signaling on dorso-ventral specification of the mouse telencephalon. Dev. Biol. *279*, 155–168.

64. Furuta, Y., Piston, D.W., and Hogan, B.L. (1997). Bone morphogenetic proteins (BMPs) as regulators of dorsal forebrain development. Development *124*, 2203–2212.

65. Caronia-Brown, G., Yoshida, M., Gulden, F., Assimacopoulos, S., and Grove, E.A. (2014). The cortical hem regulates the size and patterning of neocortex. Development *141*, 2855–2865.

66. Herring, C.A., Simmons, R.K., Freytag, S., Poppe, D., Moffet, J.J.D., Pflueger, J., Buckberry, S., Vargas-Landin, D.B., Clément, O., Echeverría, E.G., et al. (2022). Human prefrontal cortex gene regulatory dynamics from gestation to adulthood at single-cell resolution. Cell *185*, 4428–4447.e28.

67. Jourdon, A., Wu, F., Mariani, J., Capauto, D., Norton, S., Tomasini, L., Amiri, A., Suvakov, M., Schreiner, J.D., Jang, Y., et al. (2023). Modeling idiopathic autism in forebrain organoids reveals an imbalance of excitatory cortical neuron subtypes during early neurogenesis. Nat. Neurosci. *26*, 1505–1515.

68. Nordström, U., Jessell, T.M., and Edlund, T. (2002). Progressive induction of caudal neural character by graded Wnt signaling. Nat. Neurosci. *5*, 525–532.

69. Polevoy, H., Gutkovich, Y.E., Michaelov, A., Volovik, Y., Elkouby, Y.M., and Frank, D. (2019). New roles for Wnt and BMP signaling in neural anteroposterior patterning. EMBO Rep. *20*.

70. Mulligan, K.A., and Cheyette, B.N.R. (2012). Wnt signaling in vertebrate neural development and function. J. Neuroimmune Pharmacol. *7*, 774–787.

71. Gunhaga, L., Marklund, M., Sjödal, M., Hsieh, J.C., Jessell, T.M., and Edlund, T. (2003). Specification of dorsal telencephalic character by sequential Wnt and FGF signaling. Nat. Neurosci. *6*, 701–707.

72. Hendriks, D., Clevers, H., and Artegiani, B. (2020). CRISPR-Cas tools and their application in genetic engineering of human stem cells and organoids. Cell Stem Cell *27*, 705–731.

73. Borck, G., Wunram, H., Steiert, A., Volk, A.E., Körber, F., Roters, S., Herkenrath, P., Wollnik, B., Morris-Rosendahl, D.J., and Kubisch, C. (2011). A homozygous RAB3GAP2 mutation causes Warburg Micro syndrome. Hum. Genet. *129*, 45–50.

74. Handley, M.T., Morris-Rosendahl, D.J., Brown, S., Macdonald, F., Hardy, C., Bem, D., Carpanini, S.M., Borck, G., Martorell, L., Izzi, C., et al. (2013). Mutation spectrum in *RAB 3 GAP 1*, *RAB 3 GAP 2*, and *RAB 18* and genotype-phenotype correlations in Warburg micro syndrome and Martsolf syndrome. Hum. Mutat. *34*, 686–696.

75. Artegiani, B., Lange, C., and Calegari, F. (2012). Expansion of embryonic and adult neural stem cells by in utero electroporation or viral stereotaxic injection. J. Vis. Exp. *68*, e4093.

76. Bian, S., Repic, M., Guo, Z., Kavirayani, A., Burkard, T., Bagley, J.A., Krauditsch, C., and Knoblich, J.A. (2018). Genetically engineered cerebral organoids model brain tumor formation. Nat. Methods *15*, 631–639.

77. Alcantara Llaguno, S., Chen, J., Kwon, C.H., Jackson, E.L., Li, Y., Burns, D.K., Alvarez-Buylla, A., and Parada, L.F. (2009). Malignant astrocytomas originate from neural stem/progenitor cells in a somatic tumor suppressor mouse model. Cancer Cell *15*, 45–56.

78. Vassilev, L.T., Vu, B.T., Graves, B., Carvajal, D., Podlaski, F., Filipovic, Z., Kong, N., Kammlott, U., Lukacs, C., Klein, C., et al. (2004). In vivo activation of the p53 pathway by small-molecule antagonists of MDM2. Science *303*, 844–848.

79. Falchook, G.S., Lewis, K.D., Infante, J.R., Gordon, M.S., Vogelzang, N.J., DeMarini, D.J., Sun, P., Moy, C., Szabo, S.A., Roadcap, L.T., et al. (2012). Activity of the oral MEK inhibitor trametinib in patients with advanced melanoma: a phase 1 dose-escalation trial. Lancet Oncol. *13*, 782–789.

80. Kelley, K.W., and Paşca, S.P. (2022). Human brain organogenesis: toward a cellular understanding of development and disease. Cell *185*, 42–61.

81. Trevino, A.E., Sinnott-Armstrong, N., Andersen, J., Yoon, S.J., Huber, N., Pritchard, J.K., Chang, H.Y., Greenleaf, W.J., and Paşca, S.P. (2020). Chromatin accessibility dynamics in a model of human forebrain development. Science *367*.

82. Fleck, J.S., Jansen, S.M.J., Wollny, D., Zenk, F., Seimiya, M., Jain, A., Okamoto, R., Santel, M., He, Z., Camp, J.G., et al. (2023). Inferring and perturbing cell fate regulomes in human brain organoids. Nature *621*, 365–372.

83. Yoon, S.J., Elahi, L.S., Paşca, A.M., Marton, R.M., Gordon, A., Revah, O., Miura, Y., Walczak, E.M., Holdgate, G.M., Fan, H.C., et al. (2019). Reliability of human cortical organoid generation. Nat. Methods *16*, 75–78.

84. Velasco, S., Kedaigle, A.J., Simmons, S.K., Nash, A., Rocha, M., Quadrato, G., Paulsen, B., Nguyen, L., Adiconis, X., Regev, A., et al. (2019). Individual brain organoids reproducibly form cell diversity of the human cerebral cortex. Nature *570*, 523–527.

85. Kanton, S., Boyle, M.J., He, Z., Santel, M., Weigert, A., Sanchís-Calleja, F., Guijarro, P., Sidow, L., Fleck, J.S., Han, D., et al. (2019). Organoid single-cell genomic atlas uncovers human-specific features of brain development. Nature *574*, 418–422.

86. Benito-Kwiecinski, S., Giandomenico, S.L., Sutcliffe, M., Riis, E.S., Freire-Pritchett, P., Kelava, I., Wunderlich, S., Martin, U., Wray, G.A., McDole, K., et al. (2021). An early cell shape transition drives evolutionary expansion of the human forebrain. Cell *184*, 2084–2102.e19.

87. Trujillo, C.A., Rice, E.S., Schaefer, N.K., Chaim, I.A., Wheeler, E.C., Madrigal, A.A., Buchanan, J., Preissl, S., Wang, A., Negraes, P.D., et al. (2021). Reintroduction of the archaic variant of *NOVA1* in cortical organoids alters neurodevelopment. Science *371*, eaax2537.

88. Li, C., Fleck, J.S., Martins-Costa, C., Burkard, T.R., Themann, J., Stuempflen, M., Peer, A.M., Vertesy, Á., Littleboy, J.B., Esk, C., et al. (2023). Single-cell brain organoid screening identifies developmental defects in autism. Nature *621*, 373–380.

89. Meng, X., Yao, D., Imaizumi, K., Chen, X., Kelley, K.W., Reis, N., Thete, M.V., Arjun McKinney, A., Kulkarni, S., Panagiotakos, G., et al. (2023). Assembloid CRISPR screens reveal impact of disease genes in human neurodevelopment. Nature *622*, 359–366.

90. Bowles, K.R., Silva, M.C., Whitney, K., Bertucci, T., Berlind, J.E., Lai, J.D., Garza, J.C., Boles, N.C., Mahali, S., Strang, K.H., et al. (2021). ELAVL4, splicing, and glutamatergic dysfunction precede neuron loss in MAPT mutation cerebral organoids. Cell *184*, 4547–4563.e17.

91. Koch, C., Massimini, M., Boly, M., and Tononi, G. (2016). Neural correlates of consciousness: progress and problems. Nat. Rev. Neurosci. *17*, 307–321.

92. Farahany, N.A., Greely, H.T., Hyman, S., Koch, C., Grady, C., Pașca, S.P., Sestan, N., Arlotta, P., Bernat, J.L., Ting, J., et al. (2018). The ethics of experimenting with human brain tissue. Nature *556*, 429–432.

93. Mansour, A.A., Gonçalves, J.T., Bloyd, C.W., Li, H., Fernandes, S., Quang, D., Johnston, S., Parylak, S.L., Jin, X., and Gage, F.H. (2018). An in vivo model of functional and vascularized human brain organoids. Nat. Biotechnol. *36*, 432–441.

94. Revah, O., Gore, F., Kelley, K.W., Andersen, J., Sakai, N., Chen, X., Li, M.Y., Birey, F., Yang, X., Saw, N.L., et al. (2022). Maturation and circuit integration of transplanted human cortical organoids. Nature *610*, 319–326.

95. Schafer, S.T., Mansour, A.A., Schlachetzki, J.C.M., Pena, M., Ghassemzadeh, S., Mitchell, L., Mar, A., Quang, D., Stumpf, S., Ortiz, I.S., et al. (2023). An in vivo neuroimmune organoid model to study human microglia phenotypes. Cell *186*, 2111–2126.e20.

96. Love, M.I., Huber, W., and Anders, S. (2014). Moderated estimation of fold change and dispersion for RNA-seq data with DESeq2. Genome Biol. *15*, 550.

97. Newman, A.M., Steen, C.B., Liu, C.L., Gentles, A.J., Chaudhuri, A.A., Scherer, F., Khodadoust, M.S., Esfahani, M.S., Luca, B.A., Steiner, D., et al. (2019). Determining cell type abundance and expression from bulk tissues with digital cytometry. Nat. Biotechnol. *37*, 773–782.

98. Fleck, J.S., Sanchís-Calleja, F., He, Z., Santel, M., Boyle, M.J., Camp, J.G., and Treutlein, B. (2021). Resolving organoid brain region identities by mapping single-cell genomic data to reference atlases. Cell Stem Cell *28*, 1148–1159.e8.

99. Hao, Y., Hao, S., Andersen-Nissen, E., Mauck, W.M., Zheng, S., Butler, A., Lee, M.J., Wilk, A.J., Darby, C., Zager, M., et al. (2021). Integrated analysis of multimodal single-cell data. Cell *184*, 3573–3587.e29.

100. Artegiani, B., van Voorthuijsen, L., Lindeboom, R.G.H., Seinstra, D., Heo, I., Tapia, P., López-Iglesias, C., Postrach, D., Dayton, T., Oka, R., et al. (2019). Probing the tumor suppressor function of BAP1 in CRISPR-engineered human liver organoids. Cell Stem Cell *24*, 927–943.e6.

101. Ran, F.A., Hsu, P.D., Wright, J., Agarwala, V., Scott, D.A., and Zhang, F. (2013). Genome engineering using the CRISPR-Cas9 system. Nat. Protoc. *8*, 2281–2308.

102. Birey, F., Andersen, J., Makinson, C.D., Islam, S., Wei, W., Huber, N., Fan, H.C., Metzler, K.R.C., Panagiotakos, G., Thom, N., et al. (2017). Assembly of functionally integrated human forebrain spheroids. Nature *545*, 54–59.

103. Birey, F., Li, M.Y., Gordon, A., Thete, M.V., Valencia, A.M., Revah, O., Paşca, A.M., Geschwind, D.H., and Paşca, S.P. (2022). Dissecting the molecular basis of human interneuron migration in forebrain assembloids from Timothy syndrome. Cell Stem Cell *29*, 248–264.e7.

104. Pagliaro, A., Finger, R., Zoutendijk, I., Bunschuh, S., Clevers, H., Hendriks, D., and Artegiani, B. (2023). Temporal morphogen gradient-driven neural induction shapes single expanded neuroepithelium brain organoids with enhanced cortical identity. Nat. Commun. *14*, 7361.

105. Faas, F.G., Avramut, M.C., van den Berg, B.M., Mommaas, A.M., Koster, A.J., and Ravelli, R.B. (2012). Virtual nanoscopy: generation of ultra-large high resolution electron microscopy maps. J. Cell Biol. *198*, 457–469.

106. Stuart, T., Butler, A., Hoffman, P., Hafemeister, C., Papalexi, E., Mauck, W.M., Hao, Y., Stoeckius, M., Smibert, P., and Satija, R. (2019). Comprehensive integration of single-cell data. Cell *177*, 1888–1902.e21.

107. Bhaduri, A., Andrews, M.G., Mancia Leon, W., Jung, D., Shin, D., Allen, D., Jung, D., Schmunk, G., Haeussler, M., Salma, J., et al. (2020). Cell stress in cortical organoids impairs molecular subtype specification. Nature *578*, 142–148.

STAR★METHODS

KEY RESOURCES TABLE

REAGENT or RESOURCE	SOURCE	IDENTIFIER
Antibodies		
anti-BRN2	Santa Cruz	sc-393324 (RRID:AB_2737347)
anti-CTIP2	Abcam	ab18465 (RRID:AB_2064130)
anti-CUX1	Santa Cruz	sc-514008 (RRID:AB_2715519)
anti-DCX	Millipore	AB2253 (RRID:AB_1586992)
anti-DLX2	Santa Cruz	sc-393879
anti-EMX2	Abcam	ab94713 (RRID:AB_10863896)
anti-GAD65	R and D systems	AF2247 (RRID:AB_2108039)
anti-GAD67	Millipore	MAB5406 (RRID:AB_2278725)
anti-GFAP	Santa Cruz	sc33673 (RRID:AB_627673)
anti-GFP	Abcam	ab13970 (RRID:AB_300798)
anti-HB9	Santa Cruz	sc-515769
anti-HOPX	Santa Cruz	sc-398703 (RRID:AB_2687966)
anti-Ki-67	Thermo Fisher Scientific	14-5698-82 (RRID:AB_10854564)
anti-MAP2	Covance	PCK-554P (RRID:AB_291541)
anti-N-CAD	Santa Cruz	sc-59987 (RRID:AB_781744)
anti-NKX2-1	Abcam	ab76013 (RRID:AB_1310784)
anti-NKX2-2	Santa Cruz	sc-15015 (RRID:AB_650277)
anti-OLIG2	Sigma-Aldrich	AB9610 (RRID:AB_570666)
anti-PAX6	Covance	PRB-278P (RRID:AB_291612)
anti-RORB	Atlas Antibodies	HPA008393 (RRID:AB_1079830)
anti-S100B	Abcam	ab41548 (RRID:AB_956280)
anti-SATB2	Abcam	ab51502 (RRID:AB_882455)
anti-SOX2	Millipore	AB5603 (RRID:AB_2286686)
anti-SOX2	Thermo Fisher Scientific	14-9811-82 (RRID:AB_11219471)
anti-SOX5	Abcam	ab94396 (RRID:AB_10859923)
anti-TBR1	Abcam	ab31940 (RRID:AB_2200219)
anti-TBR2	Abcam	ab23345 (RRID:AB_778267)
anti-TUJ1	BioLegend	801202 (RRID:AB_2728521)
Alexa Fluor 488 goat anti-chicken	Thermo Fisher Scientific	A-11039 (RRID:AB_2534096)
Alexa Fluor 488 donkey anti-goat	Thermo Fisher Scientific	A-11055 (RRID:AB_2534102)
Alexa Fluor 488 goat anti-guinea pig	Thermo Fisher Scientific	A-11073 (RRID:AB_2534117)
Alexa Fluor 488 donkey anti-rabbit	Thermo Fisher Scientific	A-21206 (RRID:AB_2535792)
Alexa Fluor 568 donkey anti-mouse	Thermo Fisher Scientific	A-10037 (RRID:AB_2534013)
Alexa Fluor 568 donkey anti-goat	Thermo Fisher Scientific	A-11057 (RRID:AB_2534104)
Alexa Fluor 568 goat anti-guinea pig	Thermo Fisher Scientific	A-11075 (RRID:AB_2534119)
Alexa Fluor 647 donkey anti-rabbit	Thermo Fisher Scientific	A-31573 (RRID:AB_2536183)
Alexa Fluor 647 goat anti-rat	Thermo Fisher Scientific	A-21247 (RRID:AB_141778)
Biological Samples		
Human fetal central nervous system tissues (GW8, GW12-GW15)	Leiden University Medical Center and Human Developmental Biology Resource	N/A
Chemicals, peptides, and recombinant proteins		
Advanced DMEM/F12	Thermo Fisher Scientific	12634010
Penicillin-Streptomycin	Thermo Fisher Scientific	15140122

(*Continued on next page*)

Continued

REAGENT or RESOURCE	SOURCE	IDENTIFIER
GlutaMAX	Thermo Fisher Scientific	35050061
HEPES	Thermo Fisher Scientific	15630080
Neurobasal medium	Thermo Fisher Scientific	21103049
B-27 supplement, minus vitamin A	Thermo Fisher Scientific	12587010
B-27 supplement	Thermo Fisher Scientific	17504044
N-2 supplement	Thermo Fisher Scientific	17502048
MEM non-essential amino acid solution	Thermo Fisher Scientific	11140050
Human EGF	Peprotech	AF-100-15
Human FGF-2	Peprotech	100-18B
Human FGF-10	Peprotech	100-26
Human BMP-4	Peprotech	120-05ET
CHIR-99021	Sigma-Aldrich	SML1046
Primocin	Invivogen	ant-pm-2
Cultrex Basement Membrane Extract (BME), Growth Factor Reduced, Type 2	R and D systems	3533-010-02
Corning Matrigel hESC-Qualified Matrix	Corning	354277
mTeSR Plus Medium	STEMCELL Technologies	100-0276
Y-27632 dihydrochloride	AbMole	M1817
DMEM/F12	Thermo Fisher Scientific	11330032
KnockOut Serum Replacement	Thermo Fisher Scientific	10828028
2-mercaptoethanol	Thermo Fisher Scientific	21985023
Dorsomorphin	STEMCELL Technologies	72102
SB-431542	STEMCELL Technologies	72232
Neurobasal-A medium	Thermo Fisher Scientific	10888-022
Human BDNF	Peprotech	450-02
Human NT-3	Peprotech	450-03
Corning Matrigel Basement Membrane Matrix	Corning	354234
Gentle Cell Dissociation Reagent	STEMCELL Technologies	100-0485
Anti-Adherence Rinsing Solution	STEMCELL Technologies	07010
Opti-MEM, no Phenol Red	Thermo Fisher Scientific	11058021
DNAse I	Roche	10104159001
TRIzol Reagent	Thermo Fisher Scientific	15596026
DAPI	Thermo Fisher Scientific	62248
4-Methylumbelliferone	Sigma-Aldrich	M1381
BTT-3033	Tocris	4724
Chondroitinase ABC from *Proteus vulgaris*	Sigma-Aldrich	C3667
Nutlin-3a	MedChemExpress	HY-50696
Afatinib	Selleckchem	S1011
Everolimus	Selleckchem	S1120
Trametinib	Selleckchem	S2673
Critical commercial ssays		
Fluo-4 Calcium Imaging Kit	Thermo Fisher Scientific	F10489
CellTiter-Glo 3D Cell Viability Assay	Promega	G9681
STEMdiff Cerebral Organoid Kit	STEMCELL Technologies	08570
Neural Tissue Dissociation Kit (P)	Miltenyi	130-092-628
Dead Cell Removal Kit	Miltenyi	130-090-101
SuperScript IV First-Strand Synthesis System	Thermo Fisher Scientific	8091050
iQ SYBR Green Supermix	Bio-Rad	1708886

(*Continued on next page*)

Continued

REAGENT or RESOURCE	SOURCE	IDENTIFIER
Deposited data		
Read-level bulk and single-cell RNA sequencing data generated in this study	This study	GEO: GSE248481
Raw bulk and single-cell RNA sequencing data generated in this study	This study	EGA: EGAC00001001864
Proteomics data generated in this study	This study	PRIDE: PXD047075
Previously published single-cell RNA sequencing data on human fetal brain	Bhaduri et al.[37]	NeMO Archive (RRID: SCR_002001) and at https://data.nemoarchive.org/biccn/grant/u01_devhu/kriegstein/transcriptome/scell/10x_v2/human/processed/counts/
Previously published single-cell RNA sequencing data on human fetal brain	Yu et al.[42]	GEO: GSE165388
Previously published single-cell RNA sequencing data on human fetal brain	Fan et al.[52]	GEO: GSE120046
Experimental models: Cell lines		
Human H1 hESC line	WiCell	WA01
Oligonucleotides		
qPCR primers, sgRNA cloning primers, and genotyping primers	See Table S4	N/A
Software and algorithms		
RStudio 2022.02.2	RStudio, PBC	https://www.rstudio.com/
DESeq2 1.36.0	Love et al.[96]	https://bioconductor.org/packages/release/bioc/html/DESeq2.html
CIBERSORTx	Newman et al.[97]	https://cibersortx.stanford.edu/
VoxHunt	Fleck et al.[98]	https://github.com/quadbio/VoxHunt
Cell Ranger 5.0.1	10X genomics	https://www.10xgenomics.com/support/software/cell-ranger
Seurat 4.0	Hao et al.[99]	https://satijalab.org/seurat/
Maxquant 1.6.10.0	Max Planck Institute of Biochemistry	https://www.maxquant.org/
Perseus 1.6.10.0	Max Planck Institute of Biochemistry	https://maxquant.net/perseus/
Uniprot human database (Organism Species 9606)	Uniprot	https://www.uniprot.org/
Las X 3.5.7	Leica	N/A
Fiji 2.14.0	ImageJ	https://imagej.net/
Prism 9.4.1	GraphPad	https://www.graphpad.com/
Adobe Illustrator 28.0 and Photoshop 25.1.0	Adobe Inc.	https://www.adobe.com/

RESOURCE AVAILABILITY

Lead contact

Further information and requests for reagents and resources should be directed to and will be fulfilled by the lead contact, Benedetta Artegiani (b.a.artegiani@prinsesmaximacentrum.nl).

Materials availability

This study did not generate new unique reagents.

Data and code availability

Read-level bulk and single-cell RNA sequencing data of this study have been deposited in GEO (GSE248481) and are publicly available as of the date of publication. Due to donor privacy concerns, associated raw sequencing data can be made available for replication purposes by the Data Access Committee of the Princess Máxima Center (EGAC00001001864). The mass spectrometry proteomics data of this study have been deposited to the ProteomeXchange Consortium via the PRIDE partner repository (PXD047075) and are publicly available as of the date of publication. Single-cell RNA sequencing data from previous publications that were used in this study can be found in GEO (GSE165388 and GSE120046), and in the NeMO Archive (RRID: SCR_002001) and at https://data.

nemoarchive.org/biccn/grant/u01_devhu/kriegstein/transcriptome/scell/10x_v2/human/processed/counts/. This paper does not report original code. Any additional information required to reanalyze the data reported in this paper is available from the lead contact upon request.

EXPERIMENTAL MODEL AND STUDY PARTICIPANT DETAILS

Human tissue

Human fetal central nervous system (brain and spinal cord) tissues were obtained from elective abortions from Leiden University Medical Center or the Human Developmental Biology Resource, under informed consent and ethical approval. Ethical approval for the use of human fetal tissue was provided by the Commission of Medical Ethics of Leiden University Medical Center (Leiden, NL), Human Developmental Biology Resource (HDBR, Cambridge and Newcastle, UK), and the Biobank and Data Access Committee of Princess Máxima Center (Utrecht, NL). In total, n = 8 tissues were used in this study. Tissues were from both sexes (3 male, 2 female, and 3 not determined) and ranged in developmental stage from GW12 to GW15 (brain) and GW8 (spinal cord).

Human embryonic stem cells

The hESC H1 line (WA01, male) was maintained on hESC Qualified Matrigel-coated plates in mTeSR Plus medium in a 37°C, 5% CO_2 incubator. The hESCs were maintained below passage 50. The hESCs were used in accordance with the local ethical regulations and the hESC line was authenticated through STR profiling.

METHOD DETAILS

Tissue isolation, dissection, and processing for organoid culture

Human fetal tissues were derived from healthy abortion material from anonymous donors, under informed consent and ethical approval (Commission of Medical Ethics, Leiden University Medical Center, Leiden) or human embryonic and fetal material was provided by the Joint MRC / Wellcome Trust (Grant #MR/006237/1) Human Developmental Biology Resource (HDBR) (http://www.hdbr.org), under informed consent and ethical approval (HDBR, UK and Biobank and Data Access Committee (BDAC), Princess Máxima Center, Utrecht, NL). Fully anonymous subjects donated the tissue voluntarily and upon informed consent and were informed that the material would be used for research purposes only. Tissue donation did not entitle for any financial, medical or personal benefit. Donors/tissue providers were informed that the research included the understanding of how organs normally develop and relative diseases in which normal development is affected, including the possibility to grow cells derived from the donated material. Material and organoids were treated accordingly to standard laboratory practice, including, but not limited, to their disposal. Tissues from eight different donors were used in this study, ranging between GW12-15 for brain tissues, and GW8 for spinal cord. Recognizable tissue pieces were collected and washed in 0.9% (wt/vol) NaCl and kept on ice. Within 24 hrs, the tissue was extensively washed with cold Advanced DMEM/F12 containing 10 U/ml Penicillin-Streptomycin. Evident necrotic areas were removed using micro-dissecting scissors. Single pieces were isolated and individually transferred into a well of a 12-well plate. Each piece was further processed and cut into smaller pieces (approximately 1 mm diameter), while avoiding extensive mincing of the tissue. A few of these small pieces were collected for RNA isolation and subsequent qPCR analysis using a panel of marker genes to assign tissue identity (dorsal and ventral forebrain identity). Some pieces were collected for fixation in 4% formaldehyde to use for further immunofluorescence analysis. The rest of these pieces were used for establishment of the organoid lines.

FeBO establishment and long-term culturing

Tissue pieces obtained from the dissection procedure were seeded in 12-well plates (about 10-15 pieces/well). The optimized culture medium contained a base medium of a 1:1 mixture of Advanced DMEM/F12 supplemented with 10 U/ml Penicillin-Streptomycin, 1X GlutaMax, and 1X HEPES (Advanced DMEM +++) and Neurobasal medium plus 10 U/ml Penicillin-Streptomycin. To this base medium, 1X B27 Supplement minus vitamin A, 1X N2 Supplement, 1X MEM non-essential amino acid solution, 50 ng/ml hFGF-10, 40 ng/ml hFGF-2, 50 ng/ml hEGF, and 100 μg/ml Primocin were added to constitute the expansion medium. The organoids were cultured at 37°C and 5% CO_2 under constant rotation (60 rpm) using an orbital shaker. Ca. 5 days after seeding the pieces of tissue, formation of organoid-like structures with defined borders was observed. These structures were transferred to a new well of a 12-well plate using a blunt-cut P1000 pipette tip and were allowed to further grow until they reached a size of approximately 2-3 mm in diameter. These initial organoids were split by cutting them into smaller pieces using micro-dissecting scissors, washed with Advanced DMEM +++ (from now on referred to as wash buffer) and 2-3 pieces were transferred into a new well of a 12-well plate, and typically within 3-5 days new organoids were formed again. Over time, the organoids acquired a more regular, round morphology, sometimes with folded edges. Regular splitting of the organoids was performed approximately every 2-3 weeks for ca. the first 6 months, and thereafter every 3-4 weeks. The expansion medium was refreshed every 3-4 days. For further maturation, single organoids at any given point during the culturing period were transferred to a well of a 24-well plate and the expansion medium was completely removed by rinsing once with wash buffer. Maturation medium was prepared by using the base medium supplemented with 1X N2 supplement, 1X MEM non-essential amino acid solution, 100 μg/ml Primocin, 1X B27 Supplement (containing vitamin A), 100 μg/ml Primocin, and 0.5% basement membrane extract (BME). We initially also tested addition of 20 ng/ml hBDNF, 20 ng/ml hGDNF, but omitted these factors in later experiments. Maturation medium was changed every second day and kept from 3 to 10 days depending on the downstream application. Cultures were monthly tested for mycoplasma and tested negative without exception.

FeBOs growth assessment

The growth of the organoids was measured by two independent means: increase of surface area of single organoids in between passages; and for overall tissue expansion by considering the increase of volume/passage and the split ratio. After splitting, composite pictures of multiple organoids were taken at regular intervals using a Leica DMi8 microscope. The images were analyzed and surface areas were calculated using Fiji (2.14.0, ImageJ) software, and volumes were calculated by measuring the diameter and using the formula $4\pi r_1 r_2 r_3/3$. The average increased volume across multiple organoids in between a split was then multiplied per the split ratio over time to estimate the produced biomass.

Organoid and brain tissue processing for immunofluorescence

For immunofluorescence analysis, organoids or human fetal brain tissue were processed in the same way. They were fixed by incubation with 4% formaldehyde over night at 4°C. Samples were then washed 2-3 times with 1X PBS and kept at 4°C before further processing. Samples were embedded in 3% low melting agarose and sliced using a Vibratome to obtain 40 μm sections. Those were preserved in 1X PBS at 4°C or in freezing medium (50% 2X PBS, 25% Ethylene Glycol and 25% Glycerol) at -20°C for long-term storage. Staining was performed on floating sections by an initial permeabilization and blocking incubation step of 2 hrs at room temperature in blocking buffer (1X PBS, 5% BSA, 0.02% Triton X-100), and a 48 hrs primary antibody incubation at 4°C with the appropriate primary antibody at the indicated dilutions (Table S4) in incubation buffer (1X PBS, 2% BSA). Sections were washed 3 times with 1X PBS and incubated for 24 hrs at 4°C with appropriate secondary antibodies (Table S4) diluted 1:1000 in incubation buffer. Sections were then incubated with DAPI (1 μg/ml) diluted in 1X PBS for 20 min at room temperature to counterstain the nuclei. Sections were washed 3 times with 1X PBS and transferred to a 24-well glass-bottom SensoPlate using a thin brush and mounted using Immu-Mount mounting medium and a glass coverslip for further imaging.

Lentiviral infection of FeBOs

Lentiviruses were previously produced,[100] using the pLV-H2B-mCherry-ires-Puro construct. FeBOs were infected with lentiviruses for 12 hrs in a 24-well plate. After incubation, virus-containing medium was removed and organoids were washed 3 times with wash buffer and then cultured in expansion medium. Infected FeBOs were collected at different time points post infection and processed for immunofluorescence staining as described above.

ECM perturbations in FeBOs

Passaged FeBOs were individually cultured and upon organoid reformation, the FeBOs were exposed to different ECM perturbing molecules in expansion medium: BTT-3033 (1 μM), chondroitinase ABC from *Proteus vulgaris* (50 mU/ml), or 4-methylumbelliferone (200 μM) for 7 days with regular medium changes. Brightfield images were acquired before, during, and after treatment to assess organoid sizes and growth. Organoids were collected and processed for immunofluorescence staining as described above.

Morphogen treatment on FeBOs and PSC-derived 3D brain models

The effect of BMP and Wnt was tested on both dorsal and ventral forebrain FeBOs, as well as on PSC-derived cortical spheroids and PSC-derived unguided cerebral organoids (see below). For FeBOs, hBMP4 (40 ng/ml) and CHIR-99021 (3 μM), referred to as BMP+Wnt, were added to the expansion medium of individually-cultured FeBOs for 7 days. Then, dorsal and ventral forebrain FeBOs (control and BMP+Wnt-treated) were collected for RNA analysis. For both PSC-brain models, we added BMP+Wnt at a similar point of their developmental trajectory, *i.e.* after the neural induction phase and during the expansion phase. For PSC-derived cortical spheroids, BMP+Wnt were added and kept from day 17 onwards. On day 24, each spheroid was collected for RNA analysis. For PSC-derived unguided cerebral organoids, BMP+Wnt were added and kept from day 7 onwards. On day 15, each organoid was collected for RNA analysis as described below.

Sparse cell labeling of FeBOs

To visualize cell morphology, electroporation with the *piggyBac* transposase plasmid and the donor PBCAG-EGFP plasmid (Addgene #40973) or PBCAG-mRFP plasmid (Addgene #40996) was performed to label sparse cells within FeBOs (see below). One week after electroporation, organoids were transferred to maturation medium. Live whole organoids (10 days after switching to maturation medium), were imaged at a confocal microscope as described below.

Measurement of calcium flux by live imaging

Live FeBOs (early or late passage) cultured in 5 days of maturation medium were embedded in 3% low melting temperature agarose and sliced to 100 μm-thick sections using a Vibratome. These samples were then processed using the Fluo-4 Calcium Imaging Kit, according to the manufacturer's instructions with a few modifications. Briefly, slices were incubated for 15 min at 37°C followed by 15 min at room temperature with the calcium probe in complete medium diluted 1:2 with 1X PBS and supplemented with 20 mM glucose. Slices were then washed once and maintained in medium supplemented with Neuro Backdrop Background Suppressor solution (dilution 1:10) and immediately imaged on a confocal Sp8 microscope (Leica). For any defined position, images were acquired every 0.8 or 2 seconds for a total of 5 min in the 488 channel. Images over time were sequentially assembled to create movies with ImageJ software. To record calcium spikes, single cells were carefully outlined in a region of interest (ROI), and intensity of fluorescence was measured over the entire time series. The ΔF1/F0 trace for each ROI was calculated by dividing the fluorescence by the initial baseline fluorescence for each time point, and traces were visualized in GraphPad Prism (9.4.1).

CRISPR-editing, brain tumor modelling, and drug screening in FeBOs

Plasmids carrying a specific sgRNA were generated by cloning the sgRNA sequences for the different targets in the pSPgRNA plasmid (Addgene #47108), as described previously.[101] Previously used sgRNAs targeting TP53, PTEN, or NF1[100] were used while for targeting of RAB3GAP2 sgRNAs were designed using an online web-tool (www.atum.bio/eCommerce/cas9/input). The sgRNA cloning primers are provided in Table S4. A plasmid encoding both SpCas9 as well as mCherry for visualization of transfected cells (Addgene #66940) was co-transfected together with the sgRNA plasmid(s). To be able to permanently fluorescently label the transfected cells, we used a two-plasmid transposon system (*piggyBac* transposase plasmid and a donor plasmid with terminal repeats bearing a cassette with PBCAG-EGFP (Addgene #40973)) and co-transfected those with the sgRNA and the SpCas9-mCherry plasmids. Electroporation was performed as follows: FeBOs were cut into pieces of approximately 1 mm of diameter and were washed once with Opti-MEM without Phenol Red. The pieces were incubated for 5-10 min in 200 μl of Opti-MEM containing 100 μg of the DNA mixture (9 μg *piggyBac* plasmid, 26 μg transposable CAG-EGFP plasmid, 10 μg per sgRNA plasmid, 35 μg mCherry-Cas9 plasmid). Two to three organoid pieces were transferred in a 2 mm gap cuvette and electroporated with a NEPA21 electroporator using the following parameters: Poring pulse: Voltage = 175V, Pulse Length = 7.5, Pulse Interval = 50 msec, Number of Pulses = 2; Transfer pulse: Voltage = 20V, Pulse Length = 50 msec, Pulse Interval = 50 msec, Number of Pulses = 5. Immediately after electroporation, 1 ml of expansion medium was added to the cuvette to recover the organoid pieces for 15 min, after which they were transferred back into a well of a 12-well plate (1 piece/well), washed once with wash buffer and were let to reform into organoids in expansion medium. Genetically-engineered FeBOs were cultured as described for wild-type organoids with regular splitting. For TP53-mutant FeBOs or TP53; NF1; PTEN (TPN)-mutant FeBOs, when the transfected (mutated) population overgrew the non-transfected population (over repeated splitting events), as assessed by the increase in GFP$^+$ fluorescence, part of the transfected organoids was cut and processed for DNA isolation using a lysis buffer (0.1M Tris-HCl (pH 8.5–9.0), 0.2 M NaCl, 5 mM EDTA and 0.2% SDS in sterile dH$_2$O). Genomic DNA was then isolated by isopropanol precipitation. The DNA was genotyped for the respective mutation(s) by Sanger sequencing (Table S4). If necessary, genotypes were deconvoluted using the ICE v2 CRISPR tool. Defined mutant FeBOs were further passaged and grown in expansion medium as syngeneic lines. When appropriate, the mutant organoids were transferred to maturation medium. To perform drug screening in wild-type, TP53-mutant or TPN-mutant FeBOs, organoids were cut into similarly sized, small organoid fragments (smaller than what is routinely done for passaging FeBO lines) and individually placed in a well of a 24-well plate. Then, after organoid reformation (ca. 4 days later), the FeBOs were exposed to increasing concentrations of the different drugs used added to expansion medium: Nutlin-3a (0-20 μM), afatinib (0-50 μM), everolimus (0-50 μM), trametinib (0-50 μM). At the start of the drug treatment and after 5 days of drug exposure, GFP fluorescence images were acquired to monitor drug effects. Then, ATP-based assays (CellTiter-Glo 3D Cell Viability Assay) were performed to assess organoid viability and the percentage of viability over control (vehicle)-treated FeBOs was calculated across multiple organoids per condition.

Generation of PSC-derived 3D brain models

Human embryonic stem cells (hESCs) were used in accordance with the local and institutional ethical regulations. Feeder-free human H1 hESCs were cultured on 6-well plates coated with hESC Qualified Matrigel at 37°C and 5% CO$_2$ in mTeSR Plus Medium. Culture medium was changed every other day and cells were passaged using Gentle Cell Dissociation Reagent every week, following the manufacturer's protocol. Prior to passaging, cells were checked for regions of differentiation, and, if present, these were carefully scraped off with a pipette tip. The hESCs used throughout the study were maintained below passage 50. PSC-cortical spheroids were generated as previously described,[60,102,103] with minor modifications.[104] Briefly, confluent hESCs were first detached from Matrigel-coated plates using Gentle Dissociation Reagent and mechanically dissociated into single cells. To generate PSC-cortical spheroids, 9000 cells resuspended in 100 μl of mTeSR medium containing 10 μM Y-27632 were plated in each well of a 96-well ultra-low-attachment U-bottom plate. Medium was replaced on day 2 to the neural induction medium containing 1:1 DMEM/F12, 20% knockout serum replacement, 1X non-essential amino acids, 1X GlutaMax, 1X 2-mercaptoethanol, and supplemented with 5 μM Dorsomorphin and 10 μM SB-431542. Medium was fully refreshed on day 4 and 5. On day 6, medium was changed to the expansion medium containing Neurobasal-A medium, 1X Penicillin and Streptomycin, 1X B27 supplement without vitamin A, 1X GlutaMax, supplemented with 20 ng/ml hEGF and 20 ng/ml hFGF-2. On day 7, organoids were moved to a 24-well plate previously treated with Anti-Adherence Rinsing Solution with one organoid per well. Expansion medium was refreshed every other day, till day 24. On day 25, medium was changed to maturation medium containing Neurobasal-A medium, 1X Penicillin and Streptomycin, 1X B27 supplement (containing vitamin A), 1X GlutaMax and supplemented with 20 ng/ml hBDNF and 20 ng/ml hNT-3. At this stage, medium was refreshed every other day. PSC-unguided cerebral organoids were generated using the STEMdiff Cerebral Organoid Kit[59] with minor modifications.[104] Briefly, confluent hESCs were mechanically dissociated into single cells after detaching them from Matrigel-coated plates using Gentle Cell Dissociation Reagent. Then, 9000 cells were plated per well in a 96-well ultra-low-attachment U-bottom plate in EB Seeding Medium, containing 10 μM Y-27632. On days 2 and 4, 100 μl of EB Formation Medium were added to each well. On day 5, medium was fully changed to the Induction Medium. On day 7, each organoid was embedded in a 14 μl droplet of Matrigel, using an Organoid Embedding Sheet. Matrigel droplets containing organoids were left to polymerize at 37°C for 30 minutes. Around 12 to 16 embedded organoids were placed in a well of a 6-well plate, pre-treated with Anti-Adherence Rinsing Solution, in Expansion Medium. After 3 days of culture, on day 10, medium was changed to Maturation Medium, and plates were placed on orbital shaker. At this stage, medium changes were performed every 3 to 4 days, according to the STEMdiff Cerebral Organoid Kit protocol. Cultures were monthly tested for mycoplasma and tested negative without exception.

Brain tumor modelling and drug screening in PSC-derived brain organoids

On day 7 of PSC-cerebral organoid formation, prior to Matrigel embedding, the organoids were electroporated with the same plasmids described above for FeBOs to introduce concomitant TP53, NF1, and PTEN mutations, as well as to visualize transfected cells by integration of PBCAG-EGFP by *piggyBac*. Electroporation was performed as follows. Organoids were washed once with Opti-MEM without Phenol Red (Thermo Fisher) and incubated for 5-10 min in 200 μl of Opti-MEM containing 22 μg of the DNA mixture (2 μg *piggyBac* plasmid, 5 μg transposable PBCAG-EGFP plasmid, 3 μg for each sgRNA plasmid, 6 μg mCherry-Cas9 plasmid). The organoids were transferred into a 2 mm gap cuvette and electroporated with a NEPA21 electroporator using the following parameters: Poring pulse: Voltage = 75V, Pulse Length = 5, Pulse Interval = 50 msec, Number of Pulses = 2; Transfer pulse: Voltage = 20V, Pulse Length = 50 msec, Pulse Interval = 50 msec, Number of Pulses = 5. Immediately after electroporation, 1 ml of medium was added to the cuvette to recover the organoids for 15 min, after which they were transferred back into a well of a 6-well plate (10 organoids/well), washed once with wash buffer and let to recover. Organoids were thereafter cultured according to the standard protocol as described above, except that organoid embedding was performed on day 10. Organoids displaying GFP^+ transfected cells (ca. 80% of the electroporated population) were kept for further analysis. GFP fluorescence and brightfield images were temporally acquired and GFP fluorescence area occupancy within each organoid as well the GFP^+ area sizes were calculated at various time points post electroporation. To probe the response of selected organoids with defined GFP areas, we exposed individual organoids to 10 μM Nutlin-3a and monitored their response over a 30-day time window. GFP fluorescence and brightfield images were temporally acquired to calculate changes in the GFP fluorescence in response to Nutlin-3a.

Confocal imaging, analysis, and quantification

Stained organoids and brain tissue slices were imaged with a 20X objective on a Sp8 confocal microscope (Las X software, Leica). Lif files of the merged images were processed and analyzed for measurement of mean fluorescence intensity and manual counting of positive cells for any given markers, using Fiji (2.14.0, ImageJ) software and Photoshop CS4 (Adobe). For quantification of cell distribution, regions of interest (ROIs) were defined to divide the organoids in bins, and number of positive cells, mean fluorescence intensity, and area for any given ROI was determined. Similarly, for quantification of cell abundance, positive cells for each marker were manually counted and normalized over $DAPI^+$ cells. Quantifications were performed across multiple regions and multiple FeBOs using at least n = 2 different FeBO lines. Quantification was performed by two independent investigators.

Transmission electron microscopy

FeBOs in expansion and maturation medium were fixed with 1.5% glutaraldehyde in 0.1M cacodylate buffer for 24 hrs at 4°C. Then, organoids were washed with 0.1M cacodylate buffer and postfixed with 1% osmium tetroxide in the same buffer containing 1.5% potassium ferricyanide for 1 hr at 4°C in the dark. The samples were dehydrated in ethanol, infiltrated with Epon resin for 2 days, embedded in the same resin and polymerized for 48 hrs at 60°C. Ultrathin sections of 50 nm were obtained using a Leica Ultracut UCT ultramicrotome and mounted on Formvar-coated copper grids. They were stained with 2% uranyl acetate in water and lead citrate. The sections were observed in a Tecnai T12 electron microscope equipped with an Eagle 4kx4k CCD camera and large electron microscopy overviews were collected using the principles and software described previously.[105]

RNA extraction and qPCR analysis

For preparation of RNA from FeBOs and PSC-derived brain organoids/spheroids (all entire organoids) as well as human fetal brain tissues (pieces of tissue) were first washed once with 1X PBS, cut using micro-dissecting scissors, and then collected in 1 ml TRIzol Reagent. The samples were fully lysed by mechanical shearing (repetitive pipetting) and then snap-frozen in liquid nitrogen. RNA was extracted using isopropanol precipitation using the manufacturer's protocol and resuspended in sterile water. Extracted RNA was stored at -80°C. For qPCR analysis, RNA concentration and purity were determined using a NanoDrop spectrophotometer. As initial input, 250 ng of RNA was used for cDNA production using the SuperScript IV kit. The cDNA reaction was diluted 1:10, and 2 μl of the diluted cDNA was used for each qPCR reaction. qPCR reactions were performed using the iQ SYBR Green Supermix and the qPCR primers listed in Table S4. For each experiment and each organoid, technical triplicates were performed across multiple organoids and/or lines.

Bulk RNA sequencing, analysis, and deconvolution

For bulk RNA sequencing of FeBOs, RNA was extracted and processed as described above from organoids derived from dorsal and ventral forebrain, either in expansion medium or after 10 days in maturation medium, and from different donors and at different culture ages, as indicated in the text. Details on bulk RNA sequencing samples from morphogen experiments are described above. RNA integrity was measured using the Agilent RNA 6000 Nano kit with the Agilent 2100 Bioanalyzer and RNA concentrations were determined using the Qubit RNA HS Assay Kit. RIN values of RNA samples were typically 9.5-10 and only samples with RIN >8.5 were used for library preparation. RNA libraries were prepared using TruSeq Stranded mRNA polyA kit and paired-end (2x50 bp) sequenced on an Illumina Nextseq 2000. Library preparation and sequencing was performed by USEQ (Utrecht Sequencing Facility). Reads were mapped to the human GRCh37 genome assembly. From the dataset, we first filtered out lowly expressed genes (<20 transcript counts across all samples). Normalization and differential gene expression analyses were performed using the DESeq2 package[96] (1.36.0) in RStudio environment. Considered $\log_2$ fold changes and significance (p-values) are indicated in the figure legends. Gene Ontology analyses were performed using either EnrichR or Panther. Normalized transcript counts were used for analysis and data visualization. Data visualization was performed either using ggplot2 in RStudio environment or GraphPad Prism (9.4.1). PCA, correlation plots, hierarchical clustering, and heatmaps were calculated and plotted using the factoextra, corrplot, dendextend, and ComplexHeatmap packages, respectively. CIBERSORTx[97] was used for estimation of cell class abundance from bulk RNA sequencing. Gene expression profiles for the different clusters assigned to the main cell classes (stem cells/progenitors, cycling progenitors, neurons, astrocytes) obtained from the FeBO single-cell sequencing dataset (see below) were extracted as pseudobulk, by aggregating reads coming from cells belonging to the same cell type (as defined by clusters), after creating a SingleCellExperiment object and then using the ‘‘aggregate.Matrix’’ function from the Matrix.utils package. A gene list was obtained by combining the top expressed genes per the different cell classes and this was used as input signature file to probe each bulk RNA sequencing sample for deconvolution using CIBERSORTx. VoxHunt[98] analysis was performed to further confirm the qPCR assignment of regional identity on whole transcriptomes of human fetal brain tissue pieces by mapping to the mouse embryo brain E13.5.

Single-cell RNA sequencing and bioinformatic analysis

Cells from dorsal and ventral forebrain FeBOs (6 months in culture, derived from GW14 tissue) both in expansion medium and after 5 days in maturation medium were used for single-cell sequencing. To evaluate FeBO single-cell profile stability in culture, we additionally collected cells from dorsal forebrain FeBOs 2 months in culture (derived from GW15 tissue) both in expansion medium and after 5 days in maturation medium. The collected organoids were cut into smaller pieces and washed 2-3 times with wash buffer to remove possible cellular debris. The organoid pieces were then collected in a tube and washed 2 times with HBSS without calcium and magnesium. Multiple organoids of the same condition were pulled together and were dissociated using the Neural Dissociation kit (P), according to the manufacturer’s instruction. The second enzymatic step was supplemented with 10 μl of 100 U/μl of DNAse I and was incubated for approximately 40 min with regular gentle pipetting using a blunt-cut P1000 pipette tip. The dissociated cells were washed twice with HBSS with calcium and magnesium and then twice with HBSS without calcium and magnesium. Centrifugation steps were performed at low speed (100 *g*) in a swinging bucket for 5 min. Viability was calculated and only samples with >90% viable cells for the expansion condition and >80% for the maturation condition were used. For preparation of dissociated cells in maturation condition, given the lower general viability, the Dead Cell Removal kit was used with MS columns after dissociation according to the manufacturer’s instructions. Live cells were manually counted using Trypan blue and resuspended in 1X PBS containing 0.04% BSA at an optimal concentration of 700-1200 cells/μl. Library preparation and sequencing was performed by the Single Cell Genomics facility of the Princess Máxima Center. Approximately 16,000 cells per sample were loaded onto a Chromium Single Cell B or G chip and used for library preparation using the Chromium Next GEM Automated Single Cell 3’ Library and Gel Bead Kit v3/v3.1 (10X Genomics) according to the manufacturer’s instructions. Each library was sequenced using the NovaSeq 6000 SP v1.5 (200 cycles) flowcell, using the following number of cycles, Read 1: 28, i7: 10, i5: 10 and Read 2: 91. Mapping and UMI counting were performed using Cell Ranger software (5.0.1). In general, >98% of barcodes and UMI were valid, >92% of reads could be mapped to the genome, and >50% to the transcriptome. Bioinformatic analyses were performed using Seurat 4.0 in RStudio environment.[99] The respective expansion and maturation libraries were combined using the merge function, and cells with <200 detected genes, >6000 genes, or >20% mitochondrial content were removed. Additionally, low quality cells were removed, resulting in 28,939 cells for the full ventral FeBO dataset (expansion + maturation), and 53,732 cells for the full dorsal FeBO dataset (expansion + maturation from both early and late passage integrated, see below). Preprocessing of the data was performed according to the suggested analysis pipeline from Seurat developers. Briefly, gene expression normalization was performed by employing a global-scaling normalization method ‘‘LogNormalize’’ with the default scale factor of 10,000. The ‘‘FindVariableFeatures’’ function was used to find the top 2000 most variables genes in the dataset, using the standard selection method ‘‘vst’’ and prior to calculation of principal component analysis the dataset was scaled by applying linear transformation so that the average expression for each gene across cells was 0 and the variance across cells was 1. Dimensionality of the dataset was determined by using the function ‘‘ElbowPlot’’ and clusters were determined with the functions ‘‘FindNeighbors’’ and ‘‘FindClusters’’. For dorsal FeBOs, the early and late passage libraries were integrated using the ‘‘FindIntegrationAnchors’’ and ‘‘IntegrateData’’ functions.[106] Global cell type signatures were defined based on multiple marker genes previously described in the literature (Table S2). The dataset was probed for these signatures using the ‘‘AddModuleScore’’ function. Based on this collective information, defined clusters were assigned to specific identities. For subclustering analyses, cells with a defined identity (neurons and neurogenic progenitors) were selected and subjected to a further clustering step. For definition of cell identity in the clustering and subclustering analyses, a large panel of known markers based on literature annotation were used (Table S2). Cluster comparison between early and late passage dorsal forebrain

FeBOs was performed in an identical manner as described below for the organoid-tissue cluster correlation. Data visualization was performed with Seurat plotting functions in RStudio environment, using UMAP, Violin Plots, and Dot Plots.

Single-cell RNA sequencing comparison with primary human fetal brain tissue

To compare the single-cell transcriptomes of FeBOs with primary human fetal tissue, we used published datasets from Bhaduri et al.,[37] Yu et al.,[42] and Fan et al.[52] For the organoid clusters to fetal tissue clusters correlation, single-cell sequencing datasets of GE GW14 and cortex GW10-14 (both from Bhaduri et al.[37]) were first normalized, filtered and clustered using Seurat, as described above. Then, for each gene and each cluster, a specificity score was calculated as previously reported.[107] Briefly, the score was based on the expression level of each gene per cluster, as the log2FC multiplied by its enrichment ratio (*i.e.* the percentage of cells expressing the gene in the respective cluster divided by the percentage of cells in all other clusters expressing the marker). A matrix with these values was created for all genes and for all clusters and the different matrices from the different datasets were merged. Clusters D3 and V0 for dorsal and ventral forebrain FeBOs, respectively, were excluded in this analysis due to their low specificity (V0) or *DDIT4*$^+$ stressed state (D3). Using the corrplot package, correlation analysis was performed by calculating Pearson's correlation coefficients among clusters. For tissue-FeBOs dataset integration, for both dorsal and ventral forebrain FeBOs, two independent single-cell sequencing datasets on primary tissues were used (GE GW14 from Bhaduri et al.[37] and GE GW12 from Yu et al.[42]; cortex GW10-14 from Bhaduri et al.[37] and cortex GW11-12 from Fan et al.[52]). To integrate the single-cell sequencing profiles of FeBOs with the respective single-cell sequencing profiles of human fetal tissue, the datasets were first merged using the merge function and each object was independently normalized and variable features were identified using the "FindVariableFeatures" function. Then, features were selected that were repeatedly variable across the datasets. Cross-dataset pairs of cells were identified using the "FindIntegrationAnchors" function and integration of the datasets was performed using the function "IntegrateData". Cluster identification and UMAP visualization was performed as described above. For ventral forebrain FeBOs, tissue signatures for "radial glial", "proliferation", and "neuronal", were defined based on marker genes for the respective clusters using the GE GW14 tissue dataset. Gene (specificity) scores for these tissue signature markers were calculated and plotted for each cluster (excluding V0, as mentioned above), as described above. To compare ventral forebrain FeBO profiles with human fetal GE tissue profiles of different developmental stages (GW14-GW25),[37] pseudobulk comparisons were performed, after individually generating pseudobulk counts from the ventral forebrain FeBOs as well as for each fetal GE tissue dataset. Raw counts and metadata information were first extracted from the Seurat object (upon filtering) and stored using the SingleCellExperiment package. All cells belonging to each dataset were assigned to the same identity (per dataset) and then the raw counts were aggregated for each grouped identity using the "aggregate.Matrix" function. Correlation between the pseudobulks derived from ventral forebrain FeBOs and fetal GE tissues was calculated by Pearson's correlation using the corrplot package based on the top 50 differentially expressed genes per cluster, as identified using the "FindMarkers" function with a significance p value cut-off of 0.05.

Secretome and proteome analysis by LC-MS/MS

For secretome analysis, intact FeBOs, FeBOs shortly after splitting (4 days), and FeBO-derived neurospheres formed upon single-cell dissociation of a FeBO were refreshed with new medium. The conditioned media containing the secreted products were collected after 24 hrs. As blank, we used culture medium. The conditioned media were centrifuged twice for 10 min at 20,000 *g* to remove any possible cell debris, supernatant was collected, snap frozen and stored at -80°C until analysis. The conditioned media were denatured with 2M urea, pH adjusted to 8.0, reduced in 10 mM dithiothreitol at 20°C for 1 h, and then alkylated in 20 mM iodoacetamide at 20°C for 0.5 h in the dark. Secreted proteins were digested sequentially with Lys C (1:50) and Trypsin (1:50) for 4 hrs and 16 hrs, respectively. Digested peptides were acidified to 2% formic acid, and diluted to 1 ml for peptide cleanup by c18 1cc Vac cartridges (Waters). Desalted peptides were dried by vacuum centrifugation, and stored at -80°C for further use. Peptides were reconstituted with 2% formic acid and analyzed in triplicates on an Orbitrap Exploris 480 mass spectrometer coupled to an UltiMate 3000 UHPLC system, that consisted of a μ-precolumn (C18 PepMap100, 5 μm, 100 Å, 5 mm × 300 μm), and an analytical column (120 EC-C18, 2.7 μm, 50 cm × 75 μm; Agilent Poroshell). Solvent A was made of 0.1% formic acid in water and solvent B was 0.1% formic acid in 80% acetonitrile, 20% water. Peptides were resolved on a 175 min gradient from 10 to 40% Solvent B. Mass spectrometry data were acquired in data-dependent acquisition mode. MS1 scans were acquired between m/z 375-1600 at a resolution of 60,000, upon signal accumulation to AGC target of 1e6. Multiply charged precursors starting from m/z 120 were selected for further fragmentation. Higher energy collision dissociation (HCD) was performed with 28% normalized collision energy (NCE), at a resolution of 30,000, upon signal accumulation to AGC target of 1e5. An isolation window of 1.4 m/z and dynamic exclusion of 24s were used. MS raw files were searched with MaxQuant (1.6.10.0) against the human UniProt database (version April 22, 2021) using the integrated Andromeda search engines. Protein N-terminal acetylation and methionine oxidation were added to variable modification, whereas cysteine carbamidomethylation was added to fixed modification. Trypsin/P was set as the enzyme for digestion and up to 2 missed cleavages were allowed. Label-free quantification (LFQ) was enabled. FDR of 1% was set at both PSM and protein level by using a reverse decoy database strategy. LFQ algorithm and the match-between-run feature were enabled for protein identification against an in-house ECM protein library. A 1% false discovery rate (FDR) was applied for both peptide and protein identification. For proteome analysis, expanding dorsal forebrain FeBOs (ca. 3 months cultured; P1, P2, P8), primary human fetal brain tissues (P3, P4), unguided PSC-cerebral organoids (day 40, two batches; P5, P6), and PSC-cortical spheroids (day 40; P7) were washed twice with 1X PBS, after which all liquid was removed. The samples were cut into smaller fragments and snap-frozen at -80°C until further use. Total protein digests were analyzed in the same mass spectrometer with the same settings and LC-gradient as described above. PCA, correlation plots, and heatmaps were generated using the factoextra, corrplot, and ComplexHeatmap packages in RStudio environment.

QUANTIFICATION AND STATISTICAL ANALYSIS

Statistical details of experiments can be found in the figure legends and STAR Methods and include information on sample sizes and the statistical tests used.

Supplemental figures

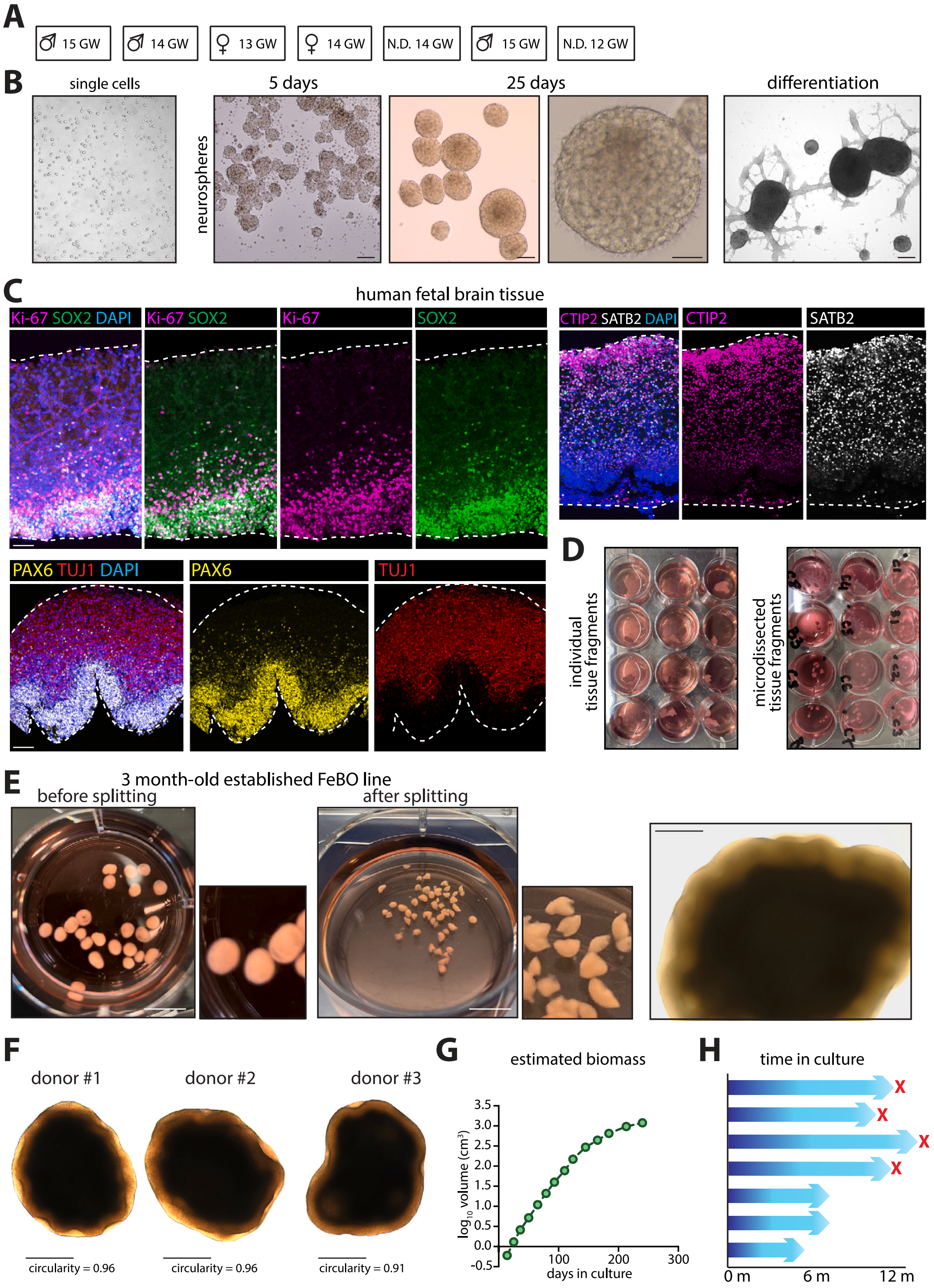

(legend on next page)

Figure S1. Donor tissue characteristics and features of FeBO line establishment, related to Figure 1

(A) Overview of the donor characteristics of the different human fetal tissues used in this study to derive forebrain FeBOs.

(B) Representative brightfield images of dissociated single cells from human fetal brain tissue (left). Representative brightfield images of 3D cell aggregates (neurospheres) forming over time from the dissociated single cells (middle). Representative brightfield images of differentiated neurospheres, showing plate attachment and direct neuronal differentiation in differentiation medium (right). Scale bars from left to right, 50 μm, 100 μm, 50 μm, 70 μm.

(C) Representative immunofluorescence images of human fetal brain tissue from which FeBOs were derived for the indicated markers. Scale bars, 100 μm (top), 50 μm (bottom).

(D) Representative images of single individual fragments isolated from human fetal brain tissue before (left) and after (right) further processing (cutting) the fragments, which are subsequently used to establish FeBOs.

(E) Representative images of multiple grouped FeBOs from an established organoid line before and after splitting. To the right, a representative brightfield image at higher magnification of an established single FeBO. Scale bars, 1 cm (left and middle), 500 μm (right).

(F) Representative brightfield images of FeBOs derived from different donors. Organoid shapes (circularity) are indicated. Scale bars, 1 mm.

(G) Estimated total biomass produced by the expansion of a FeBO line during 266 days, based on the splitting ratios over time, with the y axis plotted on $\log_{10}$ scale.

(H) Overview of the number of months in culture of different FeBO lines since line derivation. Red cross indicates the moment of termination of the FeBO line.

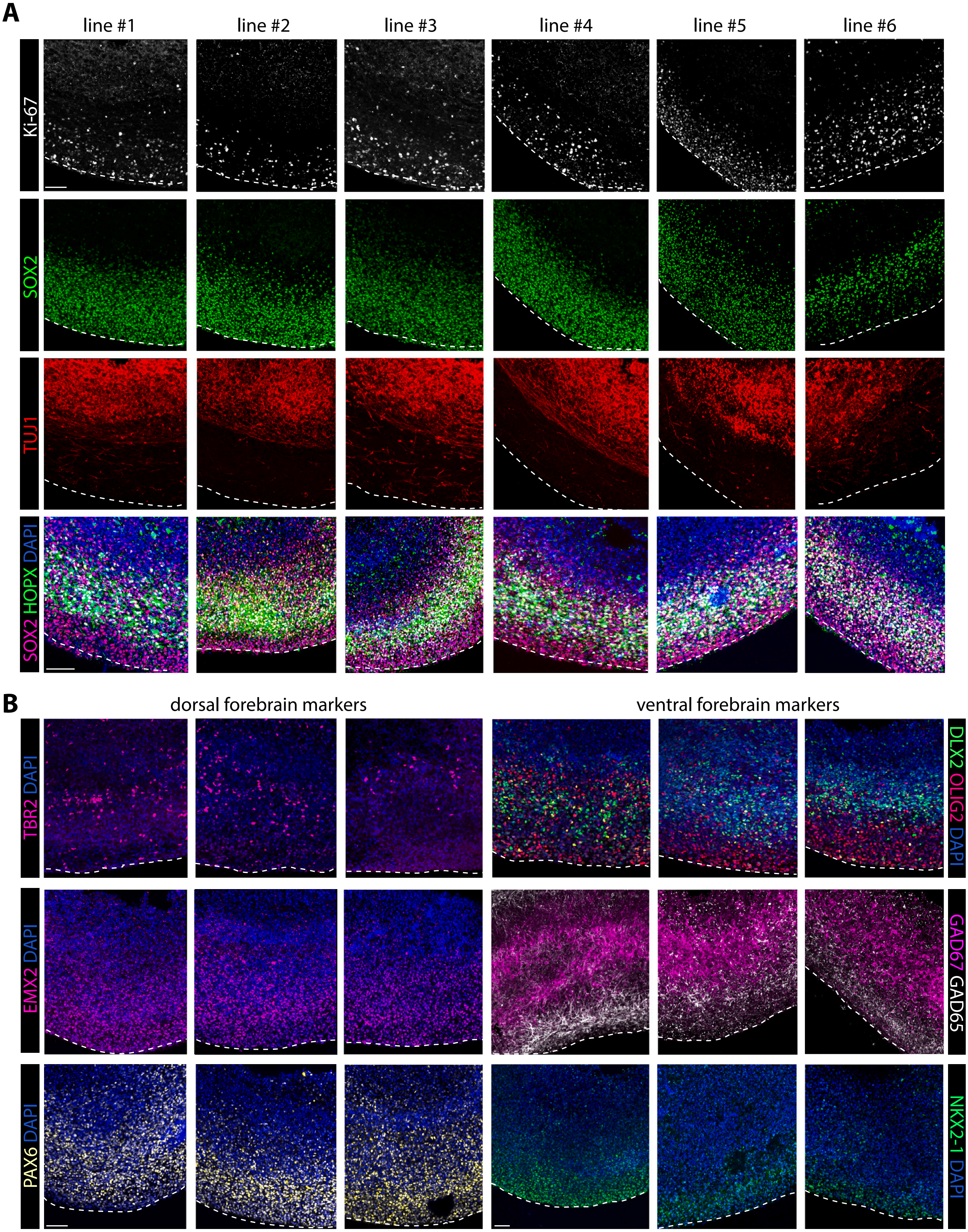

(legend on next page)

Figure S2. FeBO reproducibility across different lines and donors, related to Figures 1 and 2

(A) Representative immunofluorescence images for the indicated markers depicting cellular composition and organization in different FeBO lines derived from different donors (2–3 months expanded). Scale bars, 100 μm.

(B) Representative immunofluorescence images for the indicated dorsal- and ventral-enriched forebrain markers depicting reproducibility across different 2–3-month-expanded dorsal forebrain FeBO lines (left) and ventral forebrain FeBO lines (right). Scale bars, 100 μm.

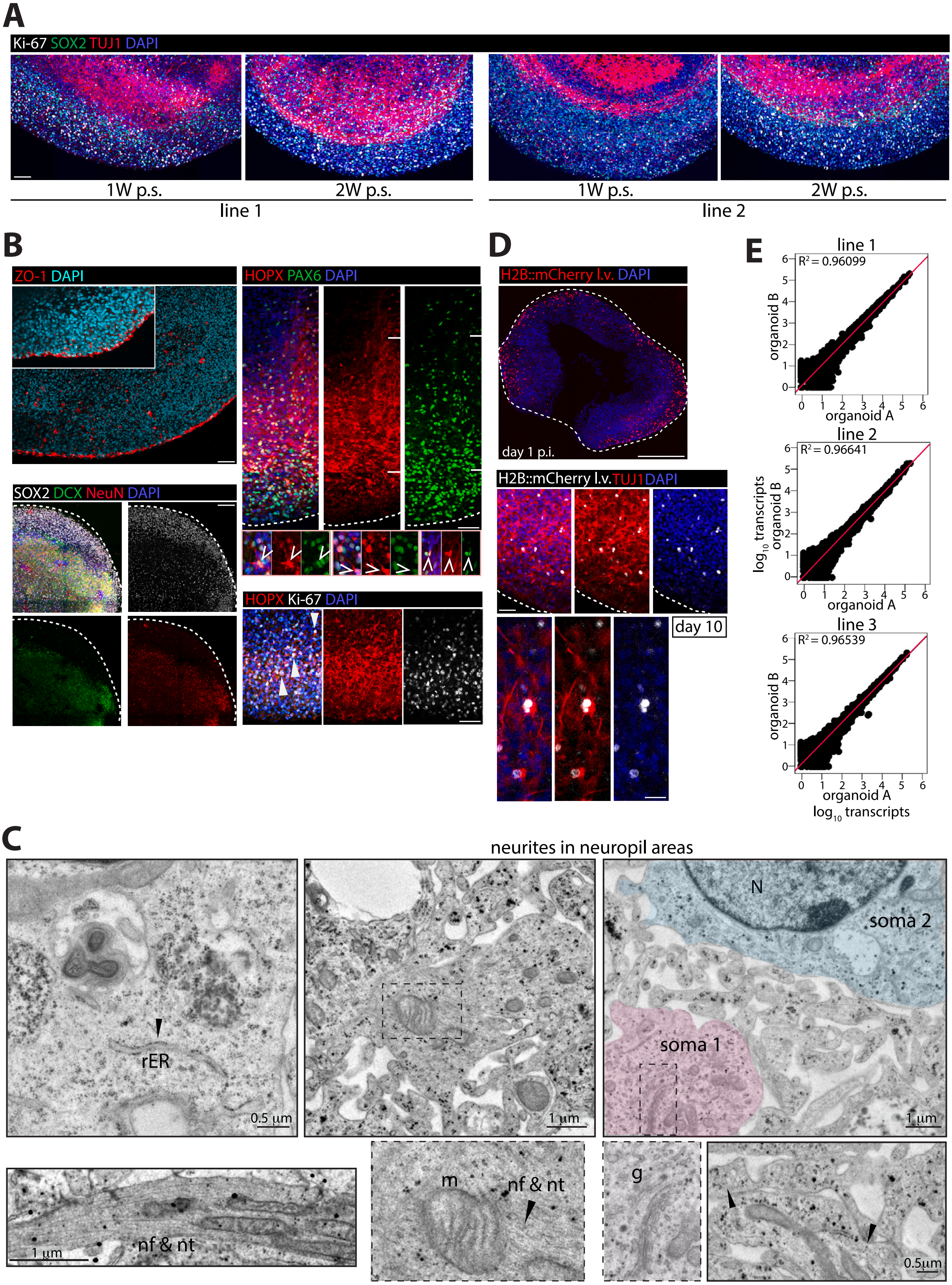

(legend on next page)

Figure S3. Characterization of FeBOs through immunofluorescence, tracing by viral labeling, and transmission electron microscopy, related to Figure 1

(A) Representative immunofluorescence images for the indicated markers of two different FeBO lines 1 week and 2 weeks post splitting (p.s.). Scale bars, 100 μm.

(B) Representative immunofluorescence images for the indicated markers in FeBOs. White lines in the staining for HOPX and PAX6 indicate the presence of a VZ- and SVZ-like layer in the FeBOs. Open arrowheads point at examples of cells expressing both HOPX and PAX6, and closed arrowheads point at colocalization of HOPX and Ki-67. Scale bars, 200 μm (top left), 50 μm (top right), 200 μm (bottom left), 50 μm (bottom right).

(C) Representative transmission electron microscopy images of FeBOs visualizing typical brain features, including stacked endoplasmic reticuli, multiple processes in abundant neuropil areas within cell somata, stacked cisternae of the Golgi apparatus, presence of synaptic vesicles (black arrowheads) and axons with neurofilaments and neurotubules. g, Golgi apparatus; m, mitochondria; N, nucleus; rER, ribosomal endoplasmic reticulum; nf, neurofilament; nt, neurite.

(D) Top: representative image of a FeBO infected with H2B::mCherry lentiviruses at 1 day post infection (p.i.). Middle and bottom: representative immunofluorescence images of a FeBO infected with H2B::mCherry lentiviruses stained for the neuronal marker TUJ1 at 10 days p.i., demonstrating the presence of mCherry$^+$; TUJ1$^+$ cells. Scale bars, 500 μm (top), 50 μm (middle), 25 μm (bottom).

(E) Whole transcriptome stability comparisons of individual organoids across different FeBO lines.

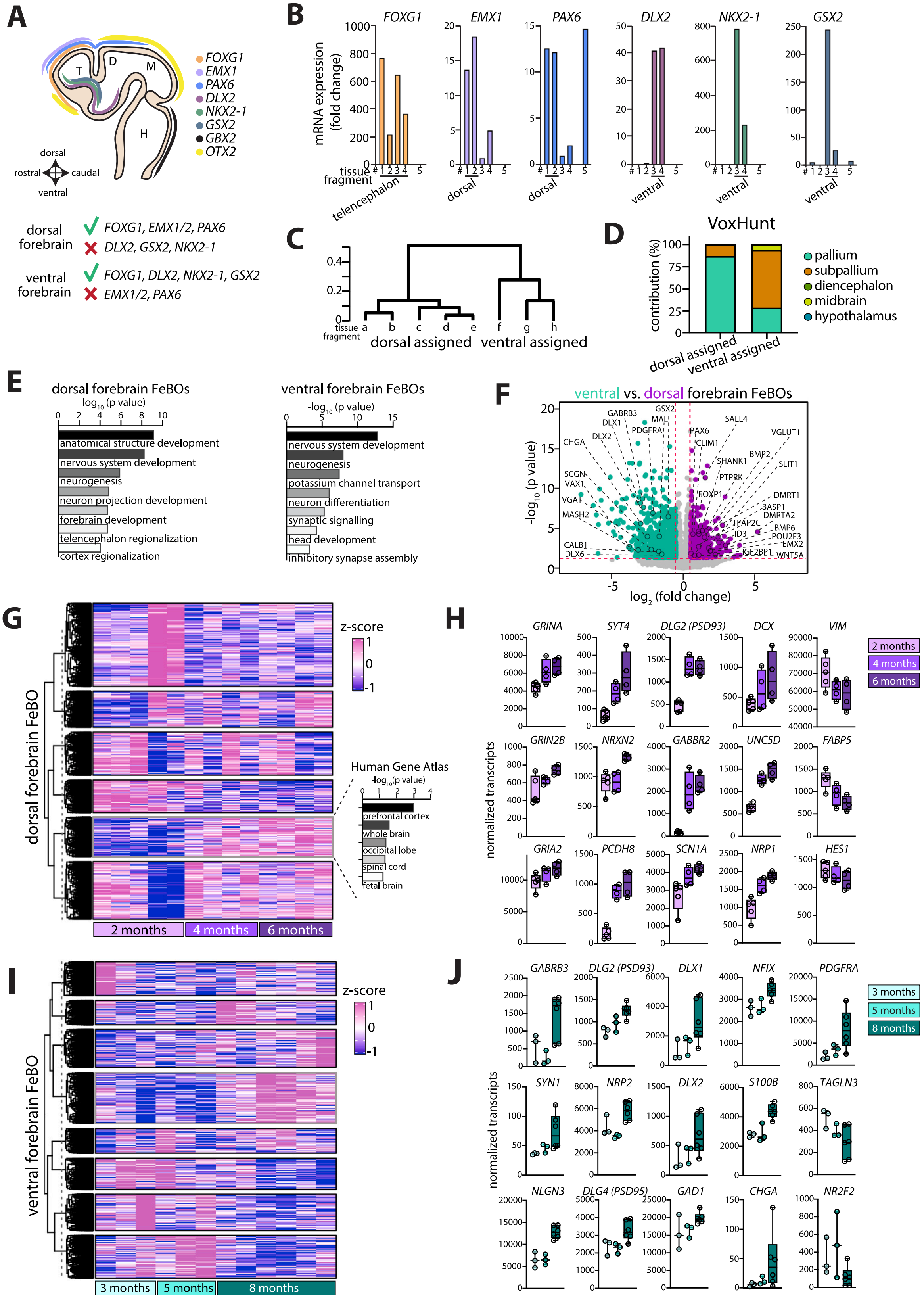

(legend on next page)

Figure S4. Assignment of brain tissue region identity and transcriptomic characterization of regional FeBOs, related to Figure 2

(A) Schematic representing the expression of typical markers in the different regions of the developing human fetal brain (left). T, telencephalon; D, diencephalon; M, midbrain; H, hindbrain. Markers used to define dorsal vs. ventral forebrain donor tissue fragment identities are depicted on the bottom.

(B) Representative example of qPCR analysis of the expression of a panel of markers in different pieces of human fetal brain (numbered 1–5) used for FeBO line establishment. Tissue sample 5 does not have an assigned tissue identity due to the lack of a typical expression profile and was not used for FeBO line generation.

(C) Unsupervised hierarchical clustering of whole transcriptomes of different human fetal brain tissue fragments.

(D) VoxHunt analysis based on E13.5 mouse brain similarity on bulk RNA sequencing data of dorsal-assigned and ventral-assigned human fetal brain pieces (pallial identity: dorsal-assigned; subpallial identity: ventral-assigned).

(E) Selected GO-terms on significantly upregulated genes in dorsal (left) and ventral (right) forebrain-derived FeBOs when comparing dorsal vs. ventral forebrain-derived FeBOs.

(F) Volcano plot showing differentially expressed genes between dorsal and ventral forebrain-derived FeBOs ($|\log_2 FC| > 0.5$ and $p < 0.05$). Significant upregulated genes are depicted in green (ventral) and purple (dorsal).

(G) Heatmap depicting the whole transcriptome of dorsal forebrain FeBOs from different donors across different time points in culture. The highlighted cluster comprises genes with gradual changes in expression during long-term culture. Selected terms on genes selected from this cluster from the human gene atlas are shown.

(H) Expression of selected genes from the highlighted cluster in gray (G) in dorsal forebrain FeBOs during long-term expansion. Each dot represents an independent FeBO.

(I) Heatmap as in (G) depicting the transcriptome of ventral forebrain FeBOs from different donors over culture time.

(J) Expression of selected genes from the highlighted cluster in gray (I) in ventral forebrain FeBOs during long-term expansion. Each dot represents an independent FeBO.

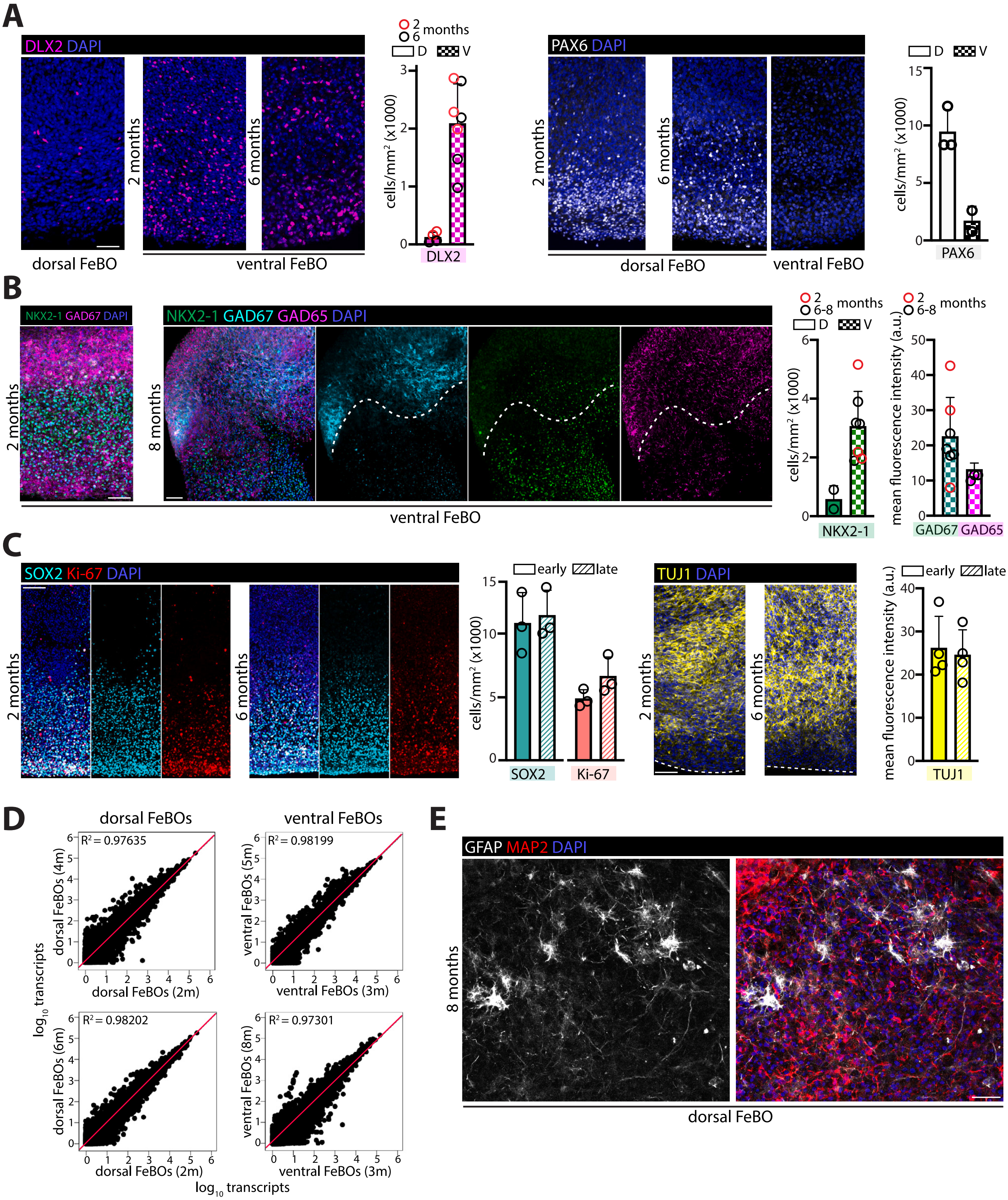

Figure S5. Stability of regional FeBO identity over prolonged culturing, related to Figure 2

(A) Representative immunofluorescence images for DLX2 and PAX6 in 2- and 6-month-expanded dorsal (left) and ventral (right) forebrain FeBOs. Quantifications of the cells positive for the indicated marker per organoid area are presented. Scale bars, 100 μm.

(legend continued on next page)

(B) Representative immunofluorescence images for the indicated markers in 2- and 6-to-8-month-expanded ventral forebrain FeBOs. Quantification of the cells positive for the indicated marker (NKX2-1$^+$) per organoid area or mean fluorescence intensity (GAD67 and GAD65) is presented. Scale bars, 100 μm.

(C) Representative immunofluorescence images for the indicated markers in 2- and 6-month-expanded FeBOs. Quantifications of the cells positive for the indicated marker per organoid area are presented. Scale bars, 200 μm (left), 100 μm (right).

(D) Representative immunofluorescence images for the astrocytic marker GFAP and neuronal marker MAP2 in 8-month-expanded dorsal forebrain FeBOs. Scale bars, 100 μm.

(E) Whole transcriptome stability comparisons of dorsal forebrain and ventral forebrain FeBOs of different culture ages.

In (A)–(C), each dot represents quantification in an independent FeBO.

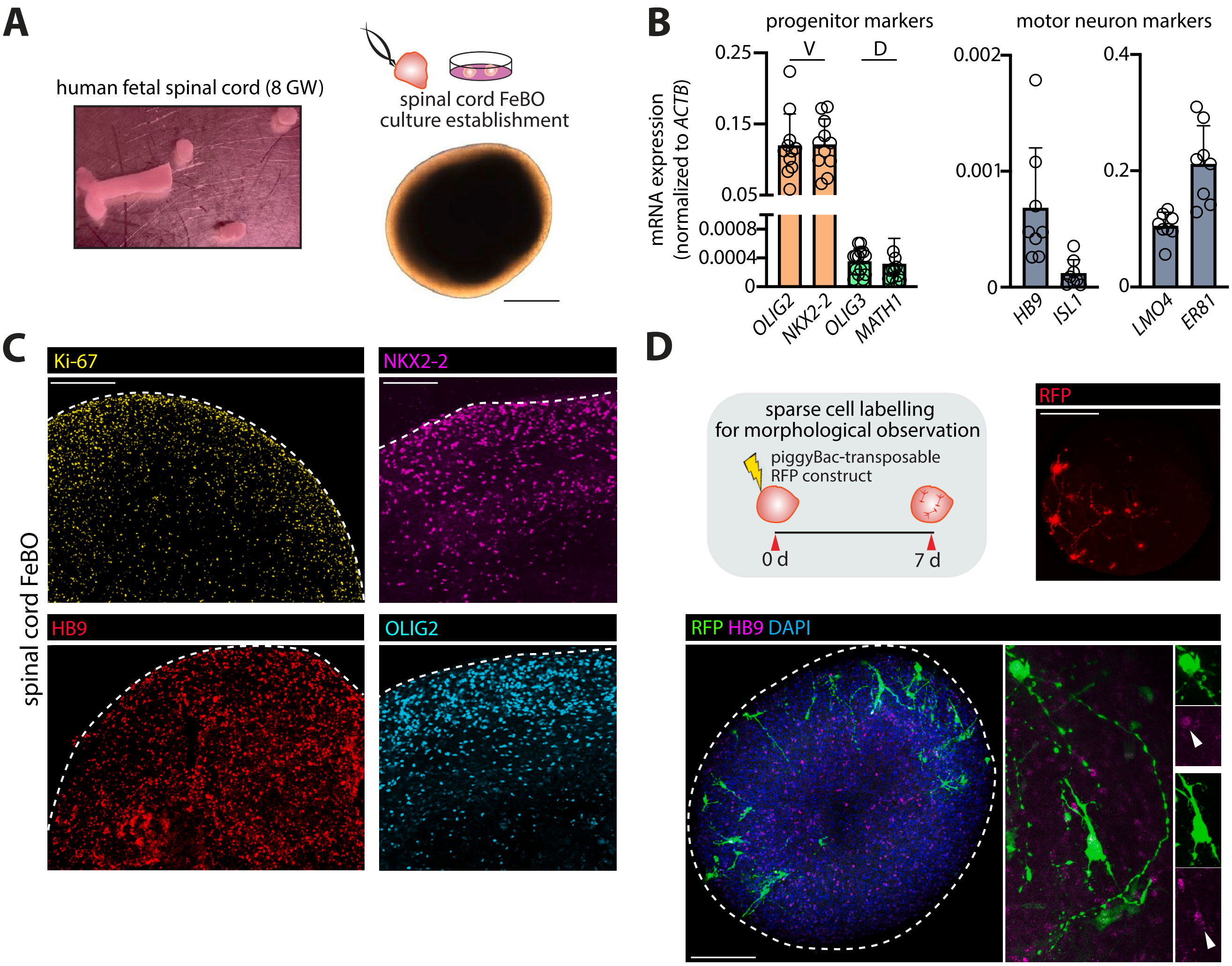

Figure S6. Generation of FeBOs from human fetal spinal cord, related to Figure 2

(A) Brightfield image of human fetal spinal cord tissue (GW8), showing an intact part on the right and coronal sections around it, used for the generation of FeBOs (left). Representative image of a spinal cord FeBO (right). The entire spinal cord was used for culturing, without attempting to distinguish between more ventral and dorsal domains or more anterior and posterior regions. Scale bars, 0.5 mm.

(B) Relative mRNA expression (qPCR) of the indicated dorsal and ventral markers as well as motor neuron markers in spinal cord FeBOs, suggesting their ventral-like identity.

(C) Representative immunofluorescence images for the indicated markers in spinal cord FeBOs. Scale bars, 250 μm (left), 150 μm (right).

(D) Strategy to sparsely label cells in spinal cord FeBOs (top). Representative immunofluorescence images showing the morphology of RFP^+; $HB9^+$ neurons. Scale bars, 100 μm (top), 500 μm (bottom).

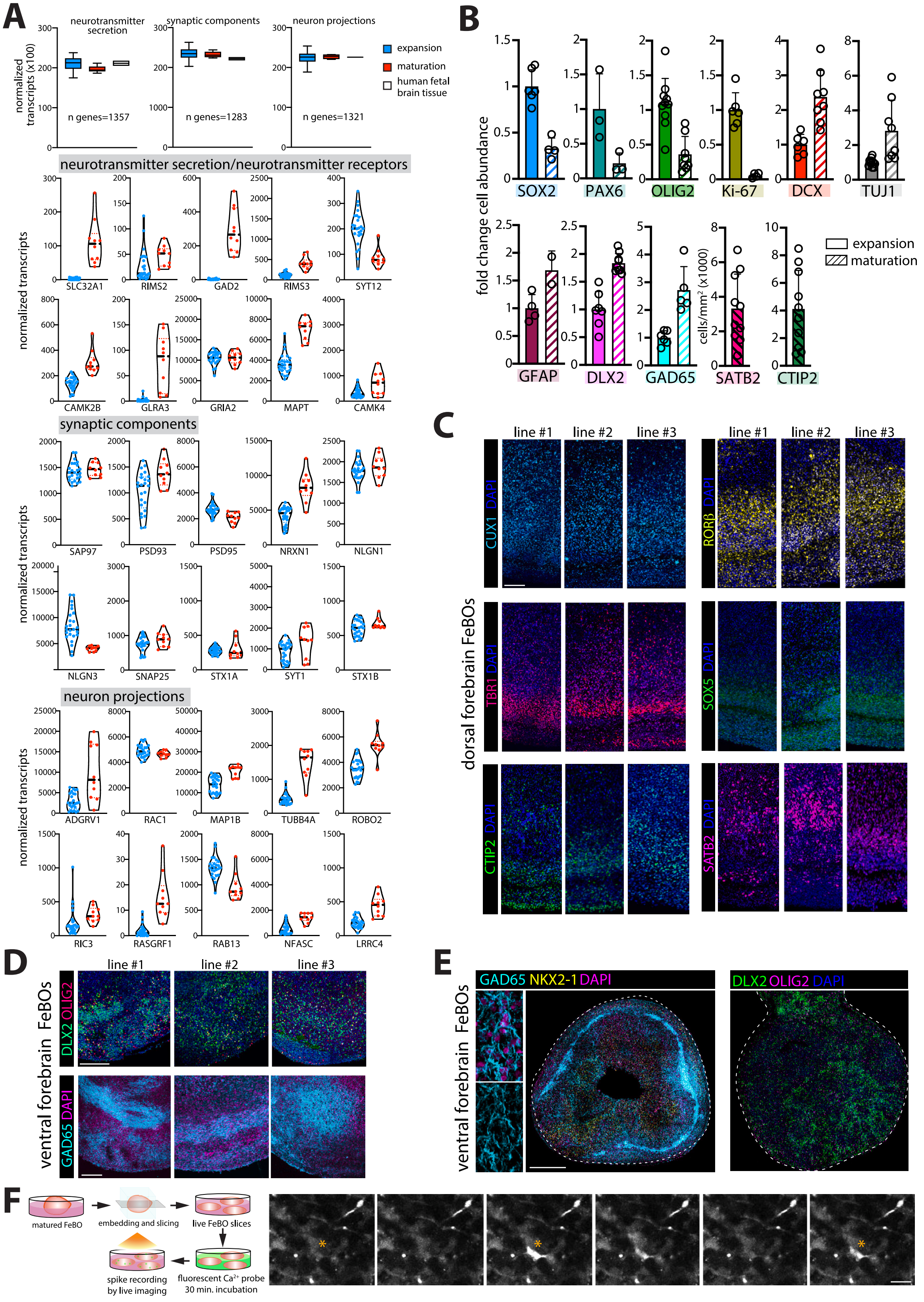

(legend on next page)

Figure S7. Further FeBO maturation as assessed by transcriptomic characterization, immunofluorescence, and functional analysis, related to Figure 3

(A) Top: analysis of cumulative mRNA transcript counts belonging to specific neuronal features (derived from the indicated GO-annotation) in expanding and matured FeBOs as well as in human fetal brain tissue. Bottom: violin plots showing the expression of selected genes involved in specific neuronal features. Each dot represents normalized transcript counts from bulk RNA sequencing of an independent FeBO.

(B) Quantification of marker expression in FeBOs in maturation and/or expansion medium based on immunofluorescence analysis. Each dot represents an independent FeBO.

(C) Representative immunofluorescence images for different neuronal markers in matured dorsal FeBOs across different lines (matured after 2–3 months expansion). Scale bars, 100 μm.

(D) Representative immunofluorescence images for the indicated markers in matured ventral FeBOs (matured after 2–3 months expansion). Scale bars, 200 μm.

(E) Representative immunofluorescence images for the indicated markers in matured ventral FeBOs. Note the bundle-like structure in which GAD65^{+} cells are sometimes organized (matured after 4 months expansion). Scale bars, 500 μm.

(F) Experimental strategy to measure electric activity in neurons by live imaging of matured FeBO slices (left). Representative example of a time course calcium imaging experiment (right). Asterisks point at electrically active neurons. Scale bars, 20 μm.

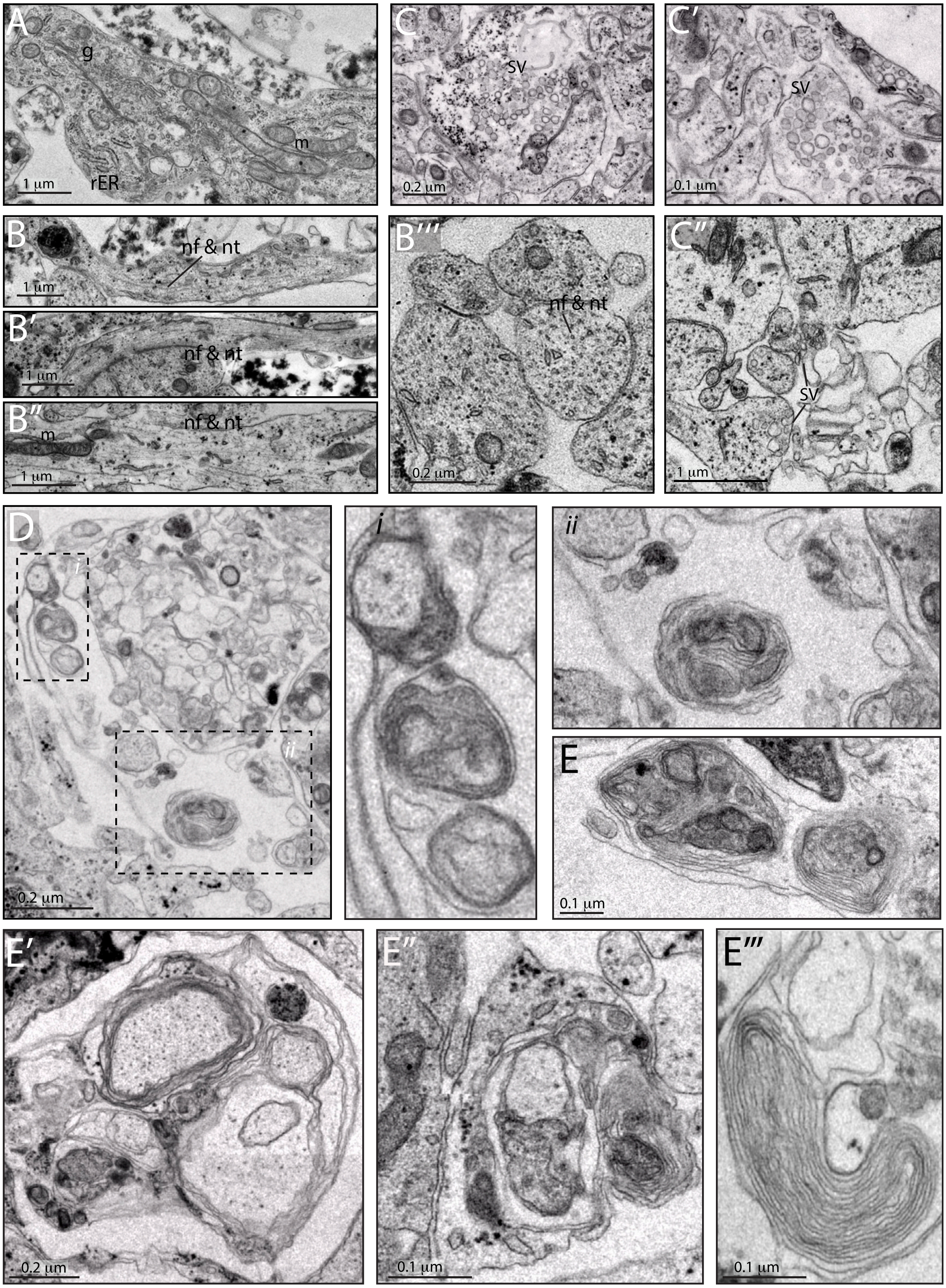

Figure S8. Transmission electron microscopy analysis on matured FeBOs, related to Figure 3

(A) Examples of neuronal subcellular structures, such as stacked Golgi cisternae and elongated mitochondria, in matured FeBOs. m, mitochondria; g, Golgi apparatus; rER, ribosomal endoplasmic reticulum.

(legend continued on next page)

(B) Examples of longitudinal sections of axons presenting with aligned neurofilaments (nf) and neurotubules (nt) throughout the axon length (B–B''); note the interspersed mitochondria (B''') a cross-section view of multiple axons is presented; note the evident sections of multiple neurofilaments (nf) and neurotubules (nt).

(C) Examples of synaptic neurotransmitter vesicle (SV) structures and multiple cell contacts (C-C′). Note that a zoom-in of (C') is also shown in Figure 3J.

(D) Examples of putative indications of early stages of oligodendrocytic myelin sheath-like structures wrapped around axons. High magnifications of marked areas are presented in *i* and *ii*.

(E) Further examples of putative indications of different degrees of myelination by oligodendrocytes (E–E'''). Note that a zoom-in of (E) is also shown in Figure 3J.

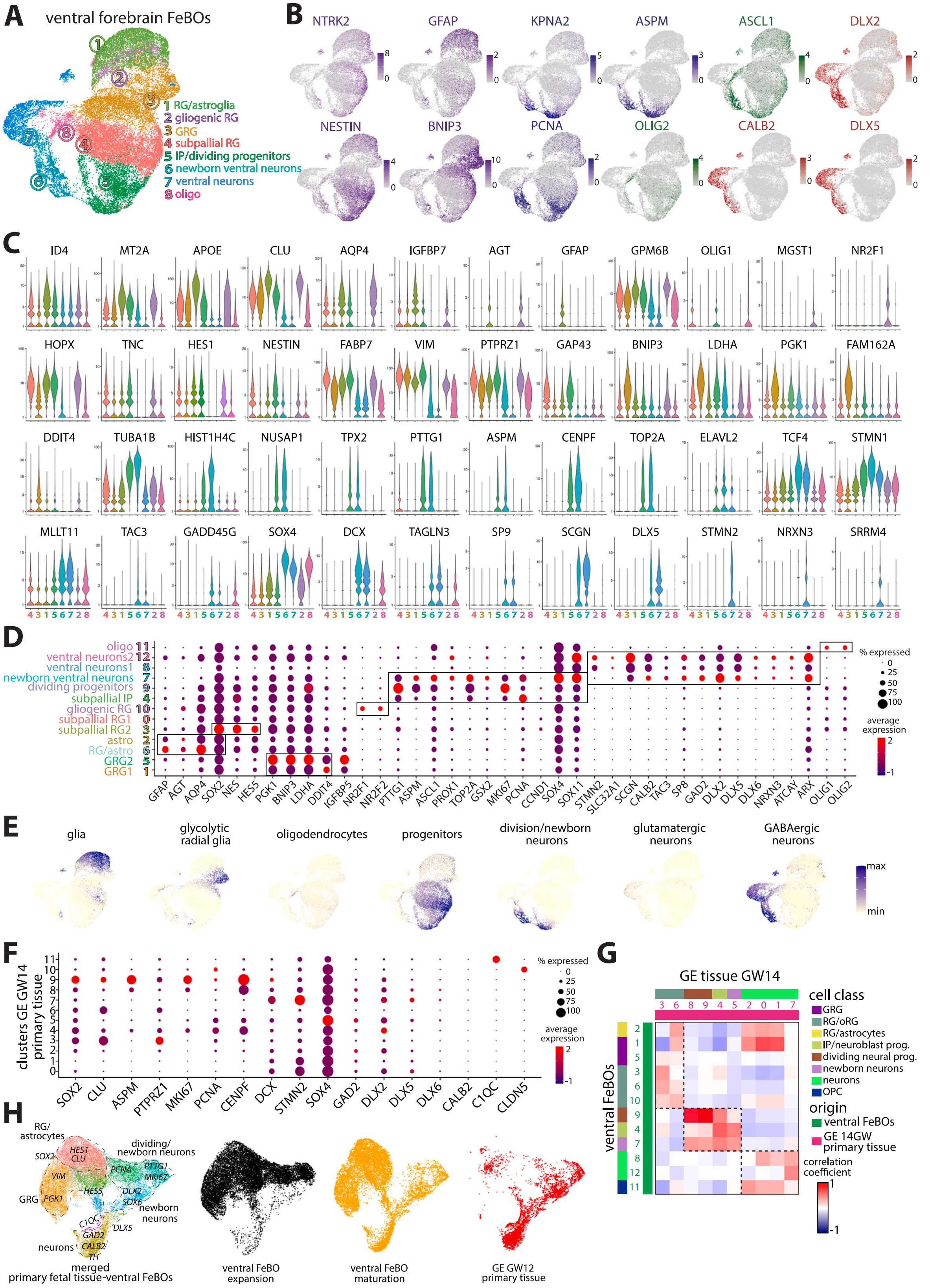

(legend on next page)

Figure S9. Single-cell sequencing analysis of ventral forebrain FeBOs, related to Figure 4

(A) UMAP of cells derived from the merged expanded and matured ventral forebrain FeBO datasets, assigned into the main cell classes.
(B) UMAP plots showcasing the expression of specific marker genes.
(C) Violin plots for multiple genes showing specific expression in the different main cell clusters, as defined in (A).
(D) Extended dot plot depicting expression of markers defining the different cell types and cluster identity, using the cluster annotation as in Figure 4A.
(E) Cell type-specific signature analysis. Each signature is based on a specific set of genes defined from previous studies (see Table S2).
(F) Dot plot depicting expression of markers defining the different cell types and cluster identities in primary GE tissue. Data were reanalyzed from Bhaduri et al.[37]
(G) Correlation plot comparing tissue (x axis) and organoid (y axis) clusters with assigned cell identities between ventral forebrain FeBOs and primary GE tissue. Note that the clusters only detected in tissue (vasculature and microglia) are not included, related to Figure 4E.
(H) UMAP representation showing the integration of the expanding and matured ventral forebrain FeBO datasets with the primary GE tissue (GW12) dataset from Yu et al.[42]

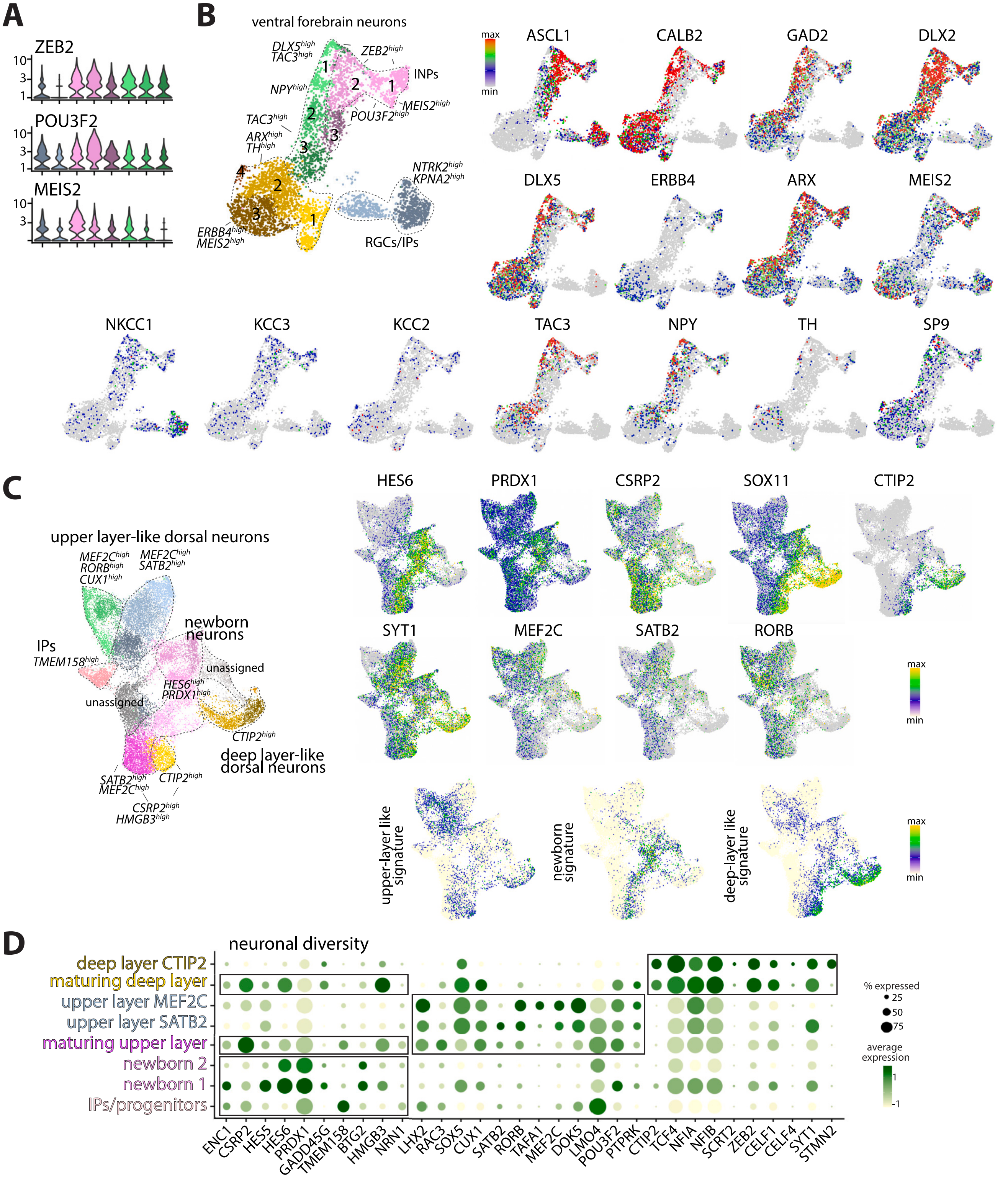

Figure S10. Identification of neurogenic and neuronal populations in ventral and dorsal forebrain FeBOs, related to Figure 4

(A) Violin plots demonstrating heterogeneity in the expression patterns of *ZEB2*, *POU3F2*, and *MEIS2* across the different neurogenic populations in ventral forebrain FeBOs.

(legend continued on next page)

(B) UMAP plot showing subclustering analysis on neurogenic and neuronal populations identified in dorsal forebrain FeBOs (also shown in Figure 4C) (left). UMAP plots showcasing the expression of specific neurogenic and neuronal markers for different classes of ventral forebrain neurons (right).

(C) UMAP plot showing subclustering analysis on neurogenic and neuronal populations identified in dorsal forebrain FeBOs (also shown in Figure 4J) (left). UMAP plots showcasing the expression of specific neurogenic and neuronal markers for the different classes of cortical neurons (right). On the bottom, cell type signature analysis for newborn glutamatergic neurons and various upper-layer (equivalent to cortical projection neurons-CPN) and deep-layer (equivalent to corticofugal projection neurons-CFuPN) neurons.

(D) Dot plot depicting expression of markers defining the different neurogenic and neuronal populations in dorsal forebrain FeBOs, including maturing upper-layer-like and deep-layer-like neurons co-expressing markers of newborn glutamatergic neurons (e.g., *ENC1*, *CSRP2*, *BACH2*, and *PRDX1*) and either markers of upper L2/3 and L4 neurons (e.g., *SATB2*, *MEF2C*, *POU3F2*, *CUX1*, and *RORB*) or deep-layer L5/L6 neurons (e.g., *CTIP2*, *NFIA*, *NFIB*, and *CELF1*) and their more mature subclasses (see C).

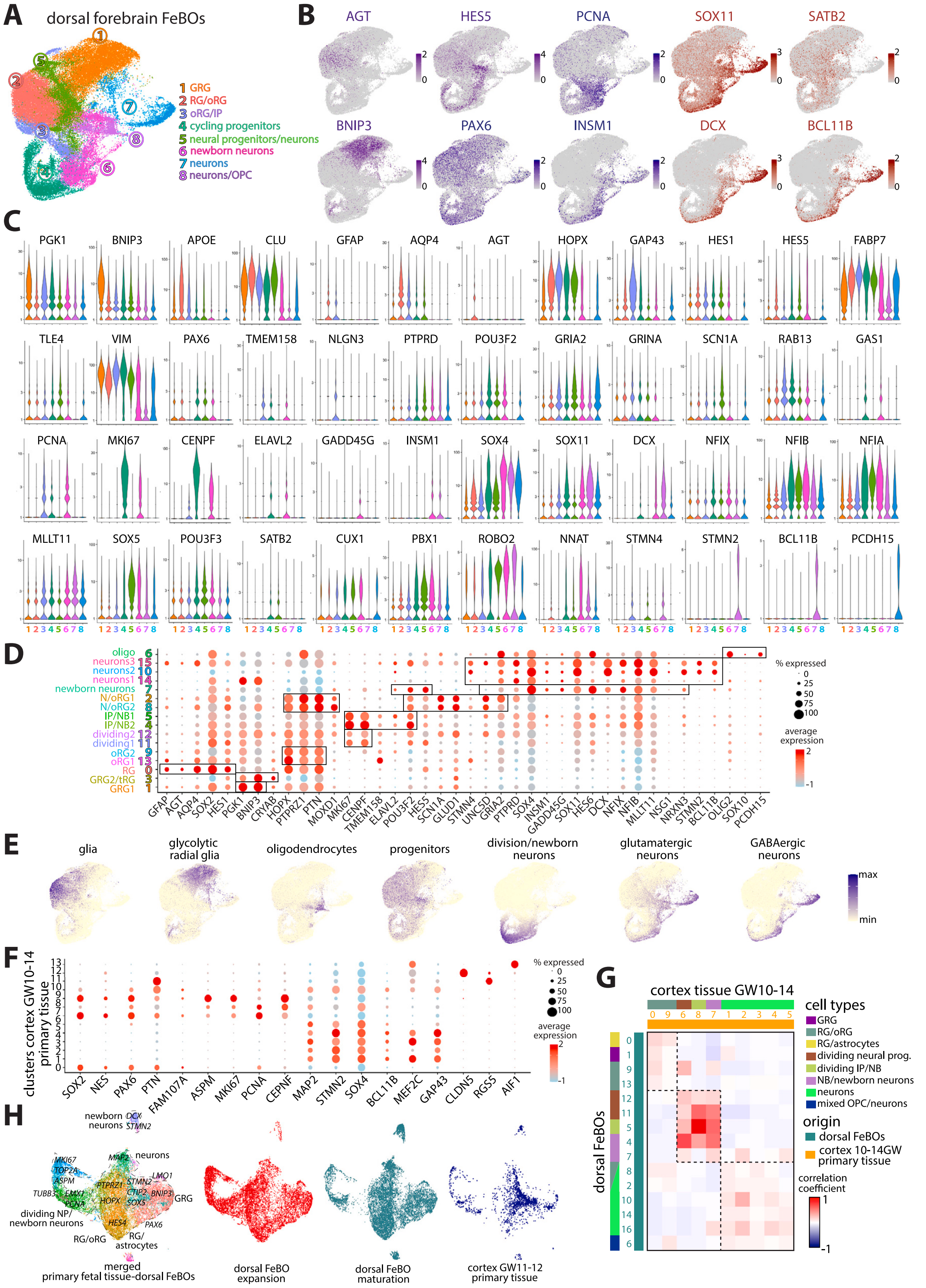

(legend on next page)

Figure S11. Single-cell sequencing analysis of dorsal forebrain FeBOs, related to Figure 4

(A) UMAP of cells derived from the integrated early passage and late passage expanded and matured dorsal forebrain FeBOs datasets, clustered into the main cell classes.

(B) UMAP plots colored by the expression of specific marker genes.

(C) Violin plots for multiple genes showing specific expression in the different main cell clusters, as defined in (A).

(D) Extended dot plot depicting expression of markers defining the different cell types and cluster identity, using the cluster annotation as in Figure 4H.

(E) Cell type-specific signature analysis. Each signature is based on a specific set of genes defined from previous studies (see Table S2).

(F) Dot plot depicting expression of markers defining the different cell types and cluster identities in primary cortex tissue. Data were reanalyzed from Bhaduri et al.[37]

(G) Correlation plot comparing tissue (x axis) and organoid (y axis) clusters with assigned cell identities between dorsal forebrain FeBOs and primary cortex tissue. Note that the clusters exclusively detected in tissue (pericytes, microglia) are not included, related to Figure 4M.

(H) UMAP representation showing the integration of the expanded and matured dorsal forebrain FeBO datasets with the primary cortex tissue (GW11-12) dataset from Fan et al.[52]

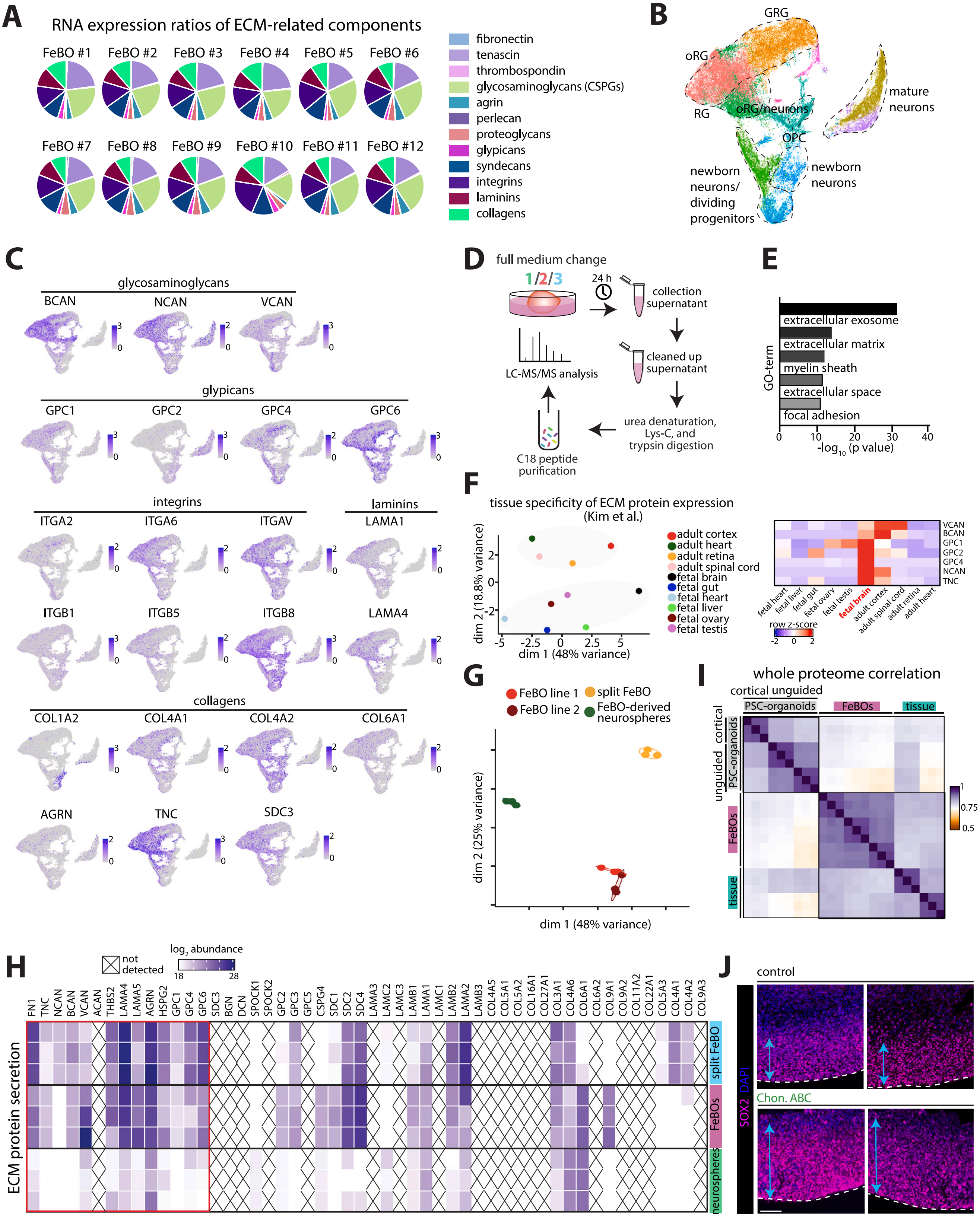

(legend on next page)

Figure S12. FeBOs present a physiological tissue-like ECM niche, related to Figure 5

(A) Pie charts showing and comparing the relative mRNA expression of ECM components in individual FeBOs.

(B) UMAP plot of expanded and matured dorsal forebrain FeBO datasets integrated with the dataset on primary cortex tissue (GW10-14), with the main cell classes annotated, as similarly shown in Figure 4N.

(C) UMAP plots colored by the expression of specific ECM genes in the different cellular populations.

(D) Experimental setup for secretome analysis.

(E) GO-term analysis on FeBO secretomes.

(F) PCA plot showing human fetal and adult tissues clustering based on proteomic expression of matrisome components (left). Heatmap of selected brain-enriched ECM components (right). Data derived from Kim et al.[58]

(G) PCA on ECM secretomes of the different experimental conditions (n = 3 replicates per condition).

(H) Extended heatmap showing the secretion of ECM components between FeBOs (in steady-state and upon splitting) with dissociated FeBO single-cell-derived neurospheres. All selected components that were searched in the different secretomes are visualized (n = 3 replicates per condition). Red box highlights the same proteins shown in Figure 5F.

(I) Correlation plot analysis on whole proteomes across the different conditions: FeBOs (3 lines), human fetal brain tissue (2 donors), PSC-cortical spheroids, and unguided PSC-cerebral organoids (2 different batches) (n = 3 replicates per condition).

(J) Representative immunofluorescence images for SOX2 in control and chondroitinase ABC-exposed FeBOs from 2 different lines. Scale bars, 100 μm.

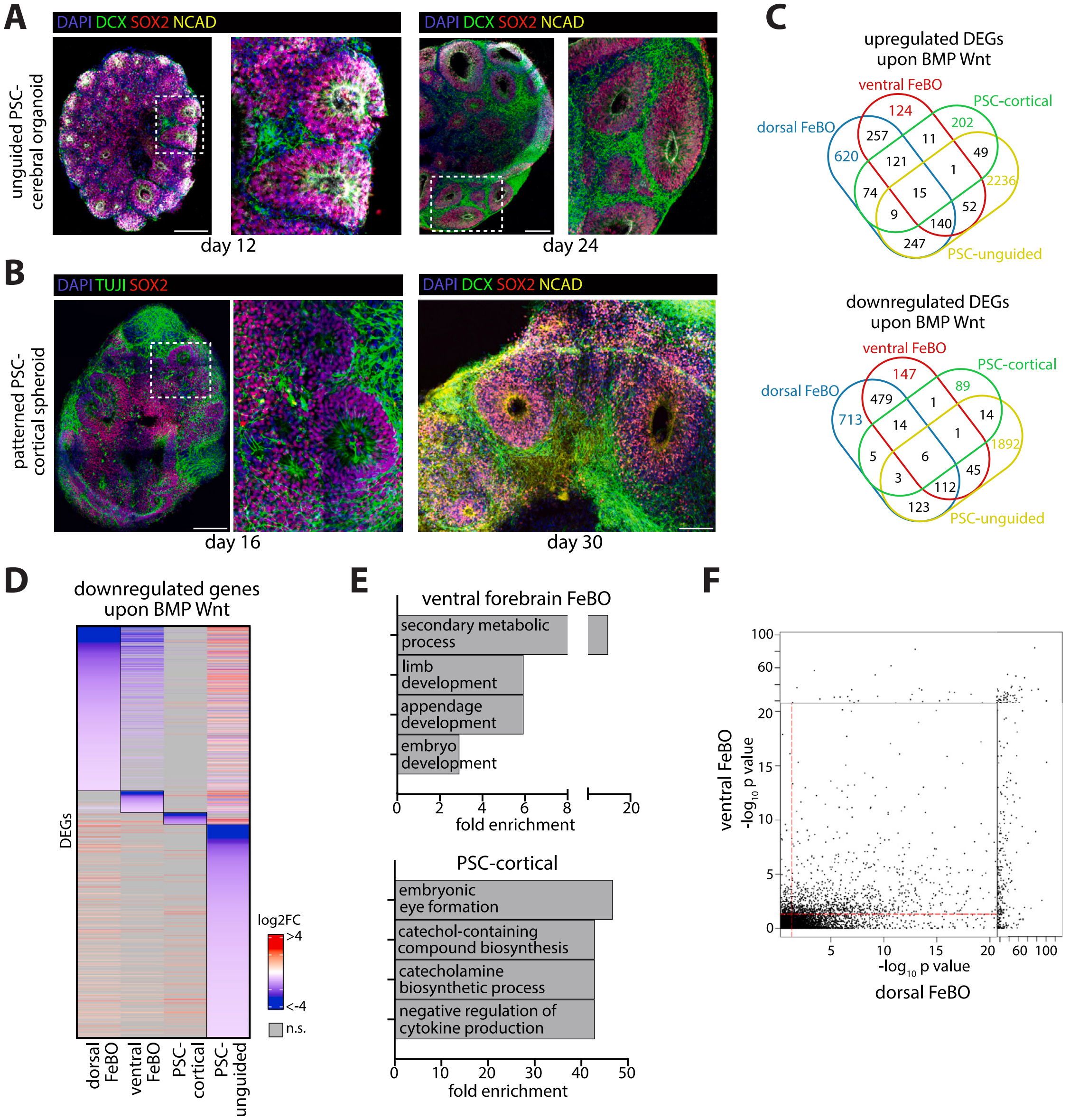

Figure S13. Transcriptomic responses upon BMP and Wnt exposure of FeBOs and PSC-brain models, related to Figure 6

(A) Representative immunofluorescence images of the indicated markers in unguided PSC-cerebral organoids at day 12 and day 24. Scale bars, 250 μm.

(B) Representative immunofluorescence images of the indicated markers in PSC-cortical spheroids at day 16 and day 30. Scale bars, 250 μm (left), 125 μm (right).

(C) Venn diagrams comparing the differentially expressed genes identified in each model upon BMP+Wnt exposure.

(D) Heatmap displaying the gene expression trends across all models upon BMP+Wnt exposure of all downregulated genes identified ($|\log_2FC| > 0.05$, $p < 0.05$) in each experimental condition vs. its own control upon BMP+Wnt exposure. n.s., not significant.

(E) GO-term enrichment analysis on the upregulated genes upon BMP+Wnt exposure identified in ventral forebrain FeBOs (top) and PSC-cortical spheroids (bottom).

(F) Dot plot comparing the differentially expressed genes based on p value between dorsal forebrain and ventral forebrain FeBOs. Red lines highlight the cutoff for significance.

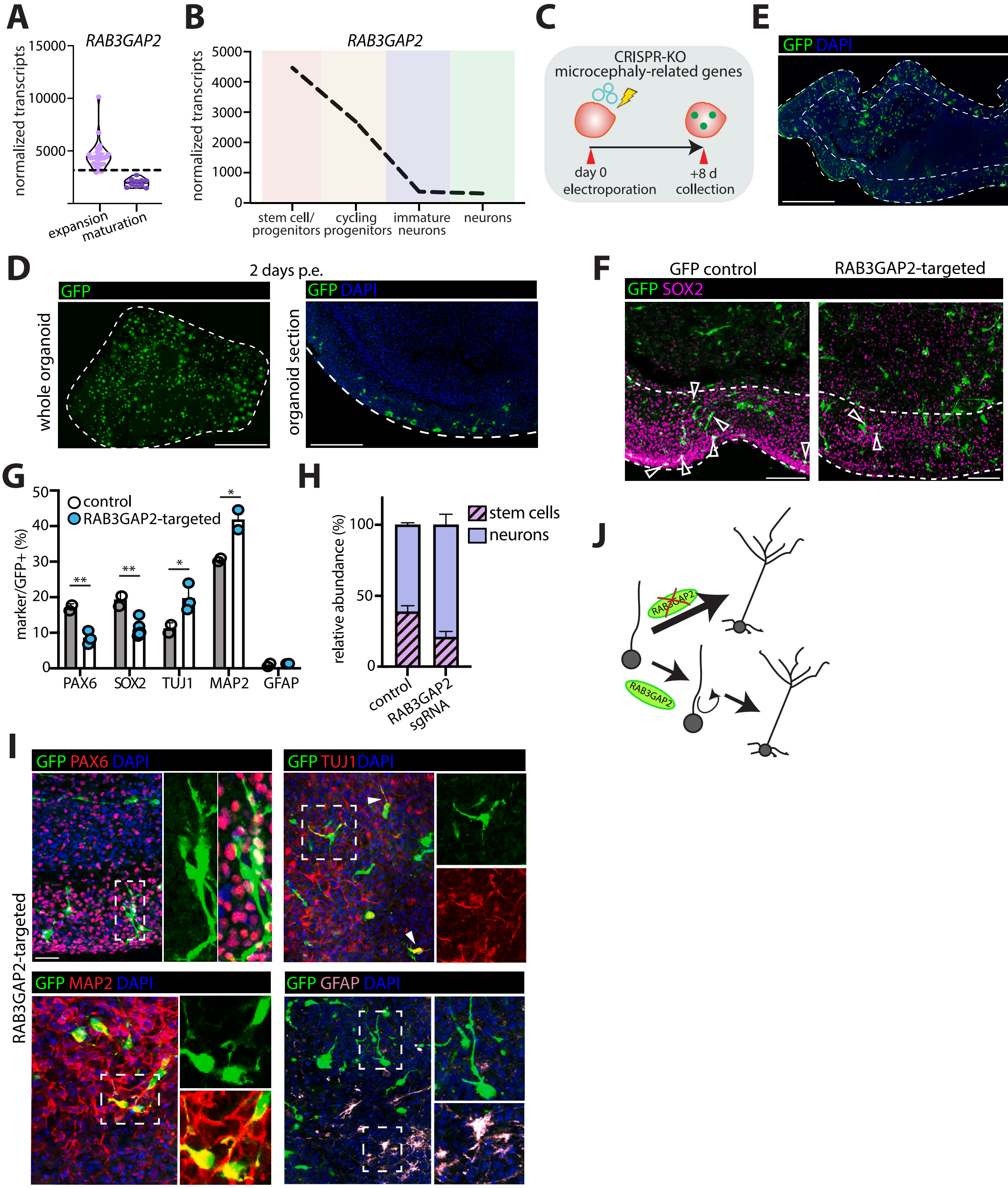

Figure S14. Interrogation of the microcephaly related gene RAB3GAP2 in FeBOs, related to Figure 7

(A) *RAB3GAP2* mRNA expression in expanding and matured FeBOs.

(B) Expression profile of *RAB3GAP2* in the different cell types in FeBOs along the cellular differentiation trajectory, as determined from pseudobulk data computed from the FeBO single-cell RNA sequencing data.

(C) Experimental setup to evaluate the role of RAB3GAP2 in FeBOs.

(D) Representative images of a whole FeBO and a FeBO section 2 days after electroporation with a *piggyBac*-transposable GFP construct and RAB3GAP2 sgRNA+Cas9. Scale bars, 750 μm (left), 500 μm (right).

(legend continued on next page)

(E) Representative image of a FeBO section 10 days after electroporation with a *piggyBac*-transposable GFP construct. Scale bars, 500 μm.

(F) Representative immunofluorescence images for SOX2 and GFP in control and RAB3GAP2-targeted FeBOs. Arrowheads indicate overlapping GFP and SOX2 signal. Scale bars, 100 μm.

(G) Quantification of colocalization of specific cell type markers in the GFP^+ population in control and RAB3GAP2-targeted FeBOs. Each dot represents an independent FeBO. $^*p < 0.05$; $^{**}p < 0.01$, Student's t test.

(H) Representative immunofluorescence images for the indicated markers in RAB3GAP2-targeted FeBOs at lower and higher magnification. Scale bars, 50 μm.

(I) Relative abundancy of stem cells and neurons in the GFP^+ population in control and RAB3GAP2-targeted FeBOs.

(J) Schematic of a suggested role of RAB3GAP2 in neuronal differentiation during human fetal brain development.

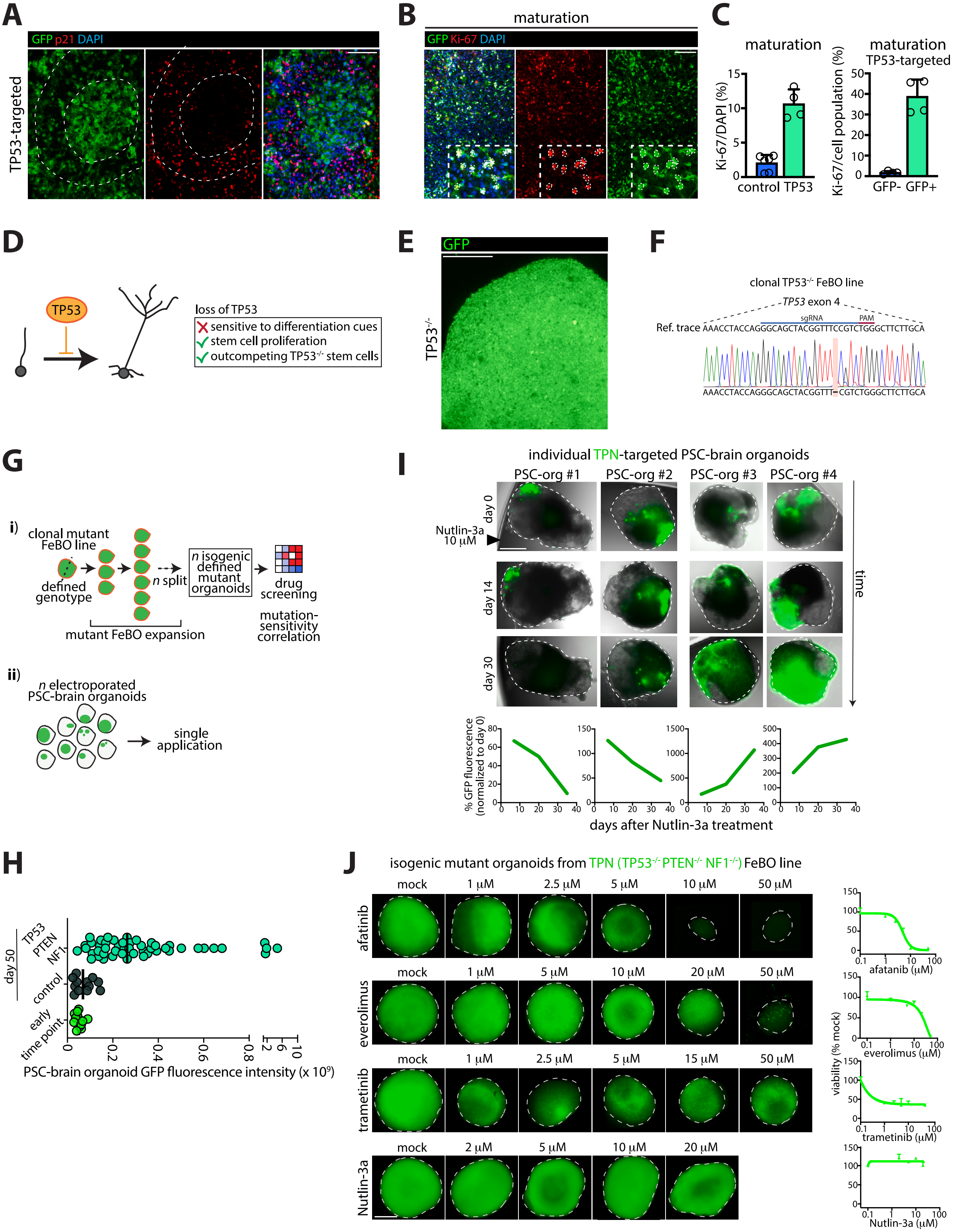

(legend on next page)

Figure S15. CRISPR-engineered FeBOs and drug screening in FeBO- and PSC-derived brain tumor models, related to Figure 7

(A) Representative immunofluorescence image for p21 (p53 target gene) in TP53-targeted (GFP$^+$) FeBOs. Scale bars, 50 μm.

(B) Representative immunofluorescence image for Ki-67 in matured TP53-targeted (GFP$^+$) FeBOs. Scale bars, 100 μm.

(C) Quantification of Ki-67$^+$ cells relative to the total amount of cells in maturation comparing control and TP53-targeted FeBOs (left) and specifically within the GFP$^+$ population (right) in TP53-targeted FeBOs.

(D) Schematic of a suggested role of TP53 in human fetal brain development.

(E) Representative GFP fluorescence image, demonstrating the generation of a fully mutant (GFP$^+$) *TP53*$^{-/-}$ FeBO line (ca. 3–4 months after electroporation). Scale bars, 300 μm.

(F) Schematic of the sgRNA used to introduce *TP53* mutations and an example of a genotype of a clonal *TP53*$^{-/-}$ FeBO line.

(G) Schematic overview of brain tumor modeling in FeBOs (i) and PSC-derived brain organoids (ii).

(H) Quantification of the GFP fluorescence intensity of individual control or TPN-targeted PSC-brain organoids at day 50 and at an early time point.

(I) Brightfield and GFP fluorescence overlay images of individual TPN-targeted PSC-brain organoids (50 days p.e.), treated with Nutlin-3a over time (top). Quantification of the GFP fluorescence over time (as percentage increase/decrease as compared with the start of Nutlin-3a treatment) within each organoid (bottom). Scale bars, 0.5 mm.

(J) Representative GFP fluorescence images of isogenic mutant organoids from an established TPN FeBO line in response to increasing doses of afatinib, everolimus, trametinib, and Nutlin-3a. The images of trametinib and Nutlin-3a are also shown in Figure 7K. Scale bars, 0.5 mm.